NLO QCD corrections to off-shell top-antitop production with leptonic decays at hadron colliders

Denner, A ; Dittmaier, S ; Kallweit, S ; Pozzorini, S

Abstract: We present details of a calculation of the cross section for hadronic top-antitop production in next-to-leading order (NLO) QCD, including the decays of the top and antitop into bottom quarks and leptons. This calculation is based on matrix elements for e e+ - overline *boverlinebproductionandincludesallnon−resonantdiagrams, interferences, andoff−shelleffectsofthetopquarks.Suchcontributionsareformallysuppressedbyth quarkwidthandturnouttobesmallintheinclusivecrosssection.However, theycanbestronglyenhancedinexclusiveobservabl physicssearches.Alsonon−resonantandoff−shelleffectsduetothefiniteW−bosonwidthareinvestigatedindetail, butthe energytailsofdistributions, butanappropriatedynamicalscalestabilisesNLOpredictions.Numericalresultsforthetotalcr*

DOI: https://doi.org/10.1007/JHEP10(2012)110

FR-PHENO-2012-007
ZU-TH 12/12

NLO QCD corrections to off-shell top–antitop production with leptonic decays at hadron colliders

A. Denner[1], S. Dittmaier[2], S. Kallweit[3] and S. Pozzorini[3]

[1] *Universität Würzburg, Institut für Theoretische Physik und Astrophysik, D-97074 Würzburg, Germany*

[2] *Albert-Ludwigs-Universität Freiburg, Physikalisches Institut, D-79104 Freiburg, Germany*

[3] *Institut für Theoretische Physik, Universität Zürich, CH-8057 Zürich, Switzerland*

Abstract:

We present details of a calculation of the cross section for hadronic top–antitop production in next-to-leading order (NLO) QCD, including the decays of the top and antitop into bottom quarks and leptons. This calculation is based on matrix elements for $\nu_e e^+ \mu^- \bar{\nu}_\mu b\bar{b}$ production and includes all non-resonant diagrams, interferences, and off-shell effects of the top quarks. Such contributions are formally suppressed by the top-quark width and turn out to be small in the inclusive cross section. However, they can be strongly enhanced in exclusive observables that play an important role in Higgs and new-physics searches. Also non-resonant and off-shell effects due to the finite W-boson width are investigated in detail, but their impact is much smaller than naively expected. We also introduce a matching approach to improve NLO calculations involving intermediate unstable particles. Using a fixed QCD scale leads to perturbative instabilities in the high-energy tails of distributions, but an appropriate dynamical scale stabilises NLO predictions. Numerical results for the total cross section, several distributions, and asymmetries are presented for Tevatron and the LHC at 7 TeV, 8 TeV, and 14 TeV.

July 2012

1 Introduction

As the only fundamental known fermion with a mass at the electroweak scale, the top quark might serve as a key for understanding the fermionic mass hierarchy and is potentially sensitive to physics beyond the Standard Model. Since it can be produced copiously at the LHC in top–antitop pairs, its production cross section, its decay, and its properties can be studied with high precision. Evidently, accurate measurements must be accompanied by precise calculations.

The first step towards precise theoretical predictions for $t\bar{t}$ production at hadron colliders was made already about 20 years ago with the calculation of QCD corrections at next-to-leading-order (NLO) [1–4]. Later also electroweak radiative corrections were calculated [5–10], and recently important progress has been achieved both in the resummation of logarithmically enhanced terms [11–14] and towards the inclusion of QCD corrections at next-to-next-to-leading-order (NNLO) [15–25]. First NNLO QCD results for the quark–antiquark channel have been presented in Ref. [26].

The above-mentioned predictions are based on the approximation of stable (on-shell) top quarks, i.e. the top-quark decays, which proceed into pairs of W bosons and b quarks in the Standard Model, are ignored. A thorough LO analysis of hadronic top-pair production and decay including off-shell and non-resonant contributions was presented in Ref. [27]. A first important step towards a full NLO description of top-pair production and decay was made in Refs. [28–30], where top-quark decays were treated in a spin-correlated narrow-width approximation, i.e. the top quarks are still on shell, but spin correlations between production and decay are taken into account. Meanwhile, NLO top-quark decays in narrow-width approximation were implemented in MCFM [31].

Recently, first results at NLO QCD for the complete process of $W^+W^-b\bar{b}$ production, with intermediate off-shell top quarks and including leptonic W-boson decays have been obtained by two independent groups [32, 33]. Here we give details on one of these calculations [32] and extend the presented results in various directions.

The reaction $pp \to W^+W^-b\bar{b} \to \nu_e e^+ \mu^- \bar{\nu}_\mu b\bar{b}$ represents one of the $2 \to 4$ particle processes on the Les Houches priority list [34]. While various multi-particle NLO QCD calculations have been performed in the recent years [35–49], $W^+W^-b\bar{b}$ production involves the treatment of resonant particles for the first time in a hadron-collider environment on that level of complexity. The two top resonances can be consistently treated in the complex-mass scheme that was introduced at the NLO level in the context of the calculation of the electroweak corrections to the processes $e^+e^- \to W^+W^- \to 4\,\text{fermions}$ [50,51], which was the first full NLO calculation for a $2 \to 4$ particle process.

To compute the virtual corrections, we employ explicit diagrammatic representations of the one-loop amplitudes. A key feature of our approach is the factorization of colour structures at the level of individual diagrams. This permits to reduce the CPU cost of colour sums essentially to zero. Helicity-dependent structures are algebraically reduced to a common set of so-called standard matrix elements. In this way the sums over physical helicities are strongly boosted. Tensor loop integrals are related to scalar integrals by means of numerical algorithms that systematically avoid numerical instabilities from inverse Gram determinants and other spurious singularities [52,53]. Scalar loop integrals are required with complex internal masses and are evaluated using the results of Refs. [54, 55].

The real corrections are handled with the dipole subtraction method [56–59], and the phase-space integration is performed with adaptive multi-channel techniques [60–62].

Our predictions provide a complete description of hadronic $\mathrm{W^+W^-b\bar{b}}$ production, including off-shell $\mathrm{t\bar{t}}$ intermediate states, as well as contributions with a single or no top-quark resonance. This permits to quantify the accuracy of the narrow-top-width approximation, which involves only on-shell $\mathrm{t\bar{t}}$ contributions and corresponds to the $\Gamma_\mathrm{t} \to 0$ limit of our calculation, at NLO. For the integrated cross section it turns out that, in presence of loose cuts, the error of the narrow-top-width approximation does not exceed 1% [32, 33, 63]. This is perfectly consistent with the theoretically expected $\mathcal{O}(\Gamma_\mathrm{t}/m_\mathrm{t})$ suppression of finite-top-width corrections to inclusive observables.

In more exclusive measurements, such as precision m_t determinations, $\mathrm{t\bar{t}}$ backgrounds to new physics that are suppressed by vetoing top resonances, or the $\mathrm{t\bar{t}}$ background to $\mathrm{H} \to ll\nu\nu$ signals in presence of b-jet vetoes, the investigation of finite-top-width effects is even more important since their magnitude is not known a priori. A first systematic study of finite-top-width effects in exclusive observables, based on a comparison of our calculation against the narrow-top-width approximation of Ref. [29], indicates that finite-top-width corrections to phenomenologically important observables can range from a few per mille to tens of per cent [63]. This motivates us, on the one hand, to undertake a more thorough comparison of the narrow- and finite-top-width approaches, which will be presented in a forthcoming paper [64]. On the other hand, it raises the issue of possible non-negligible effects resulting from the finite width of intermediate W bosons, which is addressed in the present paper.

To study finite-W-width effects we consider two different descriptions of the leptonic W-boson decays: a (spin-correlated) narrow-W-width approximation and, alternatively, matrix elements for $\nu_\mathrm{e}\mathrm{e}^+\mu^-\bar{\nu}_\mu\mathrm{b\bar{b}}$ production, including off-shell and non-resonant finite-W-width contributions[1]. While finite-W-width effects have already been included in the predictions of Ref. [33], comparing the two above-mentioned approaches provides the first quantitative assessment of the precision of the narrow-W-width approximation in $\nu_\mathrm{e}\mathrm{e}^+\mu^-\bar{\nu}_\mu\mathrm{b\bar{b}}$ production. In spite of the larger numerical value of $\Gamma_\mathrm{W}/M_\mathrm{W}$ as compared to $\Gamma_\mathrm{t}/m_\mathrm{t}$, finite-W-width corrections turn out to be definitely smaller than finite-top-width effects. As we discuss, this is due to a double-suppression mechanism related to subtle cancellations between finite-W-width contributions to matrix elements and to the Γ_t input parameter.

The paper is organized as follows. In Section 2 we discuss technical aspects of the calculation, including finite-top-width and finite-W-width effects (Section 2.1), as well as virtual (Section 2.2) and real (Section 2.3) corrections. In Section 2.1.2 we also introduce a matching approach that restores exact factorization of $\mathrm{t\bar{t}}$ production and top decays in the $\Gamma_\mathrm{t} \to 0$ limit. This permits to avoid a few-per-cent loss of precision in the non-factorized NLO description of $\nu_\mathrm{e}\mathrm{e}^+\mu^-\bar{\nu}_\mu\mathrm{b\bar{b}}$ production while including finite-top-width effects. In Section 3 we present numerical predictions for Tevatron and the LHC at different collider energies. The choice of the factorization and renormalization scales is discussed in some detail in Section 3.2. There we introduce a dynamical scale related to the transverse energy of the top quarks, which avoids serious perturbative instabilities in the high-energy tails of differential distributions. Moreover, we advocate the use of

[1]The virtual corrections are calculated in the double-pole approximation for the W resonances.

a collider-dependent QCD scale adapted to the particular behaviour of the leading partonic channels, i.e. quark–antiquark annihilation at the Tevatron and gluon–gluon fusion at the LHC. Specifically, we argue that a reduced scale provides a better description of $\mathrm{W^+W^-b\bar{b}}$ production at the LHC. Results for the integrated cross sections (Section 3.3), asymmetries (Section 3.4), and several distributions (Section 3.5), are supplemented by a numerical extrapolation of the $\nu_\mathrm{e}\mathrm{e}^+\mu^-\bar{\nu}_\mu\mathrm{b\bar{b}}$ cross section to the $\Gamma_\mathrm{t} \to 0$ limit (Section 3.6). Finally, in Section 3.7 we show that our results are in good agreement with corresponding results [33] obtained with HELAC-NLO [65]. Our conclusions are presented in Section 4, and in App. A we provide benchmark results for the partonic matrix elements squared in lowest order and including virtual corrections.

2 Details of the calculation

2.1 Preliminaries

The cross section for the hadronic process $h_1h_2 \to \mathrm{W^+W^-b\bar{b}} + X \to \nu_\mathrm{e}\mathrm{e}^+\mu^-\bar{\nu}_\mu\mathrm{b\bar{b}} + X$ is evaluated according to

$$\sigma = \sum_{a,b} \int_0^1 \mathrm{d}x_1 \int_0^1 \mathrm{d}x_2\, f_{a/h_1}(x_1)\, f_{b/h_2}(x_2) \int \mathrm{d}\hat{\sigma}_{ab}(x_1P_1, x_2P_2), \tag{2.1}$$

where the parton distribution functions (PDFs) $f_{c/h_i}(x_i)$ describe the probabilities of finding a parton c in hadron h_i with a fraction x_i of the full hadron momentum P_i. In LO the colliding parton pairs are $ab = \mathrm{g}\mathrm{g}, q\bar{q}, \bar{q}q$, but higher orders involve contributions from $\mathrm{g}q, \mathrm{g}\bar{q}, q\mathrm{g}$, and $\bar{q}\mathrm{g}$ as well. We consistently neglect contributions from initial-state bottom quarks,[2] i.e. $q = \mathrm{u}, \mathrm{d}, \mathrm{c}, \mathrm{s}$. Otherwise we work in the five-flavour scheme with massless bottom quarks. In NLO, the partonic cross section

$$\int \mathrm{d}\hat{\sigma}_{ab} = \int_6 \mathrm{d}\hat{\sigma}_{0,ab} + \int_6 \mathrm{d}\hat{\sigma}_{\mathrm{virt},ab} + \int_7 \mathrm{d}\hat{\sigma}_{\mathrm{real},ab} + \int_0^1 \mathrm{d}x \int_6 \mathrm{d}\hat{\sigma}_{\mathrm{fact},ab} \tag{2.2}$$

receives contributions from tree diagrams ($\hat{\sigma}_{0,ab}$), virtual one-loop corrections ($\hat{\sigma}_{\mathrm{virt},ab}$), real parton emission ($\hat{\sigma}_{\mathrm{real},ab}$), and the factorization of collinear initial-state singularities ($\hat{\sigma}_{\mathrm{fact},ab}$) into the PDFs. The subscript on the integral corresponds to the number of final-state particles in the reaction $ab \to \mathrm{W^+W^-b\bar{b}}(c) \to \nu_\mathrm{e}\mathrm{e}^+\mu^-\bar{\nu}_\mu\mathrm{b\bar{b}}(c)$, where c is a possibly emitted parton. The integral over x indicates that the factorization contribution involves an additional integration over the fraction x by which one of the incoming parton momenta is reduced due to collinear initial-state radiation.

In order to ensure the correctness of our results we have evaluated each ingredient twice and independently, resulting in two independent computer codes.

In the following we discuss the treatment of top-quark and W-boson resonances as well as effects beyond NLO related to the factorization of $\mathrm{t\bar{t}}$ production and top decays in the narrow-top-width limit. Details of the calculations of the virtual and real corrections are given in Sections 2.2 and 2.3.

[2] We have checked that bottom-quark-induced contributions to the integrated cross section are suppressed at the level of $\lesssim 0.2\%$ at LO.

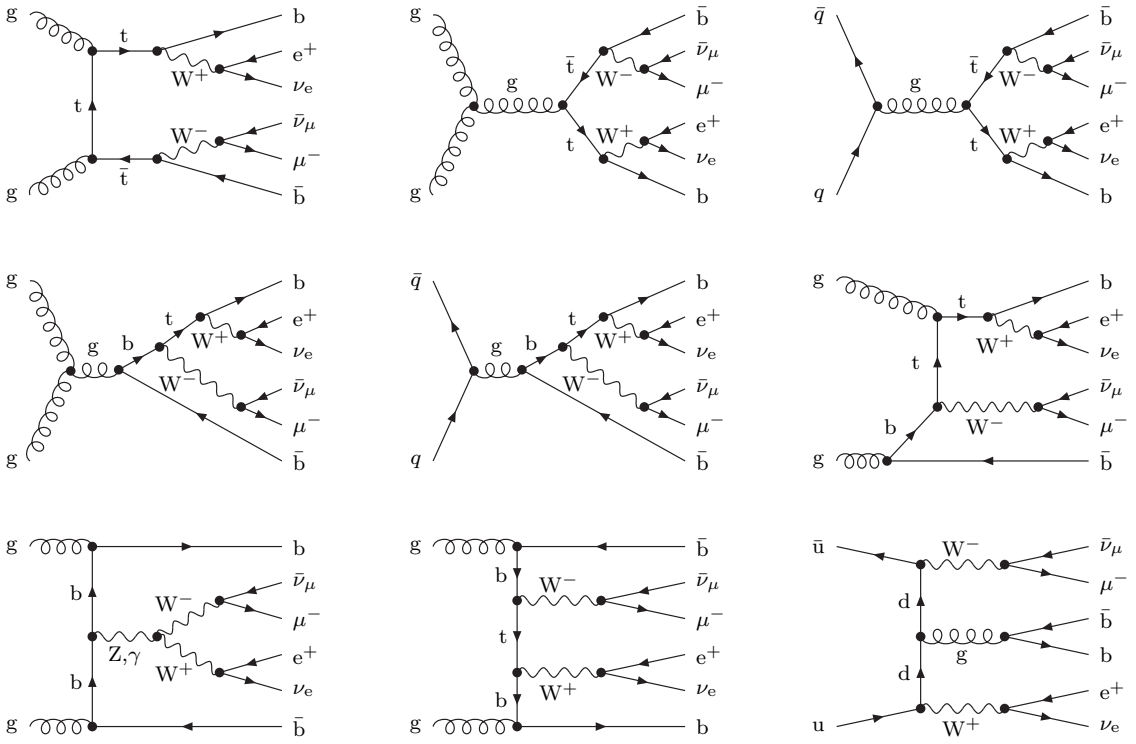

Figure 1: Representative tree diagrams involving two (first line), only one (second line), or no (last line) top-quark resonances.

2.1.1 Treatment of unstable top quarks

Our predictions for the process $h_1 h_2 \to \mathrm{W^+W^-b\bar{b}} + X \to \nu_\mathrm{e}\mathrm{e}^+\mu^-\bar{\nu}_\mu \mathrm{b\bar{b}} + X$ provide a complete description of hadronic top-quark pair production and decay, including doubly-resonant contributions where the $\nu_\mathrm{e}\mathrm{e}^+\mu^-\bar{\nu}_\mu \mathrm{b\bar{b}}$ final state results from the decay of a $\mathrm{t\bar{t}}$ pair, as well as singly-resonant and non-resonant diagrams, i.e. contributions with only one or no top resonance. Interferences between doubly-, singly-, and non-resonant diagrams are consistently taken into account. A few representative LO diagrams are depicted in Figure 1. The $q\bar{q}$ and gg partonic channels involve 14 and 31 tree diagrams, respectively, if only topologies involving two resonant W bosons are considered.[3] Additional contributions with less than two W-boson resonances are discussed in Section 2.1.3.

To regularize intermediate top-quark resonances in a gauge-invariant way we employ the complex-mass scheme [51], where the top-quark width Γ_t is incorporated into the definition of the (squared) top-quark mass,

$$\mu_\mathrm{t}^2 = m_\mathrm{t}^2 - \mathrm{i}m_\mathrm{t}\Gamma_\mathrm{t}. \tag{2.3}$$

[3]Since we treat b quarks as massless partons there are no Higgs-exchange diagrams at tree level.

In this way, off-shell-top contributions are consistently described by Breit–Wigner distributions, and all matrix elements are evaluated using the complex top mass μ_t. Technical implications of the complex-mass scheme at one loop are discussed in Section 2.2.6.

The inclusive $\nu_\mathrm{e}\mathrm{e}^+\mu^-\bar{\nu}_\mu\mathrm{b}\bar{\mathrm{b}}$ cross section is dominated by the doubly-resonant top-pair contribution and can be described, with fairly good accuracy, in narrow-top-width approximation. It is thus instructive to compare our calculation to this approximation, which corresponds to the $\Gamma_\mathrm{t} \to 0$ limit. To avoid confusion between the treatment of top-quark and W-boson decays, in the following we denote the $\Gamma_\mathrm{t} \to 0$ and $\Gamma_\mathrm{W} \to 0$ limits as narrow-top-width (NtWA) and narrow-W-width (NwWA) approximations, respectively. Contributions that vanish in NtWA and NwWA are called finite-top-width (FtW) and finite-W-width (FwW) effects, respectively. Our treatment of FwW effects is discussed in Section 2.1.3.

For what concerns top resonances, we point out that FtW contributions are included everywhere in our calculation, i.e. we never make use of the NtWA. Nevertheless, in the following we briefly introduce this approximation in order to discuss the origin of FtW effects and other features of our predictions. In the NtWA, each top-quark resonance leads to

$$\lim_{\Gamma_\mathrm{t}\to 0} \frac{1}{(p_\mathrm{t}^2 - m_\mathrm{t}^2)^2 + m_\mathrm{t}^2\Gamma_\mathrm{t}^2} = \frac{\pi}{m_\mathrm{t}\Gamma_\mathrm{t}}\,\delta(p_\mathrm{t}^2 - m_\mathrm{t}^2), \tag{2.4}$$

where the δ-function that forces the top quark on its mass shell is accompanied by a $1/\Gamma_\mathrm{t}$ factor. In NtWA the $\nu_\mathrm{e}\mathrm{e}^+\mu^-\bar{\nu}_\mu\mathrm{b}\bar{\mathrm{b}}$ cross section includes only contributions involving two top resonances, which are proportional to $1/\Gamma_\mathrm{t}^2$. Singly- and non-resonant diagrams, as well as their interference with doubly-resonant diagrams, are neglected due to their suppression in the $\Gamma_\mathrm{t} \to 0$ limit. As a result of these approximations, the differential $h_1h_2 \to \mathrm{t}\bar{\mathrm{t}} \to \nu_\mathrm{e}\mathrm{e}^+\mu^-\bar{\nu}_\mu\mathrm{b}\bar{\mathrm{b}}$ cross section is factorized into the $h_1h_2 \to \mathrm{t}\bar{\mathrm{t}}$ production cross section times the $\mathrm{t} \to \mathrm{W}\mathrm{b} \to l\nu_l\mathrm{b}$ partial decay widths,

$$\mathrm{d}\sigma_\mathrm{NtWA} = \Gamma_\mathrm{t}^{-2}\left(\mathrm{d}\sigma_{\mathrm{t}\bar{\mathrm{t}}}\,\mathrm{d}\Gamma_{\mathrm{t}\to i}\,\mathrm{d}\Gamma_{\bar{\mathrm{t}}\to j}\right), \tag{2.5}$$

where the subscripts i, j refer to the (anti)top-decay final states $\nu_\mathrm{e}\mathrm{e}^+\mathrm{b}$ and $\mu^-\bar{\nu}_\mu\bar{\mathrm{b}}$, and the total top-quark width is obtained by summing over all relevant decay channels,

$$\Gamma_\mathrm{t} = \sum_k \int \mathrm{d}\Gamma_{\mathrm{t}\to k}. \tag{2.6}$$

Top-quark spin correlations in (2.5) are implicitly understood.

In NtWA, LO and NLO partonic cross sections can be schematically written as

$$\begin{aligned}
\mathrm{d}\sigma^\mathrm{LO}_\mathrm{NtWA} &= (\Gamma_\mathrm{t}^\mathrm{LO})^{-2}\Big[\mathrm{d}\sigma^\mathrm{LO}_{\mathrm{t}\bar{\mathrm{t}}}\,\mathrm{d}\Gamma^\mathrm{LO}_{\mathrm{t}\to i}\,\mathrm{d}\Gamma^\mathrm{LO}_{\bar{\mathrm{t}}\to j}\Big],\\
\mathrm{d}\sigma^\mathrm{NLO}_\mathrm{NtWA} &= (\Gamma_\mathrm{t}^\mathrm{NLO})^{-2}\Big[\left(\mathrm{d}\sigma^0_{\mathrm{t}\bar{\mathrm{t}}} + \mathrm{d}\sigma^1_{\mathrm{t}\bar{\mathrm{t}}}\right)\mathrm{d}\Gamma^0_{\mathrm{t}\to i}\,\mathrm{d}\Gamma^0_{\bar{\mathrm{t}}\to j} + \mathrm{d}\sigma^0_{\mathrm{t}\bar{\mathrm{t}}}\left(\mathrm{d}\Gamma^1_{\mathrm{t}\to i}\,\mathrm{d}\Gamma^0_{\bar{\mathrm{t}}\to j} + \mathrm{d}\Gamma^0_{\mathrm{t}\to i}\,\mathrm{d}\Gamma^1_{\bar{\mathrm{t}}\to j}\right)\Big],
\end{aligned} \tag{2.7}$$

where the superscripts 0 and 1 indicate LO and correction contributions to NLO quantities, i.e. $\mathrm{d}\Gamma^\mathrm{NLO}_{\mathrm{t}\to k} = \mathrm{d}\Gamma^0_{\mathrm{t}\to k} + \mathrm{d}\Gamma^1_{\mathrm{t}\to k}$ and $\mathrm{d}\sigma^\mathrm{NLO}_{\mathrm{t}\bar{\mathrm{t}}} = \mathrm{d}\sigma^0_{\mathrm{t}\bar{\mathrm{t}}} + \mathrm{d}\sigma^1_{\mathrm{t}\bar{\mathrm{t}}}$. Note that $\mathrm{d}\sigma^0_{\mathrm{t}\bar{\mathrm{t}}} \neq \mathrm{d}\sigma^\mathrm{LO}_{\mathrm{t}\bar{\mathrm{t}}}$, since the ingredients of $\mathrm{d}\sigma^\mathrm{LO}_\mathrm{NtWA}$ and $\mathrm{d}\sigma^\mathrm{NLO}_\mathrm{NtWA}$ have to be evaluated with input parameters

at the corresponding perturbative order, i.e. $\mathrm{d}\sigma^{\mathrm{LO}}_{\mathrm{t\bar{t}}}$ and $\mathrm{d}\sigma^{0}_{\mathrm{t\bar{t}}}$ are evaluated with PDFs and α_{s} in LO and NLO, respectively. Since the top decay does not involve α_{s} at LO we have $\mathrm{d}\Gamma^{0}_{\mathrm{t}\to k} = \mathrm{d}\Gamma^{\mathrm{LO}}_{\mathrm{t}\to k}$. Note also that LO and NLO predictions must be computed using total decay widths $\Gamma^{\mathrm{LO}}_{\mathrm{t}}$ and $\Gamma^{\mathrm{NLO}}_{\mathrm{t}}$, respectively. Naturally, this also holds for our calculation, not only in NtWA.

As a result of the truncation of the perturbative expansion, the NtWA of the NLO cross section (2.7) involves only three contributions, where the corrections are applied either to $\mathrm{d}\sigma_{\mathrm{t\bar{t}}}$ or to one of the decays. A pure fixed-order NLO calculation does not include contributions like $\mathrm{d}\sigma^{1}_{\mathrm{t\bar{t}}}\mathrm{d}\Gamma^{1}_{\mathrm{t}\to i}\mathrm{d}\Gamma^{0}_{\bar{\mathrm{t}}\to j}$, where the NLO correction is simultaneously applied to the production and decay parts of the process. Such contributions are formally of NNLO, but given their non-negligible numerical impact it is desirable to take them into account. As discussed in Section 2.1.2, this can be achieved by means of a simple prescription which is applicable also in presence of FtW and FwW corrections and is derived by matching Eq. (2.7) to Eq. (2.5) at the level of the fully inclusive cross section.

As compared to the NtWA, our calculation includes two types of additional effects owing to the FtW: corrections resulting from the top-quark off-shellness in doubly-resonant channels and contributions from singly- as well as non-resonant diagrams. At NLO, FtW effects manifest themselves also in the form of non-factorizable corrections to doubly-resonant diagrams, which originate from one-loop topologies or interferences between real-emission diagrams, where top–antitop production and top decays are linked via exchange of QCD partons. Technically, the calculation of non-factorizable, singly-, and non-resonant one-loop contributions involves pentagon and hexagon diagrams, which represent a much higher level of complexity as compared to the four- and lower-point diagrams that appear in NtWA.

The non-factorizable contributions of virtual and real origin are enhanced by large logarithms of $\Gamma_{\mathrm{t}}/m_{\mathrm{t}}$ originating from soft gluons. However, it is well known that—in *sufficiently inclusive* $\mathrm{t\bar{t}}$ observables—such logarithms cancel, and the remaining FtW effects yield rather small contributions of order $\Gamma_{\mathrm{t}}/m_{\mathrm{t}} \simeq 0.9\%$ [66–68]. Nevertheless, a reliable quantitative assessment of FtW effects is important in order to achieve per-cent-level precision in the (inclusive and differential) description of $\mathrm{t\bar{t}}$ production. Comparing our predictions to the NtWA, one can obtain a precise determination of FtW contributions to any infrared-safe observable. For the case of the integrated cross section, we performed this comparison by means of a numerical extrapolation of our predictions to the $\Gamma_{\mathrm{t}} \to 0$ limit [32]. The results, discussed in Section 3.6, demonstrate that the NtWA for the integrated cross section agrees with the full calculation at the sub-per-cent level.

As already mentioned in the introduction, in more exclusive phenomenological studies, such as precision m_{t} measurements or Higgs- and new-physics searches, the size of FtW corrections cannot be anticipated a priori and turns out to range from a few per mille to tens of per cent [63, 64].

2.1.2 Matching to NLO inclusive $\mathrm{t\bar{t}}$ cross section

Let us now discuss effects related to the truncation of the perturbative expansion at NLO in the presence of unstable intermediate particles. To start with, we consider the fully inclusive cross section in NtWA,

$$\int \mathrm{d}\sigma_{\mathrm{NtWA}} = \sigma_{\mathrm{t\bar{t}}}\,\mathrm{BR}_{\mathrm{t}\to i}\,\mathrm{BR}_{\bar{\mathrm{t}}\to j}, \tag{2.8}$$

which is obtained by integrating (2.5) over the full phase space and is given by the on-shell inclusive $\mathrm{t\bar{t}}$ cross section,

$$\sigma_{\mathrm{t\bar{t}}} = \int \mathrm{d}\sigma_{\mathrm{t\bar{t}}}, \tag{2.9}$$

times the branching fractions

$$\mathrm{BR}_{\mathrm{t}\to k} = \frac{\Gamma_{\mathrm{t}\to k}}{\Gamma_{\mathrm{t}}} = \frac{\int \mathrm{d}\Gamma_{\mathrm{t}\to k}}{\Gamma_{\mathrm{t}}}, \tag{2.10}$$

with $k = i, j$. Apart from Coulomb effects near threshold, the above relation between the $\mathrm{pp} \to \mathrm{t\bar{t}} \to ij$ and the on-shell $\mathrm{t\bar{t}}$ cross sections is valid to all orders of perturbation theory [67]. However, due to missing higher-order terms, the NLO approximation (2.7) does not fulfil (2.8) exactly. The mismatch can be expressed in terms of products of NLO contributions as follows,

$$\begin{aligned}
\Delta\sigma^{\mathrm{NLO}}_{\mathrm{trunc}} &= \sigma^{\mathrm{NLO}}_{\mathrm{t\bar{t}}}\,\mathrm{BR}^{\mathrm{NLO}}_{\mathrm{t}\to i}\,\mathrm{BR}^{\mathrm{NLO}}_{\bar{\mathrm{t}}\to j} - \int \mathrm{d}\sigma^{\mathrm{NLO}}_{\mathrm{NtWA}} \\
&= (\Gamma^{\mathrm{NLO}}_{\mathrm{t}})^{-2}\left(\sigma^{0}_{\mathrm{t\bar{t}}} + \sigma^{1}_{\mathrm{t\bar{t}}}\right)\left(\Gamma^{0}_{\mathrm{t}\to i} + \Gamma^{1}_{\mathrm{t}\to i}\right)\left(\Gamma^{0}_{\bar{\mathrm{t}}\to j} + \Gamma^{1}_{\bar{\mathrm{t}}\to j}\right) - \int \mathrm{d}\sigma^{\mathrm{NLO}}_{\mathrm{NtWA}} \\
&= (\Gamma^{\mathrm{NLO}}_{\mathrm{t}})^{-2}\Big[\left(\sigma^{0}_{\mathrm{t\bar{t}}} + \sigma^{1}_{\mathrm{t\bar{t}}}\right)\,\Gamma^{1}_{\mathrm{t}\to i}\,\Gamma^{1}_{\bar{\mathrm{t}}\to j} + \sigma^{1}_{\mathrm{t\bar{t}}}\,\left(\Gamma^{1}_{\mathrm{t}\to i}\,\Gamma^{0}_{\bar{\mathrm{t}}\to j} + \Gamma^{0}_{\mathrm{t}\to i}\,\Gamma^{1}_{\bar{\mathrm{t}}\to j}\right)\Big].
\end{aligned} \tag{2.11}$$

Rewriting (2.11) as a relative correction to (2.8) yields

$$\delta^{\mathrm{NLO}}_{\mathrm{trunc}} = \frac{\Delta\sigma^{\mathrm{NLO}}_{\mathrm{trunc}}}{\sigma^{\mathrm{NLO}}_{\mathrm{t\bar{t}}}\,\mathrm{BR}^{\mathrm{NLO}}_{\mathrm{t}\to i}\,\mathrm{BR}^{\mathrm{NLO}}_{\bar{\mathrm{t}}\to j}} = \left[x_i(1-x_j) + (1-x_i)x_j\right]\delta_{\mathrm{t\bar{t}}} + x_i x_j, \tag{2.12}$$

where the factors

$$\delta_{\mathrm{t\bar{t}}} = \frac{\sigma^{1}_{\mathrm{t\bar{t}}}}{\sigma^{\mathrm{NLO}}_{\mathrm{t\bar{t}}}} = 1 - \frac{\sigma^{0}_{\mathrm{t\bar{t}}}}{\sigma^{\mathrm{NLO}}_{\mathrm{t\bar{t}}}} \tag{2.13}$$

and

$$x_k = \frac{\Gamma^{1}_{\mathrm{t}\to k}}{\Gamma^{\mathrm{NLO}}_{\mathrm{t}\to k}} = 1 - \frac{\Gamma^{0}_{\mathrm{t}\to k}}{\Gamma^{\mathrm{NLO}}_{\mathrm{t}\to k}} \tag{2.14}$$

represent NLO corrections to $\mathrm{t\bar{t}}$ production and decay, respectively. For the case of a di-lepton final state, where $x_i = x_j = x$, Eq. (2.12) simplifies to

$$\delta^{\mathrm{NLO}}_{\mathrm{trunc}} = 2x(1-x)\delta_{\mathrm{t\bar{t}}} + x^2. \tag{2.15}$$

Since $x \simeq 10\%$ and $\delta_{\mathrm{t\bar{t}}} \simeq 10{-}30\%$, the correction $\delta^{\mathrm{NLO}}_{\mathrm{trunc}}$ can reach a few per cent and should thus be taken into account.

In the case of di-leptonic decays of the $t\bar{t}$ system, this can be achieved by using the approach of Refs. [29, 31], where the factor $(\Gamma_t^{\rm NLO})^{-2} = (\Gamma_t^0 + \Gamma_t^1)^{-2}$ in (2.7) is expanded and truncated at NLO. The corresponding differential NLO cross section reads

$$\begin{aligned} \mathrm{d}\sigma_{\rm exp}^{\rm NLO} = (\Gamma_t^0)^{-2} \; \Big[& \left(\mathrm{d}\sigma_{t\bar{t}}^0 + \mathrm{d}\sigma_{t\bar{t}}^1\right) \mathrm{d}\Gamma_{t\to i}^0 \, \mathrm{d}\Gamma_{\bar{t}\to j}^0 \\ & + \mathrm{d}\sigma_{t\bar{t}}^0 \left(\mathrm{d}\Gamma_{t\to i}^1 \, \mathrm{d}\Gamma_{\bar{t}\to j}^0 + \mathrm{d}\Gamma_{t\to i}^0 \, \mathrm{d}\Gamma_{\bar{t}\to j}^1 - 2\,\frac{\Gamma_t^1}{\Gamma_t^0}\, \mathrm{d}\Gamma_{t\to i}^0 \, \mathrm{d}\Gamma_{\bar{t}\to j}^0 \right) \Big]. \end{aligned} \tag{2.16}$$

Integrating over the full phase space, and expressing $\mathrm{d}\Gamma_{t\to k}^0$ and $\mathrm{d}\Gamma_{t\to k}^1$ in terms of the total top width and W-decay branching fractions via

$$\Gamma_{t\to k}^0 = \Gamma_t^0 \, \frac{\Gamma_{W\to k}^0}{\Gamma_W^0}, \qquad \frac{\Gamma_{t\to k}^1}{\Gamma_{t\to k}^0} = \frac{\Gamma_t^1}{\Gamma_t^0} + \frac{\Gamma_{W\to k}^1}{\Gamma_{W\to k}^0} - \frac{\Gamma_W^1}{\Gamma_W^0}, \tag{2.17}$$

one obtains the following expression, where the total and partial top-decay widths cancel out,

$$\begin{aligned} \int \mathrm{d}\sigma_{\rm exp}^{\rm NLO} &= \left[\sigma_{t\bar{t}}^0 + \sigma_{t\bar{t}}^1 + \sigma_{t\bar{t}}^0 \sum_{k=i,j} \left(\frac{\Gamma_{t\to k}^1}{\Gamma_{t\to k}^0} - \frac{\Gamma_t^1}{\Gamma_t^0} \right) \right] \prod_{k=i,j} \frac{\Gamma_{t\to k}^0}{\Gamma_t^0} \\ &= \left[\sigma_{t\bar{t}}^0 + \sigma_{t\bar{t}}^1 + \sigma_{t\bar{t}}^0 \sum_{k=i,j} \left(\frac{\Gamma_{W\to k}^1}{\Gamma_{W\to k}^0} - \frac{\Gamma_W^1}{\Gamma_W^0} \right) \right] \prod_{k=i,j} \frac{\Gamma_{W\to k}^0}{\Gamma_W^0}. \end{aligned} \tag{2.18}$$

Note that, consistently with the treatment of the top width in (2.16), we expanded the NLO W-width term in (2.17) as $1/\Gamma_W^{\rm NLO} = 1/\Gamma_W^0 - \Gamma_W^1/(\Gamma_W^0)^2$. Moreover, to be fully general, in (2.17) we also included corrections $\Gamma_{W\to k}^1$ to the W decays. Comparing (2.18) to the factorized expression (2.8) with NLO branching fractions

$$\mathrm{BR}_{t\to k}^{\rm NLO} = \frac{\Gamma_{t\to k}^{\rm NLO}}{\Gamma_t^{\rm NLO}} = \frac{\Gamma_t^{\rm NLO} \mathrm{BR}_{W\to k}^{\rm NLO}}{\Gamma_t^{\rm NLO}} = \frac{\Gamma_{W\to k}^0 + \Gamma_{W\to k}^1}{\Gamma_W^0 + \Gamma_W^1} \tag{2.19}$$

yields

$$\begin{aligned} \sigma_{t\bar{t}}^{\rm NLO} \, \mathrm{BR}_{t\to i}^{\rm NLO} \, \mathrm{BR}_{\bar{t}\to j}^{\rm NLO} - \int \mathrm{d}\sigma_{\rm exp}^{\rm NLO} &= \sigma_{t\bar{t}}^1 \left[\prod_{k=i,j} \frac{\Gamma_{W\to k}^0 + \Gamma_{W\to k}^1}{\Gamma_W^0 + \Gamma_W^1} - \prod_{k=i,j} \frac{\Gamma_{W\to k}^0}{\Gamma_W^0} \right] \\ + \sigma_{t\bar{t}}^0 \left\{ \prod_{k=i,j} \frac{\Gamma_{W\to k}^0 + \Gamma_{W\to k}^1}{\Gamma_W^0 + \Gamma_W^1} - \left[1 + \sum_{k=i,j} \left(\frac{\Gamma_{W\to k}^1}{\Gamma_{W\to k}^0} - \frac{\Gamma_W^1}{\Gamma_W^0} \right) \right] \prod_{k=i,j} \frac{\Gamma_{W\to k}^0}{\Gamma_W^0} \right\}. \end{aligned} \tag{2.20}$$

This indicates that, in general, the inclusive cross section resulting from (2.16) is not identical to (2.8). The mismatch (2.20) is formally of NNLO and is due to the corrections $\Gamma_{W\to k}^1$ to the exclusive W decays and to the fixed-order expansion of $1/(\Gamma_W^0 + \Gamma_W^1)$. Thus, if the W decays do not receive NLO corrections the fixed-order approach (2.16) can be reconciled with (2.8) by avoiding the fixed-order expansion of the W-width term, i.e. using $1/\Gamma_W^{\rm NLO} = 1/(\Gamma_W^0 + \Gamma_W^1)$ everywhere. This corresponds to replacing $1/\Gamma_W^0 \to 1/(\Gamma_W^0 + \Gamma_W^1)$ and omitting the Γ_W^1/Γ_W^0 term in (2.20).

In practice, this is applicable to di-lepton final states, but not to hadronically decaying top quarks or in presence of electroweak corrections. Therefore we prefer to ensure the validity of (2.8) at NLO in a different way. Instead of removing higher-order contributions by expanding and truncating the term $(\Gamma_{\rm t}^{\rm NLO})^{-2}$, which originates from the Dyson resummation of the top-quark self-energy in (2.4), we keep the exact NLO top-quark width everywhere and supplement our calculation by the missing higher-order contributions (2.11). This is done by correcting the normalization of the NLO $\mathrm{pp} \to \mathrm{t\bar{t}} \to ij$ cross section in NtWA,

$$\mathrm{d}\sigma_{\rm NtWA}^{\rm NLO^+} = (1+\delta^{\rm NLO^+})\mathrm{d}\sigma_{\rm NtWA}^{\rm NLO}, \tag{2.21}$$

with a matching factor

$$\delta^{\rm NLO^+} = \frac{\delta_{\rm trunc}^{\rm NLO}}{1-\delta_{\rm trunc}^{\rm NLO}} \tag{2.22}$$

that restores the consistency with the on-shell $\mathrm{t\bar{t}}$ total cross section, i.e.

$$\int \mathrm{d}\sigma_{\rm NtWA}^{\rm NLO^+} = \sigma_{\rm t\bar{t}}^{\rm NLO}\,\mathrm{BR}_{\rm t\to i}^{\rm NLO}\,\mathrm{BR}_{\rm \bar{t}\to j}^{\rm NLO}. \tag{2.23}$$

For the total cross section, the approximations (2.16) and (2.21) are fully equivalent (for di-lepton final states and if $\Gamma_{\rm W}^{\rm NLO}$ is used everywhere). However, they yield different predictions for exclusive observables, in which case we expect (2.21) to be more accurate, thanks to the presence of higher-order contributions.

The matching correction (2.22) guarantees a consistent inclusive cross section also in presence of FtW (and FwW) effects. In this case, for the corrected cross section

$$\mathrm{d}\sigma_{\nu_{\rm e}{\rm e}^+\mu^-\bar{\nu}_\mu{\rm b\bar{b}}}^{\rm NLO^+} = (1+\delta^{\rm NLO^+})\,\mathrm{d}\sigma_{\nu_{\rm e}{\rm e}^+\mu^-\bar{\nu}_\mu{\rm b\bar{b}}}^{\rm NLO}, \tag{2.24}$$

we have

$$\int \mathrm{d}\sigma_{\nu_{\rm e}{\rm e}^+\mu^-\bar{\nu}_\mu{\rm b\bar{b}}}^{\rm NLO^+} = \sigma_{\rm t\bar{t}}^{\rm NLO}\,\left(\mathrm{BR}_{\rm t\to l\nu_l b}^{\rm NLO}\right)^2 + \Delta\sigma_{\rm FtW}^{\rm NLO}, \tag{2.25}$$

which remains consistent with (2.8) for $\Gamma_{\rm t}\to 0$. Moreover, the matching procedure does not disturb the $\mathcal{O}(\Gamma_{\rm t}/m_{\rm t})$ finite-width contributions $\Delta\sigma_{\rm FtW}^{\rm NLO}$ to $\sigma_{\nu_{\rm e}{\rm e}^+\mu^-\bar{\nu}_\mu{\rm b\bar{b}}}$, since the interplay of these two corrections represents a suppressed NNLO effect of order $\delta^{\rm NLO^+}\Gamma_{\rm t}/m_{\rm t}$.

Finally, let us note that in order to determine the correction factor (2.13) that enters $\delta^{\rm NLO^+}$, instead of performing an explicit on-shell $\mathrm{t\bar{t}}$ calculation we use

$$1-\delta_{\rm t\bar{t}} = \frac{\sigma_{\rm t\bar{t}}^0}{\sigma_{\rm t\bar{t}}^{\rm NLO}} \simeq \frac{\int \mathrm{d}\sigma_{\rm t\bar{t}}^0\,\theta_{\rm cuts}}{\int \mathrm{d}\sigma_{\rm t\bar{t}}^{\rm NLO}\,\theta_{\rm cuts}} \simeq \frac{\int \mathrm{d}\sigma_{\nu_{\rm e}{\rm e}^+\mu^-\bar{\nu}_\mu{\rm b\bar{b}}}^0\,\theta_{\rm cuts}}{\int \mathrm{d}\sigma_{\nu_{\rm e}{\rm e}^+\mu^-\bar{\nu}_\mu{\rm b\bar{b}}}^{\rm NLO}\,\theta_{\rm cuts}} \left(\frac{\Gamma_{\rm t}^{\rm NLO}}{\Gamma_{\rm t}^{\rm LO}}\right)^2, \tag{2.26}$$

i.e. we replace the fully inclusive $\sigma_{\rm t\bar{t}}$ cross section by the $\nu_{\rm e}{\rm e}^+\mu^-\bar{\nu}_\mu{\rm b\bar{b}}$ cross section in presence of the (fairly inclusive) cuts specified in Section 3. By definition, the various σ^0 and $\sigma^{\rm NLO}$ cross sections in (2.26) must be evaluated using NLO PDFs, NLO $\alpha_{\rm s}$, and $\Gamma_{\rm t}^{\rm NLO}$, and the factor $\left(\Gamma_{\rm t}^{\rm NLO}/\Gamma_{\rm t}^{\rm LO}\right)^2$ on the r.h.s. of (2.26) compensates for the fact that, in order to match the l.h.s, $\mathrm{d}\sigma_{\nu_{\rm e}{\rm e}^+\mu^-\bar{\nu}_\mu{\rm b\bar{b}}}^0$ should be computed with a LO top-quark width. We expect the above approximation to be quite precise since the mismatch between the

$\mathrm{t\bar{t}}$ and $\nu_\mathrm{e}\mathrm{e}^+\mu^-\bar{\nu}_\mu\mathrm{b\bar{b}}$ NLO cross sections in (2.26) induces a strongly suppressed error of order $(\delta^{\mathrm{NLO}^+})^2$ in $\sigma^{\mathrm{NLO}^+}_{\nu_\mathrm{e}\mathrm{e}^+\mu^-\bar{\nu}_\mu\mathrm{b\bar{b}}}$. Moreover, cut and finite-width effects in (2.26) cancel to a large extent in the ratios and are further suppressed by the factor $2x(1-x)$ in (2.15).

In the derivation of the above NLO^+ correction factor we implicitly assumed that the top-quark width input parameter and the matrix elements are evaluated at the same QCD scale. However, while m_t represents the natural scale choice to compute $\Gamma_\mathrm{t}^\mathrm{NLO}$, in general the matrix elements for $\nu_\mathrm{e}\mathrm{e}^+\mu^-\bar{\nu}_\mu\mathrm{b\bar{b}}$ production might be evaluated using a different scale μ, like the dynamical scale proposed in Section 3.2, which adapts to the hard scale of the $\mathrm{t\bar{t}}$ production part of the process. Since the scale μ also enters the top-decay part of the matrix elements, a scale choice $\mu \neq m_\mathrm{t}$ implies that partial and total top-decay widths are evaluated at different scales. This mismatch can be compensated by redefining the NLO differental cross section as

$$\mathrm{d}\sigma^\mathrm{NLO}_{\nu_\mathrm{e}\mathrm{e}^+\mu^-\bar{\nu}_\mu\mathrm{b\bar{b}}}\Big|_\mathrm{PWC} = \left(\frac{\Gamma_\mathrm{t}^\mathrm{NLO}(m_\mathrm{t})}{\Gamma_\mathrm{t}^\mathrm{NLO}(\mu)}\right)^2 \mathrm{d}\sigma^\mathrm{NLO}_{\nu_\mathrm{e}\mathrm{e}^+\mu^-\bar{\nu}_\mu\mathrm{b\bar{b}}}, \tag{2.27}$$

where the overall factor $(\Gamma_\mathrm{t}^\mathrm{NLO}(m_\mathrm{t})/\Gamma_\mathrm{t}^\mathrm{NLO}(\mu))^2$ effectively restores $\mu \to m_\mathrm{t}$ in the partial decay widths. The (dynamical or fixed) scale μ is the one used in the matrix elements, including variations in scale-dependence studies. The relative shift of the NLO cross section induced by the correction (2.27) amounts to about $-0.02 \times (\mu/m_\mathrm{t} - 1)$ for $\mu/m_\mathrm{t} \sim 1$. In principle this correction can be applied to all NLO predictions. However, we decided to present fixed-order NLO results in a more conventional way (scale μ in matrix elements and $\Gamma_\mathrm{t}^\mathrm{NLO}$ at the fixed scale m_t) and to include the above correction only in NLO^+ predictions. To this end, we evaluate (2.24) and (2.26) using "partial-width corrected" NLO predictions (2.27). In presence of a dynamical scale, $\mu = \mu_\mathrm{dyn}$, instead of a phase-space-dependent correction we apply a constant factor $\Gamma_\mathrm{t}^\mathrm{NLO}(m_\mathrm{t})/\Gamma_\mathrm{t}^\mathrm{NLO}(\bar{\mu}_\mathrm{dyn})$ evaluated at the logarithmic average of μ_dyn (see Table 1).

2.1.3 Treatment of unstable W bosons

To describe the leptonic W-boson decays, $\mathrm{W}^+ \to \nu_\mathrm{e}\mathrm{e}^+$ and $\mathrm{W}^- \to \mu^-\bar{\nu}_\mu$, we employ two different approaches: a spin-correlated NwWA and, alternatively, the full set of diagrams contributing to $\nu_\mathrm{e}\mathrm{e}^+\mu^-\bar{\nu}_\mu\mathrm{b\bar{b}}$ production. Analogously to the case of top-quark decays, the NwWA includes only contributions with two on-shell W bosons, while the FwW calculation involves additional effects from off-shell W bosons and from singly-resonant $\nu_e\mathrm{e}^+\mu^-\bar{\nu}_\mu$ production.[4] In NwWA, the effect of the W-boson width is retained only in the W propagators—approximated by $\pi/(M_\mathrm{W}\Gamma_\mathrm{W})\delta(p_\mathrm{W}^2 - M_\mathrm{W}^2)$— while elsewhere we set $\Gamma_\mathrm{W} = \Gamma_\mathrm{Z} = 0$ and use real-valued parameters M_W and M_Z. In the alternative calculation with the full set of diagrams, to include FwW effects we employ the complex-mass scheme, i.e. we use complex W- and Z-boson masses and a corresponding complex-valued weak mixing angle,

$$\mu_\mathrm{W}^2 = M_\mathrm{W}^2 - \mathrm{i}M_\mathrm{W}\Gamma_\mathrm{W}, \quad \mu_\mathrm{Z}^2 = M_\mathrm{Z}^2 - \mathrm{i}M_\mathrm{Z}\Gamma_\mathrm{Z}, \quad c_\mathrm{w} = \sqrt{1 - s_\mathrm{w}^2} = \frac{\mu_\mathrm{W}}{\mu_\mathrm{Z}}. \tag{2.28}$$

[4] All channels contributing to $\nu_\mathrm{e}\mathrm{e}^+\mu^-\bar{\nu}_\mu\mathrm{b\bar{b}}$ production involve at least one resonant W boson.

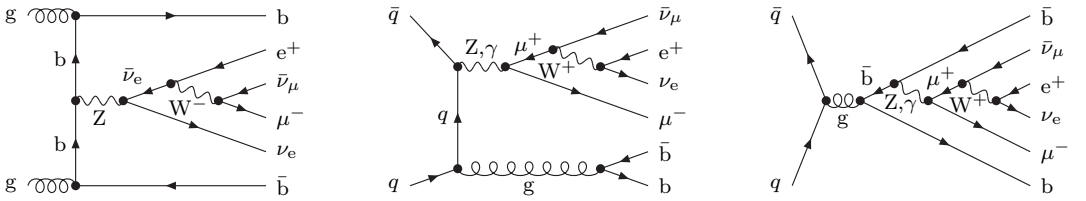

Figure 2: Examples of LO diagrams that involve a single W-boson resonance and contribute to the FwW corrections.

Examples of tree diagrams in NwWA and additional singly-resonant diagrams contributing to the FwW calculation are shown in Figure 1 and Figure 2, respectively. In all singly-resonant diagrams, the four-lepton final state originates from $\mathrm{Z},\gamma \to \nu_e \mathrm{e}^+\mu^-\bar{\nu}_\mu$ subtopologies involving one intermediate s-channel W^+ or W^- propagator. We note that such topologies do not involve any top-quark resonance and are thus expected to be strongly suppressed. Their inclusion increases the number of LO diagrams in the $q\bar{q}$ (gg) channel from 14 (31) to 38 (79).

At NLO, a resonant W-boson pair decaying into $\nu_e \mathrm{e}^+\mu^-\bar{\nu}_\mu$ does not receive (factorizable or non-factorizable) QCD corrections. This renders the inclusion of FwW effects fairly straightforward, as compared to the case of FtW effects. Since FwW contributions are strongly suppressed already at LO (see Section 3), we adopt a double-pole approximation to include FwW effects in the *infrared-finite part* of the virtual QCD corrections, which is defined by the sum of the virtual corrections and the contribution of the I-operator of the real corrections in the dipole subtraction approach [56, 59]. This approach, which is discussed in Section 2.2.7, involves only doubly-W-resonant diagrams. Similarly as in NwWA, the matrix elements in double-pole approximation are evaluated with on-shell W bosons and using $\Gamma_\mathrm{W} = \Gamma_\mathrm{Z} = 0$ and real W- and Z-boson masses everywhere, apart from the W propagator. The latter reads $1/(p^2_\mathrm{W} - M^2_\mathrm{W} + \mathrm{i}\Gamma_\mathrm{W} M_\mathrm{W})$ and takes into account off-shell-W effects. Apart from the (finite part of the) virtual corrections, in all other NLO contributions FwW effects are included exactly, using the complex-mass scheme (2.28).

For what concerns the expected magnitude of FwW contributions to inclusive $\mathrm{t\bar{t}}$ observables, one might naively expect an impact of order $\Gamma_\mathrm{W}/M_\mathrm{W} \simeq 2.5\%$, i.e. three times larger than the typical size of FtW effects. However, more careful considerations indicate that the consistent inclusion of FwW corrections in matrix elements and input parameters leads to doubly-suppressed contributions of $\mathcal{O}(\frac{\Gamma_\mathrm{W}\Gamma_\mathrm{t}}{M_\mathrm{W} m_\mathrm{t}})$ in the inclusive cross section. This is due to the fact that, in the $\Gamma_\mathrm{t} \to 0$ limit, the only contribution to the inclusive $\nu_\mathrm{e}\mathrm{e}^+\mu^-\bar{\nu}_\mu \mathrm{b\bar{b}}$ cross section (2.25) that involves W-boson decays, and is thus sensitive to Γ_W, is the branching ratio

$$\mathrm{BR}^{\mathrm{NLO}}_{\mathrm{t}\to l\nu_l \mathrm{b}} = \frac{\int \mathrm{d}\Gamma^{\mathrm{NLO}}_{\mathrm{t}\to l\nu_l \mathrm{b}}}{\Gamma^{\mathrm{NLO}}_\mathrm{t}}. \tag{2.29}$$

Moreover, owing to the identical Γ_W dependence of the numerator and denominator of (2.29)—which correspond to the integrated top-decay matrix elements and the Γ_t input parameter in our calculation—FwW corrections cancel in the branching ratio. Thus the

consistent inclusion of FwW corrections—in the $ab \to \nu_e e^+ \mu^- \bar{\nu}_\mu b\bar{b}(c)$ matrix elements and in the calculation of the Γ_t input parameter—does not affect the leading contribution to (2.25) and yields only tiny corrections of $\mathcal{O}(\frac{\Gamma_W \Gamma_t}{M_W m_t})$ to the fully inclusive cross section. These considerations do not depend on the inclusion of the matching correction (2.24) and remain valid also in presence of contributions of type (2.11), which violate (2.8). We also point out that omitting FwW effects in the top-quark width used as input parameter would induce a fake FwW shift of $\mathcal{O}(\Gamma_W/M_W)$ in the integrated cross section.

The validity of the double-suppression mechanism is restricted to the case where the top-decay phase spaces are fully integrated over, and the presence of cuts is expected to lead to additional FwW effects resulting from the incomplete cancellation of $\mathcal{O}(\Gamma_W/M_W)$ corrections to the numerator and denominator of (2.29). However, as long as the cuts are rather inclusive, also such FwW effects are expected to remain well below $\mathcal{O}(\Gamma_W/M_W)$. This justifies the approach of Ref. [32], where off-shell and non-resonant contributions of the top quark to $W^+W^-b\bar{b}$ production were combined with W-boson decays in NwWA.

For very exclusive observables, in contrast, it is important to investigate whether FwW corrections can become non-negligible. To this end, in this paper we study FwW effects by comparing several distributions obtained in NwWA and with the FwW variant of our calculation. While FwW effects have already been included in the predictions of Ref. [33], our study provides the first quantitative assessment of the precision of the NwWA in $\nu_e e^+ \mu^- \bar{\nu}_\mu b\bar{b}$ production.

2.2 Virtual corrections

2.2.1 Diagram-by-diagram approach

The sum of the LO and virtual contributions to the partonic cross section is derived from the LO and one-loop matrix elements $\mathcal{M}_0$ and $\mathcal{M}_1$ according to

$$\int_6 \mathrm{d}\hat{\sigma}_{0,ab} + \int_6 \mathrm{d}\hat{\sigma}_{\mathrm{virt},ab} = \frac{1}{2\hat{s}} \int \mathrm{d}\Phi_6 \left\{ \sum_{\mathrm{col}} \sum_{\mathrm{pol}} |\mathcal{M}_{0,ab}|^2 + \sum_{\mathrm{col}} \sum_{\mathrm{pol}} 2\,\mathrm{Re}\Big(\mathcal{M}_{1,ab}\, \mathcal{M}^*_{0,ab} \Big) \right\}, \tag{2.30}$$

where the squared partonic centre-of-mass (CM) energy $\hat{s}$ appears in the overall flux factor $1/(2\hat{s})$ and $\mathrm{d}\Phi_6$ is the phase-space element of the six-particle final state. The sums run over all colour and helicity states and implicitly include the averaging over initial-state colours and helicities. We calculate the amplitudes $\mathcal{M}_0$ and $\mathcal{M}_1$ for $q\bar{q}/\mathrm{gg} \to W^+W^-b\bar{b} \to \nu_e e^+ \mu^- \bar{\nu}_\mu b\bar{b}$ in terms of explicit Feynman diagrams and algebraically reduce the one-loop diagrams to spin structures ("standard matrix elements") and standard one-loop tensor integrals, which are subsequently evaluated numerically, as described in more detail below.

The $q\bar{q}$ and gg channels comprise 294 and 795 one-loop diagrams, respectively (see examples in Figure 3).[5] The most complicated ones are the 96 pentagons and 21 hexagons that contribute to the gg channel and involve tensor integrals up to rank five. Feynman diagrams are generated with two independent versions of FeynArts [69, 70], and one-loop amplitudes are reduced as already described for $pp \to t\bar{t}b\bar{b}$ in Refs. [71, 72] using two

[5] While our calculation includes the contributions of all three quark generations, we count diagrams with closed fermion loops only for a single generation.

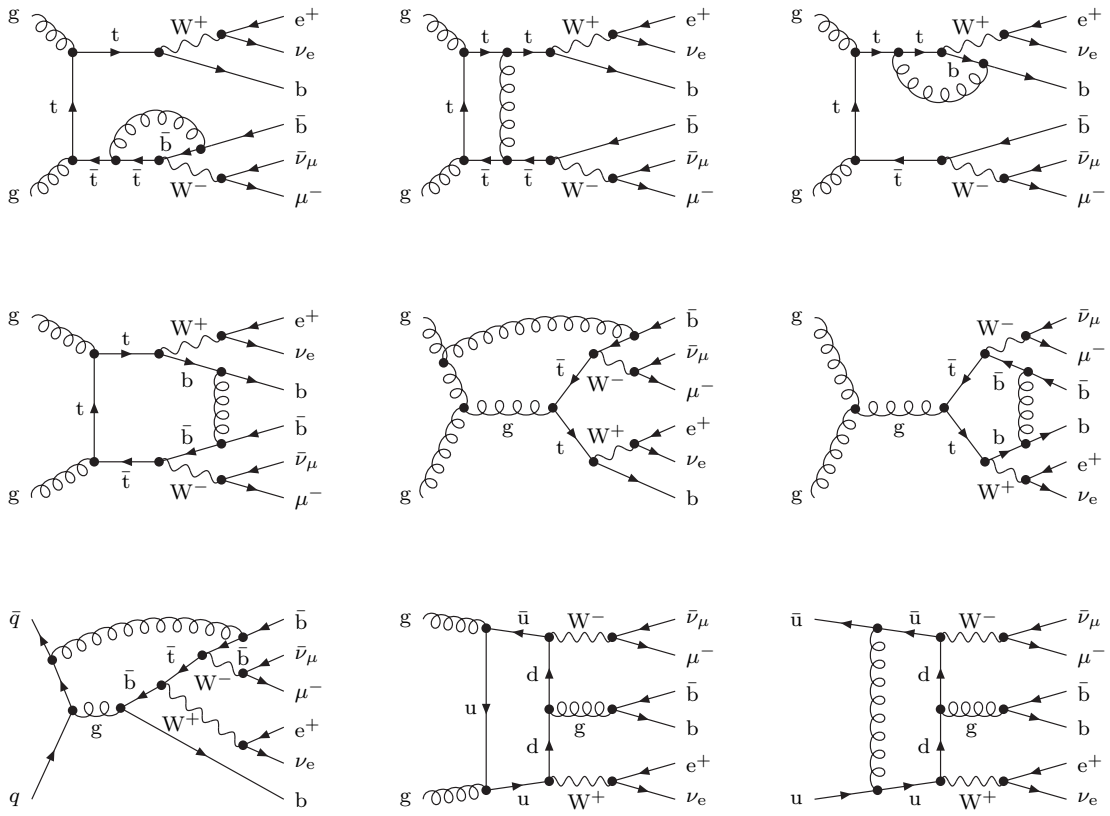

Figure 3: Examples of one-loop diagrams contributing to $q\bar{q}/gg \to W^+W^-b\bar{b} \to \nu_e e^+ \mu^- \bar{\nu}_\mu b\bar{b}$: doubly-top-resonant diagrams with corrections to $t\bar{t}$ production or decay (first line), non-factorizable pentagons and hexagons with two top-quark resonances (second line), pentagons and hexagons with less than two top resonances (third line).

in-house MATHEMATICA programs, one of which relies on FORMCALC [73] for preliminary manipulations.

The employed approach strongly mitigates the complexity inherent in Feynman diagrams by exploiting factorization of colour matrices, reduction of helicity structures to compact spinor chains, and recycling a multitude of common subexpressions. The reduced expressions are automatically converted into FORTRAN77 programs that evaluate colour/helicity summed quantities with very high CPU efficiency.

The virtual corrections are obtained from the interference of the one-loop and LO matrix elements summed over external-state colours and helicities on a diagram-by-diagram basis.

2.2.2 Colour factorization

One of the key features of the diagram-by-diagram approach is that the cost related to the large number of diagrams is compensated by the possibility to perform colour sums

very efficiently. This is a consequence of colour factorization: individual (sub)diagrams, Γ, consist of a single colour-stripped amplitude $\mathcal{A}^{(\Gamma)}$ multiplied by a single colour factor $\mathcal{C}^{(\Gamma)}$,

$$\mathcal{M}^{(\Gamma)} = \mathcal{A}^{(\Gamma)}\mathcal{C}^{(\Gamma)}. \tag{2.31}$$

More precisely, each diagram gives rise to 3^{n_4} colour-factorized contributions of type (2.31), where n_4 is the number of quartic gluon vertices in the diagram. These terms are handled as separate subdiagrams. However, most diagrams do not involve quartic couplings, and their colour structures factorize completely. The colour factor $\mathcal{C}^{(\Gamma)}$ can be linearly decomposed in terms of a fixed basis of colour structures $\mathcal{C}_k$,

$$\mathcal{C}^{(\Gamma)} = \sum_k c_k^{(\Gamma)} \mathcal{C}_k, \tag{2.32}$$

where the coefficients $c_k^{(\Gamma)}$ are just a set of numbers for each diagram Γ. For the $q\bar{q}$ and gg channels there are only 2 and 3 different colour structures, respectively, which may be taken to be

$$\begin{aligned} &\mathcal{C}_1^{q\bar{q}} = T^c_{c_{\bar{q}}c_q} T^c_{c_{\mathrm{b}}c_{\bar{\mathrm{b}}}}, \qquad \mathcal{C}_2^{q\bar{q}} = \delta_{c_{\bar{q}}c_q}\delta_{c_{\mathrm{b}}c_{\bar{\mathrm{b}}}}, \\ &\mathcal{C}_1^{\mathrm{gg}} = \delta_{ab}\delta_{c_{\mathrm{b}}c_{\bar{\mathrm{b}}}}, \qquad \mathcal{C}_2^{\mathrm{gg}} = \mathrm{i}f_{abc}T^c_{c_{\mathrm{b}}c_{\bar{\mathrm{b}}}}, \qquad \mathcal{C}_3^{\mathrm{gg}} = d_{abc}T^c_{c_{\mathrm{b}}c_{\bar{\mathrm{b}}}}. \end{aligned} \tag{2.33}$$

Here a, b and c_i denote the colour indices of the two incoming gluons and the fermion i, respectively, T^c are the group generators in the fundamental (quark) representation, and f_{abc}, d_{abc} are the usual SU(3) constants.

The summation over external colours is performed once and for all at the level of the colour basis and the LO matrix element. To this end, we compute the colour-interference matrix

$$I_{kl} = \sum_{\mathrm{col}} \mathcal{C}_k \mathcal{C}_l^*, \tag{2.34}$$

and, reducing the full tree matrix element in colour space,

$$\mathcal{M}_0 = \sum_l \mathcal{M}_l^{(\mathrm{LO})} \mathcal{C}_l, \tag{2.35}$$

we build the interference of $\mathcal{M}_0$ with the elements of the colour basis as

$$\tilde{\mathcal{M}}_k^{(\mathrm{LO})} = \sum_{\mathrm{col}} \mathcal{C}_k \mathcal{M}_0^* = \sum_l I_{kl} \left(\mathcal{M}_l^{(\mathrm{LO})}\right)^*. \tag{2.36}$$

Then, upon reduction of the factorized colour structure of the loop diagrams,

$$\mathcal{M}^{(\Gamma)} = \mathcal{A}^{(\Gamma)}\mathcal{C}^{(\Gamma)} = \mathcal{A}^{(\Gamma)} \left(\sum_k c_k^{(\Gamma)} \mathcal{C}_k \right), \tag{2.37}$$

we obtain the colour-summed interference between $\mathcal{M}_0^*$ and the complete one-loop amplitude $\mathcal{M}_1 = \sum_\Gamma \mathcal{M}^{(\Gamma)}$ as

$$\sum_{\mathrm{col}} \mathcal{M}_1 \mathcal{M}_0^* = \sum_{\mathrm{col}} \sum_\Gamma \mathcal{M}^{(\Gamma)} \mathcal{M}_0^* = \sum_\Gamma \mathcal{A}^{(\Gamma)} \left(\sum_k c_k^{(\Gamma)} \tilde{\mathcal{M}}_k^{(\mathrm{LO})} \right). \tag{2.38}$$

The colour-summed result is given by a combination of previously computed colour–Born interference terms (2.36). For each phase-space point, this requires *a single evaluation* of the non-trivial colour-stripped amplitude $\mathcal{A}^{(\Gamma)}$ of each (sub)diagram.

2.2.3 Algebraic reduction of helicity structures and helicity sums

The helicity structures encountered in the explicit evaluation of all Feynman diagrams are algebraically reduced to a common basis of standard matrix elements (SMEs). The general form of SMEs for the $a(k_1)b(k_2) \to \mathrm{W}^+(k_3)\mathrm{W}^-(k_4)\mathrm{b}(k_5)\bar{\mathrm{b}}(k_6)$ channel for the initial states $ab = q\bar{q}/\mathrm{gg}$ is

$$\begin{aligned}
\hat{\mathcal{M}}^{q\bar{q}}_{m,\sigma\tau} &= Q^{\nu_1\ldots\nu_l}_{m;\mu_3\mu_4}\Big[\bar{v}_{\bar{q}}(k_1)\gamma_{\nu_1}\ldots\gamma_{\nu_k}\omega_\sigma u_q(k_2)\Big]\varepsilon^{\mu_3*}_{\mathrm{W}^+}(k_3)\varepsilon^{\mu_4*}_{\mathrm{W}^-}(k_4) \\
&\quad\times\Big[\bar{v}_{\mathrm{b}}(k_5)\gamma_{\nu_{k+1}}\ldots\gamma_{\nu_l}\omega_\tau u_{\bar{\mathrm{b}}}(k_6)\Big], \\
\hat{\mathcal{M}}^{\mathrm{gg}}_{m,\tau} &= Q^{\nu_1\ldots\nu_l}_{m;\mu_1\ldots\mu_4}\varepsilon^{\mu_1}_{\mathrm{g}}(k_1)\varepsilon^{\mu_2}_{\mathrm{g}}(k_2)\varepsilon^{\mu_3*}_{\mathrm{W}^+}(k_3)\varepsilon^{\mu_4*}_{\mathrm{W}^-}(k_4)\left[\bar{v}_{\mathrm{b}}(k_5)\gamma_{\nu_1}\ldots\gamma_{\nu_l}\omega_\tau u_{\bar{\mathrm{b}}}(k_6)\right],
\end{aligned} \tag{2.39}$$

where $Q^{\nu_1\ldots\nu_l}_{m;\mu_3\mu_4}$ and $Q^{\nu_1\ldots\nu_l}_{m;\mu_1\ldots\mu_4}$ consist of combinations of metric tensors and external momenta, and $\sigma,\tau = \pm$ refer to the chirality projectors $\omega_\pm = (1\pm\gamma_5)/2$. In the double-pole approximation (see Section 2.2.7), W-boson decays are described via effective polarisation vectors

$$\begin{aligned}
\varepsilon^{\mu*}_{\mathrm{W}^+}(k_3) &= \frac{e\,\bar{u}(k_{\nu_\mathrm{e}})\gamma^\mu\omega_- v(k_{\mathrm{e}^+})}{\sqrt{2}s_\mathrm{w}\Big((k_{\nu_\mathrm{e}}+k_{\mathrm{e}^+})^2 - M^2_\mathrm{W} + \mathrm{i}M_\mathrm{W}\Gamma_\mathrm{W}\Big)}, \\
\varepsilon^{\mu*}_{\mathrm{W}^-}(k_4) &= \frac{e\,\bar{u}(k_{\mu^-})\gamma^\mu\omega_- v(k_{\bar{\nu}_\mu})}{\sqrt{2}s_\mathrm{w}\Big((k_{\mu^-}+k_{\bar{\nu}_\mu})^2 - M^2_\mathrm{W} + \mathrm{i}M_\mathrm{W}\Gamma_\mathrm{W}\Big)},
\end{aligned} \tag{2.40}$$

which include the left-handed lepton currents and the W-boson propagators. In our calculation we encounter about 800 and 2000 SMEs for the $q\bar{q}$ and gg channels, respectively. These compact spinor chains permit to decouple helicity information from the remnant parts of the diagrams, so that helicity sums can be performed in a diagram-independent and efficient way. In practice, the colour-stripped part of each loop diagram [see (2.37)] is expressed as a linear combination of SMEs and tensor integrals,

$$\begin{aligned}
\mathcal{A}^{(\Gamma)} &= \sum_m \mathcal{F}^{(\Gamma)}_m \hat{\mathcal{M}}_m, \\
\mathcal{F}^{(\Gamma)}_m &= \sum_P \sum_{j_1,\ldots,j_P=0}^{N-1} \mathcal{K}^{(\Gamma)}_{m;j_1\ldots j_P} T^N_{j_1\ldots j_P} \;+\; \text{rational parts},
\end{aligned} \tag{2.41}$$

where the index m here also includes the chirality indices σ,τ. The coefficients $\mathcal{K}^{(\Gamma)}_{m;j_1\ldots j_P}$ are rational functions of the kinematic invariants. These functions involve only denominators from intermediate-particle propagators and are free of spurious poles that might generate numerical instabilities. The functions $T^N_{j_1\ldots j_P}$ are the coefficients of the one-loop tensor integrals, whose evaluation is briefly described below.

Helicity sums are performed at the level of the interference of the diagram-independent SMEs with the colour-projected Born amplitude (2.36),

$$M_{km} = \sum_{\text{hel}} \hat{\mathcal{M}}_m \tilde{\mathcal{M}}_k^{(\text{LO})} = \sum_l I_{kl} \sum_{\text{hel}} \hat{\mathcal{M}}_m \left(\mathcal{M}_l^{(\text{LO})}\right)^* . \tag{2.42}$$

This matrix is computed only once per phase-space point employing the Weyl–van der Waerden spinor formalism of Ref. [74]. Using M_{km} one can directly obtain the colour- and helicity-summed contributions of each loop diagram in terms of its colour- and helicity-independent form factors $\mathcal{F}_m^{(\Gamma)}$ and the coefficients $c_k^{(\Gamma)}$ of its factorized colour structure (2.37),

$$\sum_{\text{col}} \sum_{\text{hel}} \mathcal{M}_1 \mathcal{M}_0^* = \sum_{\text{col}} \sum_{\text{hel}} \sum_{\Gamma} \mathcal{M}^{(\Gamma)} \mathcal{M}_0^* = \sum_{\Gamma} \sum_m \mathcal{F}_m^{(\Gamma)} \left(\sum_k c_k^{(\Gamma)} M_{km} \right) . \tag{2.43}$$

2.2.4 Covariant decomposition and numerical reduction of tensor integrals

Tensor one-loop integrals with N propagators and P Lorentz indices are expressed in terms of totally symmetric covariant structures $\{g \dots gp \dots p\}_{j_1 \dots j_P}^{\mu_1 \dots \mu_P}$ involving $g^{\mu\nu}$ and the external momenta $p_1, \dots, p_{N-1}$,

$$\frac{(2\pi\mu)^{4-D}}{\mathrm{i}\pi^2} \int \mathrm{d}^D q \, \frac{q^{\mu_1} \dots q^{\mu_P}}{\prod_{i=0}^{N-1} [(q+p_i)^2 - m_i^2 + \mathrm{i}0]} = \sum_{j_1,\dots,j_P=0}^{N-1} T^N_{j_1 \dots j_P} \, \{g \dots gp \dots p\}_{j_1 \dots j_P}^{\mu_1 \dots \mu_P} , \tag{2.44}$$

with D denoting the number of space–time dimensions. For details of the notation we refer to Ref. [53]. To describe N-point integrals with $N \geq 5$, tensor structures with only four external momenta would be sufficient. However, in order to avoid potential instabilities due to inverse Gram determinants we use a redundant set of structures, including the metric tensor and $N-1$ momenta.

The virtual corrections to $q\bar{q} \to \mathrm{W^+W^-b\bar{b}}$ and $\mathrm{gg} \to \mathrm{W^+W^-b\bar{b}}$ involve tensor integrals up to ranks $P = 4$ and $P = 5$, respectively. As sketched above, the one-loop amplitudes are expressed as linear combinations of tensor-integral coefficients $T^N_{j_1,\dots,j_P}$. The latter are evaluated by *numerical* libraries that recursively reduce them to master integrals using the methods of Refs. [52, 53]. Avoiding an explicit reduction of analytic expressions to master integrals, this numerical approach prevents prohibitively large expressions and permits to adapt the reduction strategy to the specific numerical problems that appear in different phase-space regions.

Tensor N-point integrals with $N \geq 5$ are expressed in terms of lower-rank and lower-point integrals exploiting the four-dimensionality of space–time [52, 53].[6] The tensor rank and the number of propagators are simultaneously reduced without introducing inverse Gram determinants. Consequently, the maximal power of inverse Gram determinants resulting from the entire reduction is given by the maximal rank of four-point integrals, which never exceeds four in renormalizable gauges. Scalar hexagons and pentagons are reduced to boxes using Melrose's method [77]. Tensor 4-point and 3-point integrals are

[6] Similar reductions are described in Refs. [75, 76].

reduced to scalar integrals with the Passarino–Veltman algorithm [78] as long as no small Gram determinant appears in the reduction. If small Gram determinants occur, alternative schemes are applied [53].[7] More precisely, we make use of expansions of the tensor coefficients about the limit of vanishing Gram determinants and possibly other kinematical determinants. One- and two-point tensor integrals are obtained with numerically stable analytic expressions.

Ultraviolet (UV) divergences are regularized dimensionally throughout, but infrared (IR) divergences are treated in different variants, which comprise pure dimensional regularization with strictly massless light quarks and a hybrid scheme with small quark masses and massless gluons. The corresponding scalar integrals are evaluated using the methods and results of Refs. [54, 55, 81], and different regularization schemes are translated into each other as described in Ref. [82].

The calculation of tensor integrals is implemented in two independent FORTRAN libraries. This permits to perform detailed cross checks, which confirm the excellent numerical stability of the reduction procedure. An automatic cache system is implemented that strongly boosts the reduction by recycling a multitude of tensor integrals among Feynman diagrams with common sub-topologies.

2.2.5 Rational parts

In $D = 4 - 2\epsilon$ dimensions, UV-singular tensor integrals give rise to $1/\epsilon_{\mathrm{UV}}$ poles and UV-finite remainders $\hat{T}^N_{j_1\dots j_P}$,

$$T^N_{j_1\dots j_P} = \hat{T}^N_{j_1\dots j_P} + \frac{R^N_{j_1\dots j_P}}{\epsilon_{\mathrm{UV}}}. \tag{2.45}$$

Consequently, their D-dependent prefactors $f(D)$ need to be expanded in $D - 4$,

$$f(D)T^N_{j_1\dots j_P} = f(4)T^N_{j_1\dots j_P} - 2f'(4)R^N_{j_1\dots j_P}, \tag{2.46}$$

resulting in so-called rational terms that are proportional to the pole residues $R^N_{j_1\dots j_P}$. Rational contributions originate from D-dependent terms in tensor-reduction identities and in the loop-momentum-independent part of the diagram numerators.

We employ the treatment of rational terms of ultraviolet or infrared origin as described in Appendix A of Ref. [71]. We use the fact (proven in Appendix A of Ref. [71]) that in the 't Hooft–Feynman gauge and similar gauge fixings rational terms of IR origin cancel in truncated one-loop amplitudes and only contribute via wave-function renormalization factors. Rational terms of UV origin are obtained in a straightforward way by performing the relevant expansions about $D = 4$ automatically by means of a catalogue of residues of UV poles (see e.g. Ref. [53]).

2.2.6 Treatment of unstable top quarks

The presence of intermediate unstable top quarks in $h_1h_2 \to \mathrm{W^+W^-b\bar{b}} \to \nu_\mathrm{e}\mathrm{e}^+\mu^-\bar{\nu}_\mu\mathrm{b\bar{b}}$ represents a non-trivial new aspect as compared to previous NLO QCD studies of multi-particle processes. To regularize intermediate top-quark resonances in a gauge-invariant

[7] Similar procedures based on numerical evaluations of specific one-loop integrals [75, 79] or expansions in small determinants [80] have also been proposed by other authors.

way, we employ the complex-mass scheme [51]. In this approach the top-quark width Γ_t is incorporated into the definition of the renormalized (squared) top-quark mass (2.3). This complex parameter μ_t^2 is identified with the position of the pole of the top-quark propagator, and the top-mass counterterm $\delta\mu_t$ is related to the top-quark self-energy at $p_t^2 = \mu_t^2$ via [51]

$$\frac{\delta\mu_t}{\mu_t} = \frac{1}{2}\left[\Sigma^{t,R}(\mu_t^2) + \Sigma^{t,L}(\mu_t^2) + 2\Sigma^{t,S}(\mu_t^2)\right], \tag{2.47}$$

where $\Sigma^{t,R}$, $\Sigma^{t,L}$, and $\Sigma^{t,S}$ are the left-handed, right-handed, and scalar parts of the top self-energy, respectively. This yields the one-loop counterterm

$$\frac{\delta\mu_t}{\mu_t} = -\frac{\alpha_s}{\pi}\left[\frac{(4\pi)^\epsilon\Gamma(1+\epsilon)}{\epsilon} + \ln\left(\frac{\mu^2}{\mu_t^2}\right) + \frac{4}{3}\right] \tag{2.48}$$

in $D = 4-2\epsilon$ dimensions, where μ is the reference scale of dimensional regularization. The evaluation of one-loop scalar box integrals in the presence of complex masses represents another non-trivial aspect of the complex-mass scheme. In our calculation we employ the results of Ref. [55], where explicit analytic continuations of box integrals have been presented for all kinematic configurations that are relevant for physical processes.

2.2.7 On-shell projection for off-shell W bosons

As discussed in Section 2.1.3, we treat the leptonic W-boson decays in (spin-correlated) NwWA and, alternatively, including also FwW effects. In the latter case, we employ exact LO and real-emission amplitudes—including all non-resonant and off-shell effects resulting from the FwW—together with the one-loop matrix elements and the I-operator from dipole subtraction in "double-pole approximation" (DPA). The DPA represents the leading contribution in an expansion of the corresponding matrix elements around the resonance poles in the W-boson propagators.

The pole expansion is based on the idea [83, 84] to separate the resonant part of an amplitude $\mathcal{M}$ which peaks at $p^2 \sim M^2$ in the following way,

$$\mathcal{M}(p) = \frac{R(p^2)}{p^2 - M^2} + N(p^2) = \frac{R(M^2)}{p^2 - M^2} + \frac{R(p^2) - R(M^2)}{p^2 - M^2} + N(p^2), \tag{2.49}$$

where $R(M^2)$ is the gauge-independent residue of the resonance and the non-resonant contributions from $R(p^2) - R(M^2)$ and $N(p^2)$ are neglected in DPA. A consistent implementation of this idea, however, involves some complications, in particular, if two resonances instead of one are involved. Nevertheless this concept was very successfully applied, for instance, to W-pair production in e^+e^- annihilation at LEP2, as e.g. reviewed in Ref. [85]. Here we follow the "hybrid concept" of Ref. [86], where only the IR-finite virtual corrections are treated in DPA, while keeping the lowest-order and the remaining real-emission matrix elements fully off shell. One of the mentioned subtleties concerns the appearance of so-called non-factorizable corrections, which involve non-analytic terms like $\ln(p^2 - M^2)$ in the resonance region. Such terms are ignored in the naive equation (2.49); they are caused by soft photon or gluon exchange between production and decay processes that are linked by the resonance. In our case, such non-factorizable corrections

do not appear, since we consider QCD corrections in combination with purely leptonic W-boson decays, i.e. there is no gluon exchange between W production and decay. Thus, only so-called factorizable corrections are relevant for us, which are just the corrections to the residue $R(M^2)$.

In this context, a second subtlety arises in the evaluation of $R(M^2)/(p^2-M^2)$ concerning the kinematics. The residue $R(p^2)$ typically depends on the momenta of all involved particles, and the consistent substitution $p^2 \to M^2$ requires a deformation of momenta on the full off-shell phase space of the reaction. This "on-shell projection" is needed in order to define a gauge-invariant set of corrections and maps each phase-space point into an associated phase-space point with on-shell W bosons. This procedure actually involves some freedom, but this ambiguity changes the results only at the level of non-resonant terms.

Technically, we proceed as follows to obtain the virtual corrections in DPA for the W-boson resonances in $q\bar{q}/\mathrm{gg} \to \nu_\mathrm{e}\mathrm{e}^+\mu^-\bar{\nu}_\mu\mathrm{b}\bar{\mathrm{b}}$. We select those diagrams that involve two resonant W bosons and perform a projection of the final-state momenta that puts W bosons onto their mass shells. Since we deal with corrections of $\mathcal{O}(\alpha_\mathrm{s})$ in DPA only, the intrinsic ambiguity leads to differences of the order of $\alpha_\mathrm{s}\Gamma_\mathrm{W}/(\pi M_\mathrm{W})$ for different versions of the projection, provided that the projection does not induce large changes in the matrix elements. To this end, we must keep the invariant masses of the top and antitop quarks fixed. In fact, we do not modify the four-momenta of the top and antitop and define the on-shell projected momenta $\hat{p}_i$ in terms of the original momenta p_i as follows:

$$\begin{aligned}
\hat{p}_\mathrm{b} &= p_\mathrm{b}\frac{p_\mathrm{t}^2 - M_\mathrm{W}^2}{2p_\mathrm{t}p_\mathrm{b}}, \qquad & \hat{p}_{\mathrm{W}^+} &= p_\mathrm{t} - \hat{p}_\mathrm{b},\\
\hat{p}_{\mathrm{e}^+} &= p_{\mathrm{e}^+}\frac{M_\mathrm{W}^2}{2\hat{p}_{\mathrm{W}^+}p_{\mathrm{e}^+}}, \qquad & \hat{p}_{\nu_\mathrm{e}} &= \hat{p}_{\mathrm{W}^+} - \hat{p}_{\mathrm{e}^+},\\
\hat{p}_{\bar{\mathrm{b}}} &= p_{\bar{\mathrm{b}}}\frac{p_{\bar{\mathrm{t}}}^2 - M_\mathrm{W}^2}{2p_{\bar{\mathrm{t}}}p_{\bar{\mathrm{b}}}}, \qquad & \hat{p}_{\mathrm{W}^-} &= p_{\bar{\mathrm{t}}} - \hat{p}_{\bar{\mathrm{b}}},\\
\hat{p}_{\mu^-} &= p_{\mu^-}\frac{M_\mathrm{W}^2}{2\hat{p}_{\mathrm{W}^-}p_{\mu^-}}, \qquad & \hat{p}_{\bar{\nu}_\mu} &= \hat{p}_{\mathrm{W}^-} - \hat{p}_{\mu^-}.
\end{aligned} \tag{2.50}$$

Each top decay is treated separately, the momenta of the bottom quarks and leptons are rescaled such that $\hat{p}^2_{\mathrm{W}^\pm} = M^2_\mathrm{W}$ and $\hat{p}^2_{\nu_\mathrm{e}} = 0 = \hat{p}^2_{\bar{\nu}_\mu}$, and the momenta of the neutrinos and W bosons are determined from four-momentum conservation. The above-mentioned ambiguity in the on-shell projection, e.g., manifests itself in our choice to rescale the charged-lepton momenta and to fix the neutrino momenta via momentum conservation; the analogous on-shell projection with the roles of charged leptons and neutrinos interchanged would be equally good. Apart from the W propagators, the matrix elements are computed using on-shell projected momenta, physical (i.e. real) W- and Z-boson masses, and $\Gamma_\mathrm{W} = \Gamma_\mathrm{Z} = 0$. The phase space and the W propagators are evaluated using the original off-shell momenta and including the W-boson width.

This procedure accounts for the most important off-shell effects in spite of the use of the DPA for the one-loop matrix element. This fact is strongly supported by the results on W-pair production in $\mathrm{e}^+\mathrm{e}^-$ annihilation, where comparisons between DPA and full off-shell calculations exist for LO [87] and NLO electroweak corrections [50, 51].

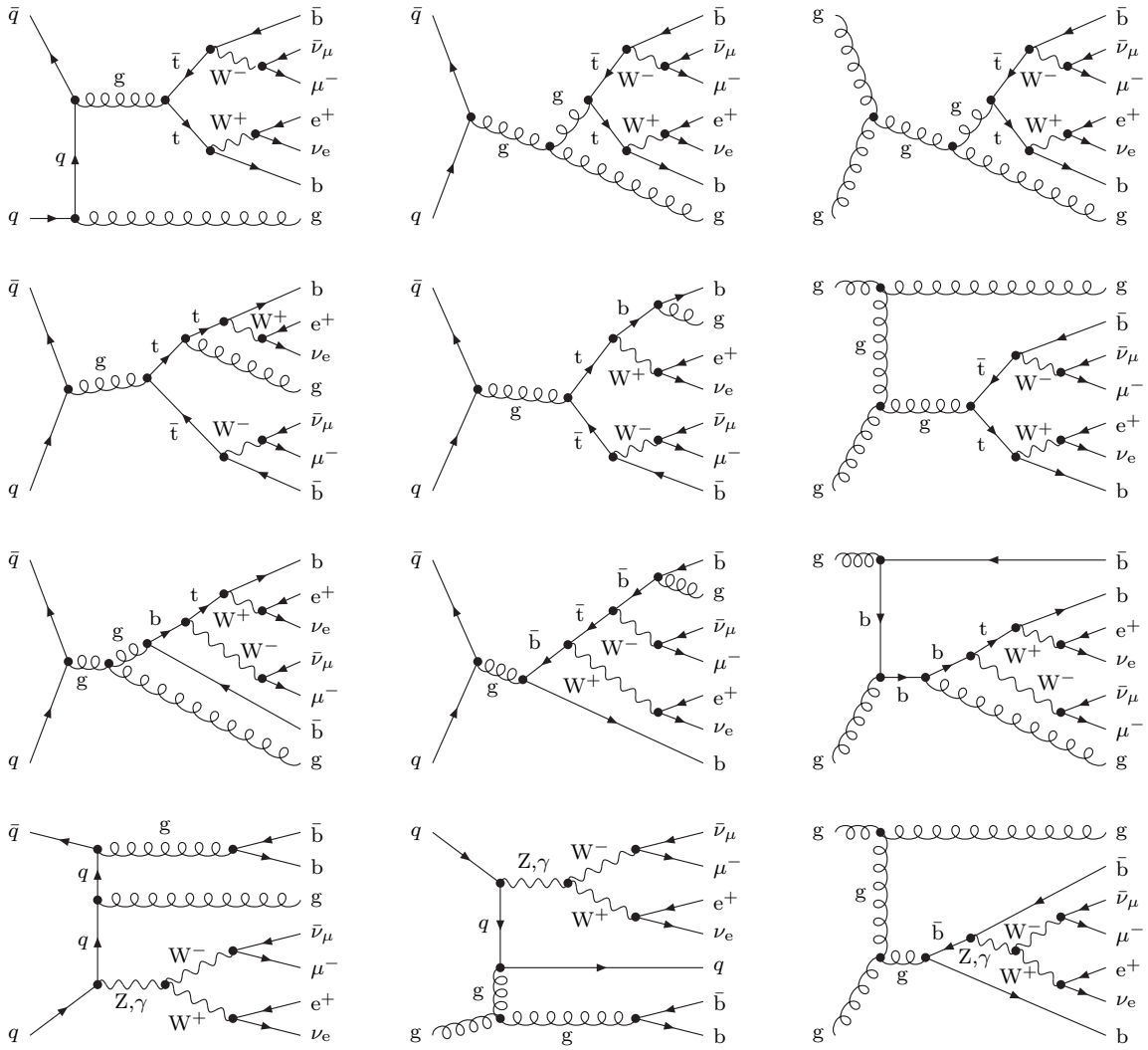

Figure 4: Examples of real-emission diagrams with two (first two lines), one (third line) or no (last line) top-quark resonances. All depicted diagrams involve two W-boson resonances.

2.3 Real corrections

2.3.1 Matrix-element evaluation

The real corrections receive contributions from the $2 \to 7$ partonic processes $gg \to \nu_e e^+ \mu^- \bar{\nu}_\mu b\bar{b}g$, $q\bar{q} \to \nu_e e^+ \mu^- \bar{\nu}_\mu b\bar{b}g$, $gq \to \nu_e e^+ \mu^- \bar{\nu}_\mu b\bar{b}q$, and $g\bar{q} \to \nu_e e^+ \mu^- \bar{\nu}_\mu b\bar{b}\bar{q}$. In the NwWA the gg channel involves 208 tree diagrams, while the $q\bar{q}$, gq, and $g\bar{q}$ channels, which are related by crossing symmetry, are described by 90 tree diagrams each. Examples of doubly-W-resonant real-emission diagrams are depicted in Figure 4. When including FwW effects, additional singly-W-resonant diagrams must be taken into account (for examples see Figure 5) resulting in a total number of 508 and 234 diagrams for the gg channel and the $q\bar{q}$ channel, respectively. The $2 \to 7$ matrix elements are evaluated

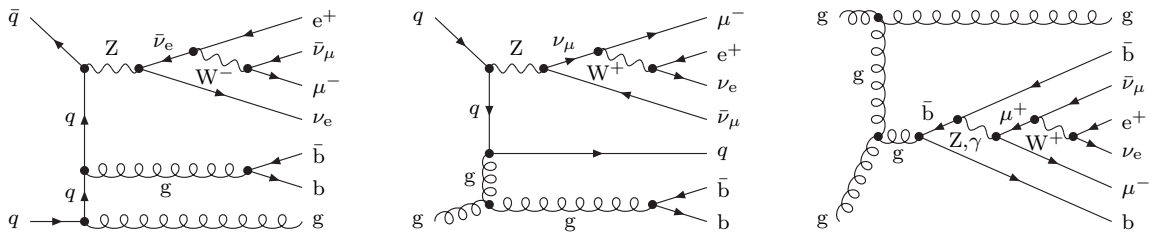

Figure 5: Examples of real-emission diagrams that involve a single W-boson resonance and contribute to the FwW corrections.

with MADGRAPH [88] and, alternatively, using the Weyl–van-der-Waerden formalism of Ref. [74]. In addition, in presence of FwW effects we used OPENLOOPS [89] to evaluate the real-emission matrix elements in the complex-mass scheme. All real bremsstrahlung amplitudes have been checked by comparing different calculations for several phase-space points.

2.3.2 Treatment of IR singularities

Owing to IR singularities all the NLO pieces in (2.2) are singular, but their sum is finite. When combining virtual and real corrections, soft singularities as well as singularities connected to collinear configurations in the final state cancel for "infrared-safe" observables after applying a jet algorithm. The remaining singularities connected to the collinear initial-state splittings factorize and are removed via $\overline{\text{MS}}$ PDF redefinitions, i.e. they are compensated by the term $\mathrm{d}\hat{\sigma}_{\text{fact},ab}$ in (2.2).

To isolate the IR divergences and cancel them analytically, we employ the subtraction formalism. To this end, we rewrite (2.2) as

$$\begin{aligned}\int \mathrm{d}\hat{\sigma}_{ab} &= \int_6 \mathrm{d}\hat{\sigma}_{0,ab} + \int_6 \left[\mathrm{d}\hat{\sigma}_{\text{virt},ab} - \mathrm{d}\hat{\sigma}^{\text{sub}}_{\text{virt},ab}\right] + \int_7 \left[\mathrm{d}\hat{\sigma}_{\text{real},ab} - \mathrm{d}\hat{\sigma}^{\text{sub}}_{\text{real},ab}\right] \\ &\quad + \int_0^1 \mathrm{d}x \int_6 \left[\mathrm{d}\hat{\sigma}_{\text{fact},ab} - \mathrm{d}\hat{\sigma}^{\text{sub}}_{\text{fact},ab}\right] \\ &= \int_6 \mathrm{d}\hat{\sigma}_{0,ab} + \int_6 \mathrm{d}\hat{\sigma}^{\text{fin}}_{\text{virt},ab} + \int_7 \mathrm{d}\hat{\sigma}^{\text{fin}}_{\text{real},ab} + \int_0^1 \mathrm{d}x \int_6 \mathrm{d}\hat{\sigma}^{\text{fin}}_{\text{fact},ab}\,. \end{aligned} \tag{2.51}$$

Here the added subtraction terms $\mathrm{d}\hat{\sigma}^{\text{sub}}_{\text{virt},ab}$, $\mathrm{d}\hat{\sigma}^{\text{sub}}_{\text{real},ab}$, and $\mathrm{d}\hat{\sigma}^{\text{sub}}_{\text{fact},ab}$ are constructed in such a way that their sum vanishes exactly and that they individually cancel all IR singularities of the corresponding original terms locally in phase space. As discussed in Section 2.3, when including FwW effects, the DPA is applied to the subtracted virtual corrections, i.e. the second term on the r.h.s. of (2.51), otherwise there would be a mismatch in the IR structure between virtual corrections and corresponding subtraction terms (see Ref. [86] for the same reasoning concerning photon radiation).

For the subtraction terms, we choose in-house implementations of the dipole subtraction formalism [56–59] for NLO QCD calculations. Specifically this is done in dimensional regularization with strictly massless light quarks (including b quarks) and, alternatively,

in a hybrid scheme with small quark masses and massless gluons with the respective dipole subtraction terms from Ref. [59]; the typical agreement between the results from the two alternative treatments is at the level of 12 digits.

Soft and collinear singularities in the "endpoint part" (the I operator of Refs. [56, 59]) of the subtraction function, $\mathrm{d}\hat{\sigma}^{\mathrm{sub}}_{\mathrm{virt},ab}$, are regularized using the same regularization prescription (dimensional or with small quark masses) as the corresponding virtual corrections. No regularization is needed in the subtraction terms for the real corrections, $\mathrm{d}\hat{\sigma}^{\mathrm{sub}}_{\mathrm{real},ab}$. For both the $q\bar{q}$ and gg channels 12 different dipole subtraction terms need to be included while each $\mathrm{g}^{(-)}q$channel requires only 6, since we demand b quarks with finite transverse momentum in the final state.

Version 1 of the real corrections employs a fully automatized implementation of dipole subtraction terms, which has been developed and tested during the calculation of VV+jet production [34, 90, 91]. The underlying matrix elements are based on helicity amplitudes employing the Weyl–van-der-Waerden formalism of Ref. [74], which facilitates the treatment of helicity correlations. The colour structure of the dipole terms is generated automatically from the inserted colour operators and the underlying Born amplitudes.

In *version 2* all dipole subtraction terms have been implemented by hand into the Monte Carlo generator. Colour and helicity correlations that enter the subtraction procedure are generated by means of AutoDipole [92] in NwWA and OpenLoops [89] for the FwW case.

The cancellation between real matrix elements and dipole subtraction terms has been verified numerically in all soft and collinear regions. The individual dipole subtraction terms, the subtracted real matrix elements, and the integrated subtraction terms (P and K terms of Refs. [56, 59]) have been compared point-wise between the two independent calculations. The agreement was generally at the level of 13−14 digits.

2.3.3 Phase-space integration and numerical performance

To achieve sufficient numerical stability, we perform the 17-dimensional phase-space integration using multi-channel Monte Carlo techniques [60] with adaptive weight optimization [93]. For each of the bremsstrahlung Feynman diagrams a corresponding channel is taken into account in the Monte Carlo integration. In addition, the integration of the dipole-subtracted $2 \to 7$ contributions is optimized by means of extra channels corresponding to the dipole kinematics. For each of the 12 different dipoles and each tree-level diagram a new channel is introduced resulting in $12 \times 31 = 372$ and $12 \times 14 = 168$ extra channels in the NwWA in the gg and $q\bar{q}$ channels, respectively. When including FwW effects the number of additional channels grows to $12 \times 79 = 948$ and $12 \times 38 = 456$, respectively. In the $\mathrm{g}^{(-)}q$channel dipoles based on both gg and $q\bar{q}$ Born subprocess are needed. So $3 \times 31 + 3 \times 14 = 135$ and $3 \times 79 + 3 \times 38 = 351$ channels are added here in the NwWA and with FwW effects, respectively. These additional channels lead to some improvement in the convergence of the Monte Carlo integration.

In *version 1*, the phase-space integration, implemented in C++, is based on RacoonWW [61], but the phase-space mappings are built up in a more generic way very similar to the approach of Lusifer [62].

The Monte Carlo generator of *version 2* is a further development of the one used in COFFER$\gamma\gamma$ [94] and for the calculation of the NLO corrections to $pp \to Hjj + X$ [95] and $pp \to t\bar{t}b\bar{b} + X$ [72].

For the complete NLO cross section we found agreement between the two versions of our code at the few-per-mille level. We also performed a detailed comparison of all differential distributions presented in this paper and found good agreement.

For a typical run we generate 10^8 phase-space points, and the fraction of points within cuts is roughly 50%. This yields an accuracy for the NLO cross section of about 0.2–0.3%. For the LHC, the contributions of the $g\bar{u}$, $g\bar{d}$, $u\bar{u}$, and $d\bar{d}$ channels were calculated for every 2nd, 5th, 4th, and 5th event, respectively. The virtual corrections for the gg, $u\bar{u}$, and $d\bar{d}$ channels were evaluated for every 100th, 200th, and 500th event, respectively. The resulting runtime on a 3 GHz Intel Xeon processor using the `ifort` compiler is about 170 h. The bulk of the runtime is taken by the real corrections to the gg channel. For the virtual corrections the CPU time is dominated by the gg channel and amounts to 180 ms per event. For the Tevatron, the weights of the different contributions are different, the runtime is somewhat smaller for a comparable accuracy. For the numerical results shown in the following almost 10^9 events were generated.

3 Numerical results

In the following we present predictions for various observables that are relevant for top-pair production, either as signal or as background to Higgs production or new physics. Neither the following setup nor the considered observables are deliberately chosen to enhance the calculated off-shell and finite-top-width effects. Our aim rather is to quantify these effects for the standard observables.

3.1 Input parameters

We study the process $h_1h_2 \to \nu_e e^+\mu^-\bar{\nu}_\mu b\bar{b} + X$ at Tevatron ($p\bar{p}$ collisions) with $\sqrt{s} = 1.96\,\text{TeV}$ and at the LHC (pp collisions) for the collider energies 7 TeV, 8 TeV, and 14 TeV. The input parameters and the default setup are basically the same as in Ref. [32], where first results of our calculation have been presented. For completeness we specify the input and discuss modifications.

In NLO (LO) QCD we employ the MSTW2008NLO (LO) parton distributions [96] and use the running of the strong coupling constant α_s with two-loop (one-loop) accuracy as provided by the LHApdf library. In the renormalization of the strong coupling constant the top-quark loop in the gluon self-energy is subtracted at zero momentum, and the number of active flavours is $N_F = 5$. In this scheme, the running of α_s is generated solely by the contributions of the light-quark and gluon loops. Contributions induced by the strongly suppressed bottom-quark parton density are neglected. For the gauge-boson and top-quark masses we use

$$m_t = 172.0\,\text{GeV}, \quad M_W = 80.399\,\text{GeV}, \quad M_Z = 91.1876\,\text{GeV}. \tag{3.1}$$

The masses of all other quarks, including b quarks, are neglected. In view of the negligibly small Higgs-mass dependence we adopt the $M_H \to \infty$ limit, i.e. we neglect closed fermion

loops involving top quarks coupled to Higgs bosons. The electroweak coupling is derived from the Fermi constant in the G_μ-scheme,

$$G_\mu = 1.16637 \times 10^{-5}\,\text{GeV}^{-2}, \quad \alpha = \frac{\sqrt{2}}{\pi} G_\mu M_\text{W}^2 \left(1 - \frac{M_\text{W}^2}{M_\text{Z}^2}\right). \tag{3.2}$$

While in narrow-W-width approximation (NwWA) we employ the usual real-valued weak mixing angle, $s_\text{w}^2 = 1 - M_\text{W}^2/M_\text{Z}^2$, when including finite-W-width (FwW) effects we employ the complex-valued mixing angle (2.28). To derive the electromagnetic coupling (3.2), we always use the real W- and Z-boson masses.

The leptonic decays of W bosons are treated in two different ways: in the (spin-correlated) NwWA and including FwW effects. In the latter case, as discussed in Section 2.1.3, FwW contributions have to be included both in the matrix elements and in the top-quark width used as input parameter. The top-quark width for unstable W bosons in NLO QCD was given in Ref. [97]. Neglecting the bottom-quark mass, as we do throughout this paper, the LO top-quark width reads

$$\Gamma_\text{t}^\text{LO} = \frac{G_\mu m_\text{t}^5}{16\sqrt{2}\pi^2 M_\text{W}^2} \int_0^1 \frac{\text{d}y\,\gamma_\text{W}}{(1 - y/\bar{y})^2 + \gamma_\text{W}^2} F_0(y) \tag{3.3}$$

with $\gamma_\text{W} = \Gamma_\text{W}/M_\text{W}$, $\bar{y} = (M_\text{W}/m_\text{t})^2$, and

$$F_0(y) = 2(1-y)^2(1+2y). \tag{3.4}$$

Including NLO QCD corrections, the top-quark width is given by

$$\Gamma_\text{t}^\text{NLO} = \frac{G_\mu m_\text{t}^5}{16\sqrt{2}\pi^2 M_\text{W}^2} \int_0^1 \frac{\text{d}y\,\gamma_\text{W}}{(1 - y/\bar{y})^2 + \gamma_\text{W}^2} \left[F_0(y) - \frac{2\alpha_\text{s}}{3\pi} F_1(y)\right] \tag{3.5}$$

with

$$\begin{aligned} F_1(y) = {} & 2(1-y)^2(1+2y)\left[\pi^2 + 2\,\text{Li}_2(y) - 2\,\text{Li}_2(1-y)\right] \\ & + 4y(1-y-2y^2)\ln(y) + 2(1-y)^2(5+4y)\ln(1-y) \\ & - (1-y)(5+9y-6y^2). \end{aligned} \tag{3.6}$$

In NwWA, i.e. for $\gamma_\text{W} \to 0$, the top width follows from (3.3)–(3.6) by the replacement

$$\frac{\gamma_\text{W}}{(1 - y/\bar{y})^2 + \gamma_\text{W}^2} \to \pi\bar{y}\,\delta(y - \bar{y}). \tag{3.7}$$

With the above formulas and our input parameter set we obtain

$$\Gamma_\text{t}^\text{LO} = 1.4655\,\text{GeV}, \qquad \Gamma_\text{t}^\text{NLO} = 1.3376\,\text{GeV} \tag{3.8}$$

in the NwWA and

$$\Gamma_\text{t}^\text{LO} = 1.4426\,\text{GeV}, \qquad \Gamma_\text{t}^\text{NLO} = 1.3167\,\text{GeV} \tag{3.9}$$

including FwW corrections. Since the leptonic W-boson decays do not receive NLO QCD corrections and $\nu_\text{e}\text{e}^+\mu^-\bar{\nu}_\mu\text{b}\bar{\text{b}}$ production does not involve $\text{Z} \to f\bar{f}$ subprocesses, for the gauge-boson widths we use the NLO QCD values[8]

$$\Gamma_\text{W} = 2.09974\,\text{GeV}, \qquad \Gamma_\text{Z} = 2.50966\,\text{GeV} \tag{3.10}$$

everywhere, i.e. for LO as well as for NLO matrix elements.

[8]Using the measured Z-boson width instead has no significant effect on our results.

3.2 Jet definition, cuts, and scale choice

We now turn to the event selection. Final-state quarks and gluons with pseudo-rapidity $|\eta| < 5$ are converted into infrared-safe jets using the anti-$k_{\rm T}$ algorithm [98]. The jet-resolution parameter R is set to $R = 0.4$ and $R = 0.5$ for the Tevatron and the LHC, respectively. After recombination, we impose cuts on the transverse momenta and pseudo-rapidities of the leptons and b jets, and on the missing transverse momentum. For Tevatron we choose

$$\begin{aligned} p_{\rm T,b} &> 20\,{\rm GeV}, \qquad |\eta_{\rm b}| < 2.5, \qquad p_{\rm T,miss} > 25\,{\rm GeV}, \\ p_{{\rm T},l} &> 20\,{\rm GeV}, \qquad |\eta_l| < 2.5, \end{aligned} \tag{3.11}$$

and for the LHC

$$\begin{aligned} p_{\rm T,b} &> 30\,{\rm GeV}, \qquad |\eta_{\rm b}| < 2.5, \qquad p_{\rm T,miss} > 20\,{\rm GeV}, \\ p_{{\rm T},l} &> 20\,{\rm GeV}, \qquad |\eta_l| < 2.5, \end{aligned} \tag{3.12}$$

where $p_{\rm T,miss}$ is obtained from the vector sum of all visible transverse momenta after jet recombination.

For the factorization ($\mu_{\rm F}$) and renormalization ($\mu_{\rm R}$) scales we have considered different choices. A common approach, which was adopted in Refs. [32, 33], is to set $\mu_{\rm R} = \mu_{\rm F} = m_{\rm t}$. However, as shown in Section 3.5, this choice leads to perturbative instabilities in the high-energy tails of differential distributions. The use of a dynamical scale, which adapts to the hard scattering energy, guarantees a much better convergence of the perturbative expansion. We thus consider an alternative scale choice, based on the kinematic variable

$$E_{\rm T} = \sqrt{\sqrt{m_{\rm t}^2 + p_{\rm T,t}^2}\sqrt{m_{\rm t}^2 + p_{\rm T,\bar{t}}^2}}, \tag{3.13}$$

which corresponds to the geometric average of the top- and antitop-quark transverse energies. Similar scales had already been used in early papers [1, 2, 4]. The top transverse energy $E_{\rm T}$ coincides with $m_{\rm t}$ for vanishing transverse momenta and adapts to the higher scattering energy at large transverse momenta. While we use the scales $\mu_{\rm fix} = m_{\rm t}$ or $\mu_{\rm dyn} = E_{\rm T}$ to describe $\nu_{\rm e}{\rm e}^+\mu^-\bar{\nu}_\mu{\rm b}\bar{\rm b}$ production at Tevatron, for the LHC we use half of these scales, i.e. $\mu_{\rm fix} = m_{\rm t}/2$ or $\mu_{\rm dyn} = E_{\rm T}/2$. The different scale choice is motivated by the fact that $\rm t\bar{t}$ production at the Tevatron is dominated by s-channel quark–antiquark annihilation, while the dominant $\rm t\bar{t}$ production mechanism at the LHC is t-channel gluon fusion, which prefers smaller scales. Moreover, in Ref. [99] it has been demonstrated that the contributions beyond NLO in an NLL soft-gluon resummation are smaller for $\mu = m_{\rm t}/2$ than for $\mu = m_{\rm t}$. Our different scale choices are summarized in Table 1. There we also show the logarithmic average $\bar{\mu}_{\rm dyn}$ of the dynamical scale, defined via

$$\ln \bar{\mu}_{\rm dyn} = \frac{\int \ln(\mu_{\rm dyn}) {\rm d}\sigma}{\int {\rm d}\sigma}. \tag{3.14}$$

The numerical values of $\bar{\mu}_{\rm dyn}$ indicate that, for what concerns the integrated cross section, using the dynamical scale corresponds to an effective increase of the fixed scale by roughly 18−27%, depending on the collider energy.

collider	μ_{fix}	μ_{dyn}	$\sqrt{s}\,[\text{TeV}]$	$\bar{\mu}_{\text{dyn}}\,[\text{GeV}]$
Tevatron	m_{t}	E_{T}	1.96	203.1
LHC	$m_{\text{t}}/2$	$E_{\text{T}}/2$	7	105.8
			8	106.5
			14	109.2

Table 1: Fixed (μ_{fix}) and dynamical (μ_{dyn}) scales used for Tevatron and LHC predictions. The last column shows the logarithmic average of the dynamical scale, as defined in (3.14).

The scale uncertainty of our LO and NLO predictions is determined by uniform variations of the renormalization and factorization scales,

$$\mu_{\text{F}} = \mu_{\text{R}} = \mu, \tag{3.15}$$

around the central values

$$\mu_0 = \mu_{\text{fix}} \qquad \text{or} \qquad \mu_0 = \mu_{\text{dyn}}. \tag{3.16}$$

When varying the renormalization scale in PDFs and matrix elements, we keep it fixed in the top-quark width, which is always evaluated at the scale m_{t}. The mismatch between the scales used in partial and total top-decay widths is compensated by the partial-width correction (2.27), which we include in NLO$^+$ predictions as discussed in Section 2.1.2. In Section 3.3, to investigate the scale dependence of the LO and NLO integrated cross section we vary μ up and down by a factor eight. For all other results we provide LO and NLO predictions with uncertainties corresponding to factor-two scale variations. More precisely, the observables are evaluated at three different scales, $\mu/\mu_0 = 0.5, 1, 2$; the central value is obtained for $\mu = \mu_0$, and the error band is determined by the envelope of the three scales.

3.3 Total cross section and scale dependence

We first present Tevatron and LHC total cross sections with fixed and dynamical scales (see Table 1), both in NwWA and including FwW effects. The results, listed in Table 2, correspond to the standard cuts defined in (3.11) and (3.12). Besides the LO and NLO $\nu_{\text{e}}\text{e}^+\mu^-\bar{\nu}_\mu\text{b}\bar{\text{b}}$ cross sections, we also present improved results that include the NLO$^+$ matching corrections of Section 2.1.2 and can be regarded as our best predictions. These $\sigma^{\text{NLO}^+}_{\nu_{\text{e}}\text{e}^+\mu^-\bar{\nu}_\mu\text{b}\bar{\text{b}}}$ results incorporate higher-order effects determined by the relation (2.25) between the narrow-top-limit of the inclusive $\nu_{\text{e}}\text{e}^+\mu^-\bar{\nu}_\mu\text{b}\bar{\text{b}}$ cross section and the on-shell $\text{t}\bar{\text{t}}$ cross section, as well as the "partial-with correction" (2.27).

At the Tevatron, the K factor is 0.95 for the fixed scale and 1.03 for the dynamical scale. Similarly, for the LHC we find K factors slightly below one for the fixed scale and 5−12% above one for the dynamical scale. If we had not reduced the central scale by a factor 2, the K factors at the LHC would be around 1.27−1.38. The use of the dynamical scale increases the K factor by about 10% and changes the NLO predictions by less than 1%. The inclusion of the NLO corrections reduces the scale dependence from 36−45% to

$\sqrt{s}$ [TeV]	μ_0	Γ_W	σ_{LO} [fb]	K	σ_{NLO} [fb]	$\frac{\sigma_{NLO^+}}{\sigma_{NLO}}$	σ_{NLO^+} [fb]
1.96	m_t	FwW	$44.197(2)^{+44.4\%}_{-28.2\%}$	0.95	$41.77(2)^{-8.8\%}_{-5.2\%}$	0.98	$40.93(2)^{+2.3\%}_{-10.2\%}$
1.96	m_t	NwWA	$44.304(2)^{+44.4\%}_{-28.2\%}$	0.94	$41.78(2)^{-9.1\%}_{-5.1\%}$	0.98	$40.96(2)^{+2.1\%}_{-10.0\%}$
1.96	E_T	FwW	$40.480(2)^{+42.8\%}_{-27.5\%}$	1.03	$41.77(2)^{-3.3\%}_{-7.1\%}$	0.96	$40.23(2)^{+5.7\%}_{-11.3\%}$
1.96	E_T	NwWA	$40.580(2)^{+42.8\%}_{-27.5\%}$	1.03	$41.79(3)^{-3.6\%}_{-7.0\%}$	0.96	$40.27(3)^{+5.4\%}_{-11.2\%}$
7	$m_t/2$	FwW	$922.22(3)^{+44.9\%}_{-28.5\%}$	0.93	$862.1(8)^{-13.1\%}_{-2.9\%}$	1.01	$870.4(8)^{-0.2\%}_{-8.7\%}$
7	$m_t/2$	NwWA	$925.77(3)^{+44.8\%}_{-28.5\%}$	0.93	$864.1(8)^{-13.4\%}_{-2.8\%}$	1.01	$872.7(8)^{-0.4\%}_{-8.6\%}$
7	$E_T/2$	FwW	$824.00(3)^{+42.8\%}_{-27.6\%}$	1.05	$866.9(6)^{-5.5\%}_{-5.7\%}$	0.99	$854.0(7)^{+4.2\%}_{-10.4\%}$
7	$E_T/2$	NwWA	$827.22(3)^{+42.8\%}_{-27.6\%}$	1.05	$867.0(8)^{-5.9\%}_{-5.5\%}$	0.99	$854.7(8)^{+3.9\%}_{-10.3\%}$
8	$m_t/2$	FwW	$1278.20(4)^{+43.1\%}_{-27.8\%}$	0.95	$1219(1)^{-10.9\%}_{-3.2\%}$	1.01	$1226(1)^{+0.9\%}_{-8.8\%}$
8	$m_t/2$	NwWA	$1283.06(5)^{+43.1\%}_{-27.8\%}$	0.95	$1221(1)^{-11.2\%}_{-3.1\%}$	1.01	$1229(1)^{+0.7\%}_{-8.7\%}$
8	$E_T/2$	FwW	$1141.69(4)^{+41.1\%}_{-26.9\%}$	1.07	$1221(1)^{-4.1\%}_{-5.8\%}$	0.98	$1200(1)^{+5.0\%}_{-10.3\%}$
8	$E_T/2$	NwWA	$1146.17(4)^{+41.1\%}_{-26.9\%}$	1.07	$1225(1)^{-4.3\%}_{-5.7\%}$	0.98	$1203(1)^{+4.8\%}_{-10.3\%}$
14	$m_t/2$	FwW	$4416.8(2)^{+36.3\%}_{-24.8\%}$	1.01	$4468(4)^{-3.1\%}_{-4.4\%}$	0.99	$4439(4)^{+5.2\%}_{-9.0\%}$
14	$m_t/2$	NwWA	$4433.3(2)^{+36.3\%}_{-24.8\%}$	1.01	$4473(4)^{-3.3\%}_{-4.3\%}$	0.99	$4445(5)^{+5.0\%}_{-8.9\%}$
14	$E_T/2$	FwW	$3953.1(2)^{+34.6\%}_{-24.0\%}$	1.12	$4420(4)^{+0.8\%}_{-6.1\%}$	0.97	$4301(4)^{+7.6\%}_{-10.\%}$
14	$E_T/2$	NwWA	$3968.1(2)^{+34.6\%}_{-24.0\%}$	1.12	$4430(4)^{+0.7\%}_{-6.0\%}$	0.97	$4311(4)^{+7.5\%}_{-9.9\%}$

Table 2: Total cross section for $pp/p\bar{p} \to \nu_e e^+ \mu^- \bar{\nu}_\mu b\bar{b} + X$ within cuts for Tevatron and LHC at different CM energies in the NwWA and including FwW effects both with fixed and dynamical scales. In the cross-section numbers the upper variation corresponds to the scale $\mu = 0.5\mu_0$, the lower to $\mu = 2\mu_0$.

4−13% at the LHC and from 44% to 9% at the Tevatron. In most cases, the NLO cross section goes down irrespectively of the direction of the scale variation. This indicates the presence of a maximum of $\sigma_{NLO}(\mu)$ in the vicinity of the central scale μ_0 (see Figures 6–7). The residual scale dependence is comparable for fixed and dynamical scales. Including the partial-width correction (2.27) in the fixed-order NLO predictions would result in a shift of roughly +2% in the central values of the LHC cross sections (due to the reduced central scale), while the upper ($\mu = 0.5\mu_0$) and lower ($\mu = 2\mu_0$) NLO scale variations at Tevatron and the LHC would move by +2% and −2%, respectively.

The FwW effects amount to −0.3% at the Tevatron and −0.4% at the LHC rather independent of the collider energy and the scale choice. These per-mille-level FwW effects confirm the strong suppression anticipated in Section 2.1.3. If we did not use the top width calculated with FwW effects, the inconsistency of the branching fraction (2.10) would lead to a fake FwW effect of roughly −3%. The NLO$^+$ correction, which matches our NLO results to the on-shell $t\bar{t}$ cross section and includes the partial-width correction (2.27), ranges from −4% to +1%, depending on the scale choice and the collider energy. The scale dependence of σ_{NLO^+} is at the level of 10%.

Figures 6 and 7 display the dependence of the LO and NLO cross sections under uniform variations of the fixed and dynamical QCD scales at Tevatron and the LHC with $\sqrt{s} = 7\,\text{TeV}$, 8 TeV, and 14 TeV. The fact that the central scale μ_0 is shifted to the left in the LHC plots reflects the collider-dependent scale choice (see Table 1). For Tevatron, the maximum of the NLO cross section is obtained for $\mu \simeq \mu_0 = m_\text{t}$ or E_T, and the K factor is close to one in this region. For the LHC, the maximum of the NLO cross section is shifted to smaller values near $\mu \simeq \mu_0 = m_\text{t}/2$ or $E_\text{T}/2$, and also the K factor reaches a minimum there. These features are quite independent of the LHC energy and can be attributed to the different dominant production channels at Tevatron and the LHC. The improved stability of the cross section against NLO corrections and scale variations supports the use of the "reduced scales" $\mu_\text{fix} = m_\text{t}/2$ and $\mu_\text{dyn} = E_\text{T}/2$ at the LHC.

3.4 Asymmetries

Asymmetries in top–antitop production have found particular interest recently, triggered by experimental results from Tevatron [100–102]. The situation is different for $\text{p}\bar{\text{p}}$ collisions at Tevatron and pp collisions at the LHC. In this section we discuss FwW effects and compare asymmetries obtained with fixed and dynamical scale choices. Results based on dynamical scales and including FwW effects should be regarded as our "best" NLO QCD predictions. For a recent review, including a discussion of electroweak correction effects [10, 103], we refer to Ref. [104].

3.4.1 Asymmetries for Tevatron

At LO, on-shell top–antitop production is totally symmetric under the exchange $\text{t} \leftrightarrow \bar{\text{t}}$ both for $q\bar{q}$ and gg production mechanisms. For the gg channel this is a consequence of C invariance of QCD, for $q\bar{q}$ the symmetry is accidental. Consequently, the LO angular distributions of the top and antitop quarks are forward–backward symmetric for $\text{p}\bar{\text{p}}$ collisions. This accidental symmetry is violated by NLO corrections, in particular by interference terms in $q\bar{q} \to \text{t}\bar{\text{t}}\text{g}$ and $\text{g}q \to \text{t}\bar{\text{t}}q$ radiative processes [105] and by interference terms in the $q\bar{q}$ channel between virtual corrections and the leading order [106]. Since top–antitop production at Tevatron is dominated by the $q\bar{q}$ channel, an observable forward–backward asymmetry emerges. In the laboratory frame this can be defined as

$$A_\text{t,LAB}^\text{FB} = \frac{\sigma(y_\text{t} > 0) - \sigma(y_\text{t} < 0)}{\sigma(y_\text{t} > 0) + \sigma(y_\text{t} < 0)}, \tag{3.17}$$

where y_t and $y_{\bar{\text{t}}}$ are the rapidities of the top and antitop quark, respectively. In our predictions we set $\sigma = \sigma_\text{NLO}$ both in numerator and denominator. Owing to CP symmetry, the asymmetry of the antitop is oppositely equal to the asymmetry of the top quark. Our numerical results for the asymmetry (3.17) are given in the second column of the upper part of Table 3 including FwW effects. Compared to the result for the fixed scale $\mu_0 = m_\text{t}$, the asymmetry is lowered by 10−15% for the dynamical scale $\mu_0 = E_\text{T}$. The scale uncertainty is large, since the numerator is effectively known only in leading order and has a scale dependence like α_s^3, while the NLO cross section in the denominator is rather stable against scale variations. Within the integration accuracy, the results for on-shell and off-shell W bosons coincide.

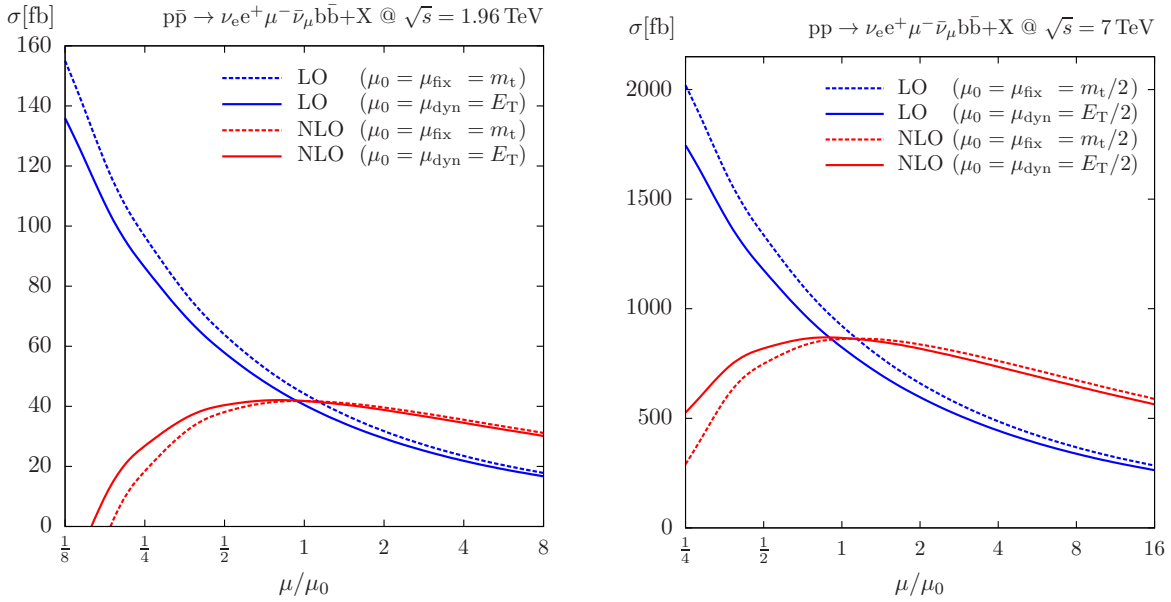

Figure 6: Scale dependence of the LO and NLO cross sections at Tevatron (left) and the LHC with $\sqrt{s} = 7\,\text{TeV}$ (right). The renormalization and factorization scales are varied around the fixed ($\mu_0 = \mu_{\text{fix}}$) or dynamical ($\mu_0 = \mu_{\text{dyn}}$) central values defined in Table 1.

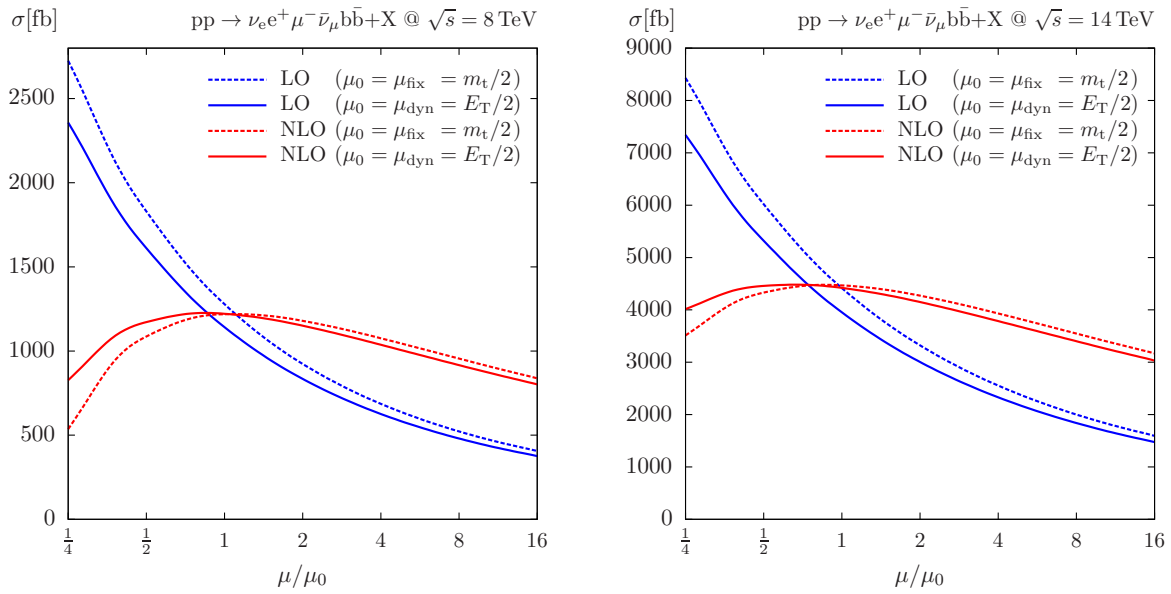

Figure 7: Scale dependence of the LO and NLO cross sections at the LHC with $\sqrt{s} = 8\,\text{TeV}$ (left) and 14 TeV (right). The renormalization and factorization scales are varied around the fixed or dynamical central values μ_0 defined in Table 1.

In the literature, the asymmetry $A_{\mathrm{t,LAB}}^{\mathrm{FB}}$ has often been calculated by using the LO cross section in the denominator [10, 30, 103, 106]. This reduces the scale dependence by at least a factor of 4, while using NLO predictions in the numerator and the denominator of (3.17), as in the present paper, provides a more conservative estimate of theoretical uncertainties. In any case, this choice does not really affect the size of the finite-width effects that we are after. We do not include QED or electroweak corrections.

We note that for off-shell top quarks an asymmetry already exists in LO, e.g. from non-resonant diagrams where W bosons are emitted from initial-state quarks. This asymmetry is, however, only at the level of 10^{-4} and thus negligible.

An analogous asymmetry can be defined for the charged leptons. Results for the positron including FwW effects are given in the third column of the upper part of Table 3, both for fixed and dynamical scales. Our results at the fixed scale $\mu_0 = m_{\mathrm{t}}$ for both $A_{\mathrm{t,LAB}}^{\mathrm{FB}}$ and $A_{\mathrm{e^+,LAB}}^{\mathrm{FB}}$ agree well with the corresponding numbers given in Refs. [30, 33, 107].

Alternatively, asymmetries can be defined in the CM frame of the $\mathrm{t\bar{t}}$ system as

$$A_{\mathrm{t,CM}}^{\mathrm{FB}} = \frac{\sigma(y_{\mathrm{t}} > y_{\bar{\mathrm{t}}}) - \sigma(y_{\mathrm{t}} < y_{\bar{\mathrm{t}}})}{\sigma(y_{\mathrm{t}} > y_{\bar{\mathrm{t}}}) + \sigma(y_{\mathrm{t}} < y_{\bar{\mathrm{t}}})}. \tag{3.18}$$

At the CDF experiment, these asymmetries have been measured separately in two regions of the $\mathrm{t\bar{t}}$ invariant mass $M_{\mathrm{t\bar{t}}}$, viz. for $M_{\mathrm{t\bar{t}}} > 450\,\mathrm{GeV}$ and $M_{\mathrm{t\bar{t}}} < 450\,\mathrm{GeV}$, with the result [102]

$$\begin{aligned} A_{\mathrm{t,CM}}^{\mathrm{FB,CDF}} &= 0.162(47), \\ A_{\mathrm{t,CM}}^{\mathrm{FB,CDF}}(M_{\mathrm{t\bar{t}}} < 450\,\mathrm{GeV}) &= 0.078(54), \\ A_{\mathrm{t,CM}}^{\mathrm{FB,CDF}}(M_{\mathrm{t\bar{t}}} > 450\,\mathrm{GeV}) &= 0.296(67). \end{aligned} \tag{3.19}$$

The D0 experiment has measured [101]

$$A_{\mathrm{t,CM}}^{\mathrm{FB,D0}} = 0.196(65). \tag{3.20}$$

From our calculation, using $\mu_0 = E_{\mathrm{T}}$ and including FwW effects, we find the results given in the lower part of Table 3. While these results agree well with theoretical calculations of other groups [30, 107], the measured asymmetry is significantly higher, in particular for $M_{\mathrm{t\bar{t}}} > 450\,\mathrm{GeV}$.

3.4.2 Asymmetries for the LHC

At the LHC, the forward-backward asymmetry of the quark- and antiquark-induced partonic subprocesses does not show up in observables, since all distributions are forward–backward symmetric for the proton–proton initial state. However, as a result of the dominance of valence quarks over sea (anti)quarks at large momentum fractions, the partonic asymmetry manifests itself as a hadronic central–edge asymmetry. In practice, in the laboratory frame, antitop quarks tend to be produced more centrally than top quarks. The ATLAS collaboration [108] measures an asymmetry based on the LAB-frame rapidity of the top quarks,

$$A_{\mathrm{t}}^{\mathrm{CE},y} = \frac{\sigma(|y_{\mathrm{t}}| > |y_{\bar{\mathrm{t}}}|) - \sigma(|y_{\mathrm{t}}| < |y_{\bar{\mathrm{t}}}|)}{\sigma(|y_{\mathrm{t}}| > |y_{\bar{\mathrm{t}}}|) + \sigma(|y_{\mathrm{t}}| < |y_{\bar{\mathrm{t}}}|)}, \tag{3.21}$$

μ_0	$A_{\rm t,LAB}^{\rm FB}$	$A_{\rm e^+,LAB}^{\rm FB}$
$m_{\rm t}$	$0.0499(5)^{+0.0342}_{-0.0143}$	$0.0361(5)^{+0.0256}_{-0.0107}$
$E_{\rm T}$	$0.0454(5)^{+0.0259}_{-0.0119}$	$0.0321(5)^{+0.0190}_{-0.0087}$

μ_0	$A_{\rm t,CM}^{\rm FB}$	$A_{\rm t,CM}^{\rm FB}(M_{\rm t\bar{t}} < 450\,{\rm GeV})$	$A_{\rm t,CM}^{\rm FB}(M_{\rm t\bar{t}} > 450\,{\rm GeV})$
$m_{\rm t}$	$0.0749(5)^{+0.0514}_{-0.0214}$	$0.0491(6)^{+0.0267}_{-0.0126}$	$0.1281(11)^{+0.1286}_{-0.0421}$
$E_{\rm T}$	$0.0683(5)^{+0.0391}_{-0.0181}$	$0.0486(6)^{+0.0250}_{-0.0122}$	$0.1078(9)^{+0.0737}_{-0.0307}$

Table 3: Forward–backward asymmetries for the top quark and the charged lepton at the Tevatron including FwW effects, using a dynamical $\mu_0 = E_{\rm T}$ or a fixed $\mu_0 = m_{\rm t}$ scale.

$E_{\rm CM}$[TeV]	μ_0	$A_{\rm t}^{{\rm CE},y}$	$A_{\rm t}^{{\rm CE},\eta}$	$A_l^{{\rm CE},y} = A_l^{{\rm CE},\eta}$
7	$m_{\rm t}/2$	$0.0078(9)^{+0.0050}_{-0.0020}$	$0.0100(9)^{+0.0068}_{-0.0026}$	$0.0050(9)^{+0.0034}_{-0.0013}$
7	$E_{\rm T}/2$	$0.0075(7)^{+0.0038}_{-0.0017}$	$0.0093(7)^{+0.0049}_{-0.0022}$	$0.0045(7)^{+0.0022}_{-0.0010}$
8	$m_{\rm t}/2$	$0.0063(8)^{+0.0039}_{-0.0016}$	$0.0087(8)^{+0.0058}_{-0.0024}$	$0.0027(8)^{+0.0012}_{-0.0005}$
8	$E_{\rm T}/2$	$0.0050(7)^{+0.0021}_{-0.0010}$	$0.0070(8)^{+0.0033}_{-0.0016}$	$0.0037(7)^{+0.0014}_{-0.0007}$
14	$m_{\rm t}/2$	$0.0024(9)^{+0.0016}_{-0.0007}$	$0.0034(9)^{+0.0021}_{-0.0010}$	$0.0021(9)^{+0.0013}_{-0.0006}$
14	$E_{\rm T}/2$	$0.0032(8)^{+0.0015}_{-0.0008}$	$0.0047(8)^{+0.0022}_{-0.0012}$	$0.0021(8)^{+0.0009}_{-0.0005}$

Table 4: Central–edge asymmetries for the top quark and the charged lepton for the LHC at different CM energies including FwW effects, using a dynamical $\mu_0 = E_{\rm T}/2$ or a fixed $\mu_0 = m_{\rm t}/2$ scale.

while CMS [109] prefers to investigate an asymmetry based on the pseudo-rapidity,

$$A_{\rm t}^{{\rm CE},\eta} = \frac{\sigma(|\eta_{\rm t}| > |\eta_{\bar{\rm t}}|) - \sigma(|\eta_{\rm t}| < |\eta_{\bar{\rm t}}|)}{\sigma(|\eta_{\rm t}| > |\eta_{\bar{\rm t}}|) + \sigma(|\eta_{\rm t}| < |\eta_{\bar{\rm t}}|)}. \tag{3.22}$$

Again these asymmetries can be defined for charged leptons as well,

$$A_l^{{\rm CE},y} = \frac{\sigma(|y_{\rm e^+}| > |y_{\mu^-}|) - \sigma(|y_{\rm e^+}| < |y_{\mu^-}|)}{\sigma(|y_{\rm e^+}| > |y_{\mu^-}|) + \sigma(|y_{\rm e^+}| < |y_{\mu^-}|)}. \tag{3.23}$$

Since the charged leptons can be considered massless, $A_l^{{\rm CE},y} = A_l^{{\rm CE},\eta}$. Results for the top-quark and charged-lepton central–edge asymmetries for the dynamical $\mu_0 = E_{\rm T}/2$ and fixed $\mu_0 = m_{\rm t}/2$ scale and with FwW effects are given in Table 4. Also in this case FwW effects turn out to be strongly suppressed (at the sub-per-mille level).

3.5 Differential distributions

In the following we present various distributions obtained by applying the cuts specified in Section 3.2. For each of the observables illustrated in Figures 8–30 we present three plots. The left plots display absolute LO (blue, dashed) and NLO (red, solid) predictions together with corresponding uncertainty bands resulting from scale variations

within $0.5 < \mu/\mu_0 < 2$. In the upper–right plots we show the same LO and NLO predictions normalized to LO results at the central scale, i.e. $K_{\rm LO}(\mu) = {\rm d}\sigma_{\rm LO}(\mu)/{\rm d}\sigma_{\rm LO}(\mu_0)$ and $K_{\rm NLO}(\mu) = {\rm d}\sigma_{\rm NLO}(\mu)/{\rm d}\sigma_{\rm LO}(\mu_0)$. Here the blue band illustrates the relative scale uncertainty of the LO cross section, and the central curve of the red band corresponds to the usual NLO correction factor, $K = K_{\rm NLO}(\mu_0)$. These first two plots always include FwW effects, whose impact is illustrated in the lower–right plots. There we display the FwW correction factor

$$\Delta_{\rm FwW} = \frac{{\rm d}\sigma^{\rm FwW}}{{\rm d}\sigma^{\rm NwWA}} - 1, \tag{3.24}$$

obtained by comparing the NwWA and the FwW variants of our calculation.

All results in Figures 10–30 are obtained with the dynamical scales $\mu_0 = E_{\rm T}/2$ at the LHC and $\mu_0 = E_{\rm T}$ at Tevatron. To motivate this choice, we first show, in Figures 8 and 9, that using a fixed scale $\mu = m_{\rm t}/2$ at the LHC leads to serious perturbative instabilities in the high-energy tails of distributions.

3.5.1 Differential distributions for the LHC at 8 TeV

We first provide results for the LHC at 8 TeV. As examples for typical $p_{\rm T}$ distributions we present the distributions in the transverse momenta of the positron and of the top quark for the fixed scale $\mu = m_{\rm t}/2$ in Figures 8 and 9. The tails of these distributions are relevant for new-physics searches based on boosted top quarks, while the lepton-$p_{\rm T}$ distribution plays an important role for the $\rm t\bar{t}$ cross-section acceptance. The typical lepton $p_{\rm T}$ is below 100 GeV and the average $p_{\rm T}$ of the top quark is around 100 GeV. The FwW effects are within integration errors. In the plotted range, the cross section falls by almost four orders of magnitude, while the K factor drops by 75%. In the high-$p_{\rm T}$ tails, the corrections become so large that NLO predictions move outside the LO band and their scale variation exceeds -100%. This pathologic behaviour at large $p_{\rm T}$ can (at least in part) be attributed to large logarithms associated with the running of $\alpha_{\rm s}$, which can be effectively resummed by adapting the QCD renormalization scale to the characteristic scattering energy. This motivates us to adopt the dynamical scale $\mu_0 = E_{\rm T}/2$ as our standard LHC scale choice, which is applied to all LHC observables presented in the following.

The $p_{\rm T,e^+}$ and $p_{\rm T,t}$ distributions, displayed in Figures 10 and 11, show that the dynamical scale choice leads to a drastic improvement of the perturbative stability. Now the K factor changes only slightly with $p_{\rm T}$ (within 20%), and the NLO band lies within the LO band.

Next we consider the distributions in the transverse momenta of the harder b jet (the one with larger $p_{\rm T}$) and the softer b jet in Figures 12 and 13. The corrections to the transverse-momentum distribution of the harder b jet are small near the maximum of the distribution and increase slowly for higher $p_{\rm T}$ by about 40%, while those for the distribution of the softer b jet decrease by 20%. Using the fixed scale $\mu_0 = m_{\rm t}/2$ (not shown), the K factor to the $p_{\rm T,b,max}$ distribution decreases by 40% and the one for the $p_{\rm T,b,min}$ distribution even by 90%. FwW effects are at the level of 1% or below.

The distribution in the transverse momentum of the $\rm b\bar{b}$ pair is presented in Figure 14. This variable plays an important role in boosted-Higgs searches with a large $\rm t\bar{t}$ background. In particular, the strategy proposed in Refs. [110, 111] to extract a $\rm pp \to H(\to b\bar{b})W$

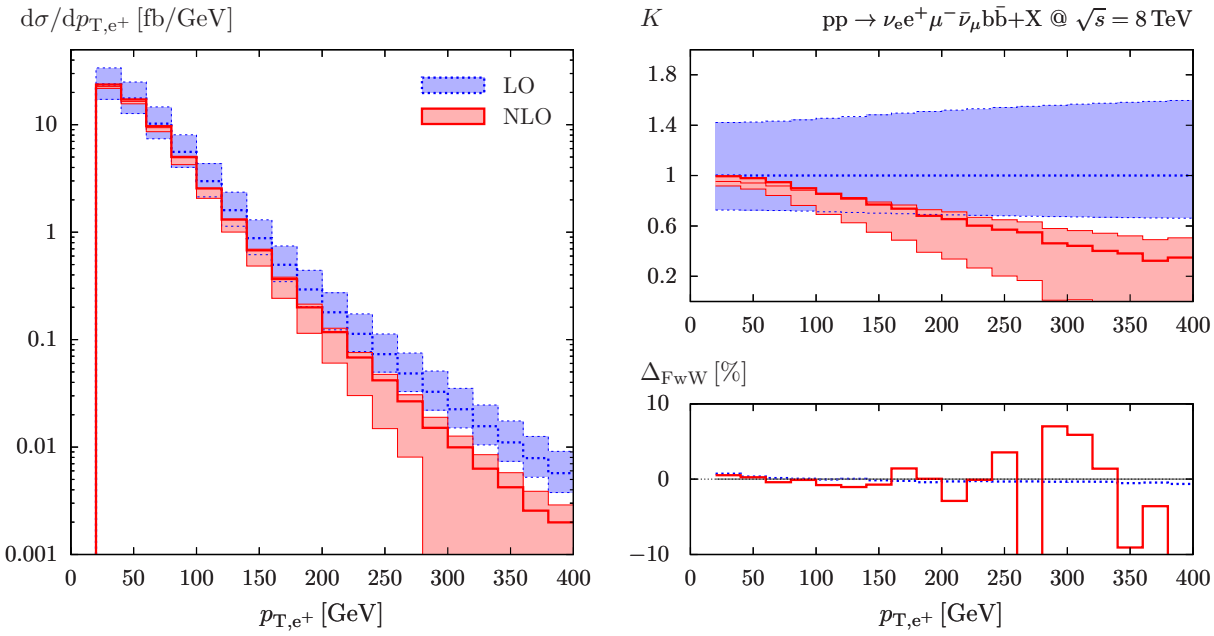

Figure 8: Transverse-momentum distribution of the positron with standard cuts for the LHC at $\sqrt{s} = 8\,\text{TeV}$ for fixed scale $\mu_0 = m_\text{t}/2$.

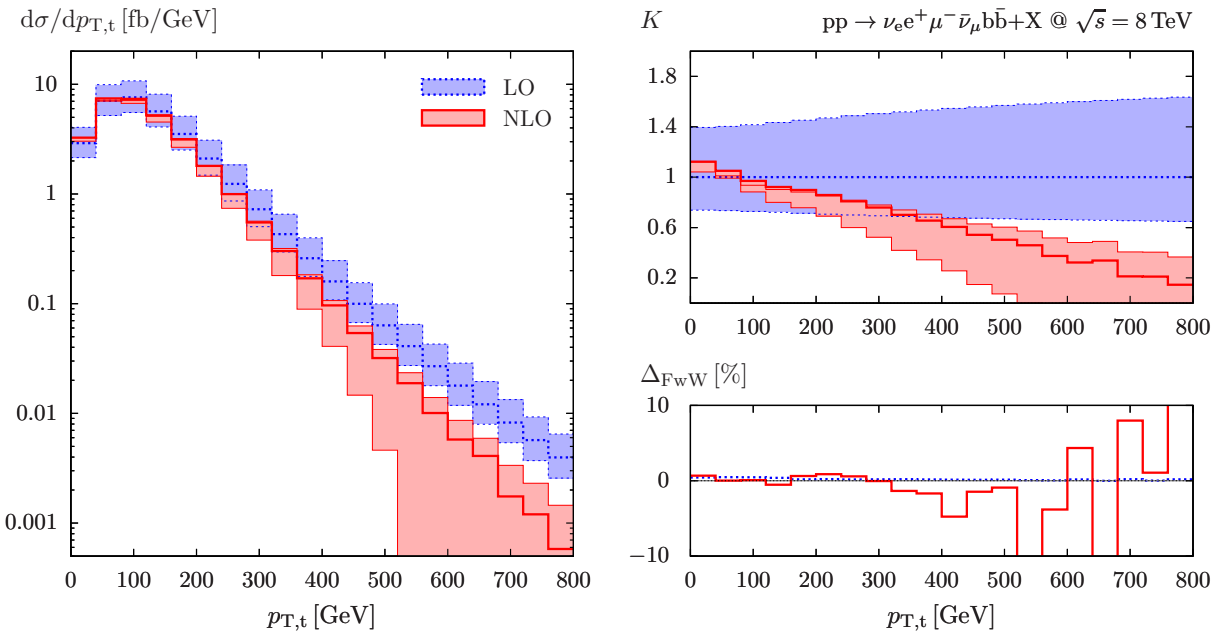

Figure 9: Transverse-momentum distribution of the top quark with standard cuts for the LHC at $\sqrt{s} = 8\,\text{TeV}$ for fixed scale $\mu_0 = m_\text{t}/2$.

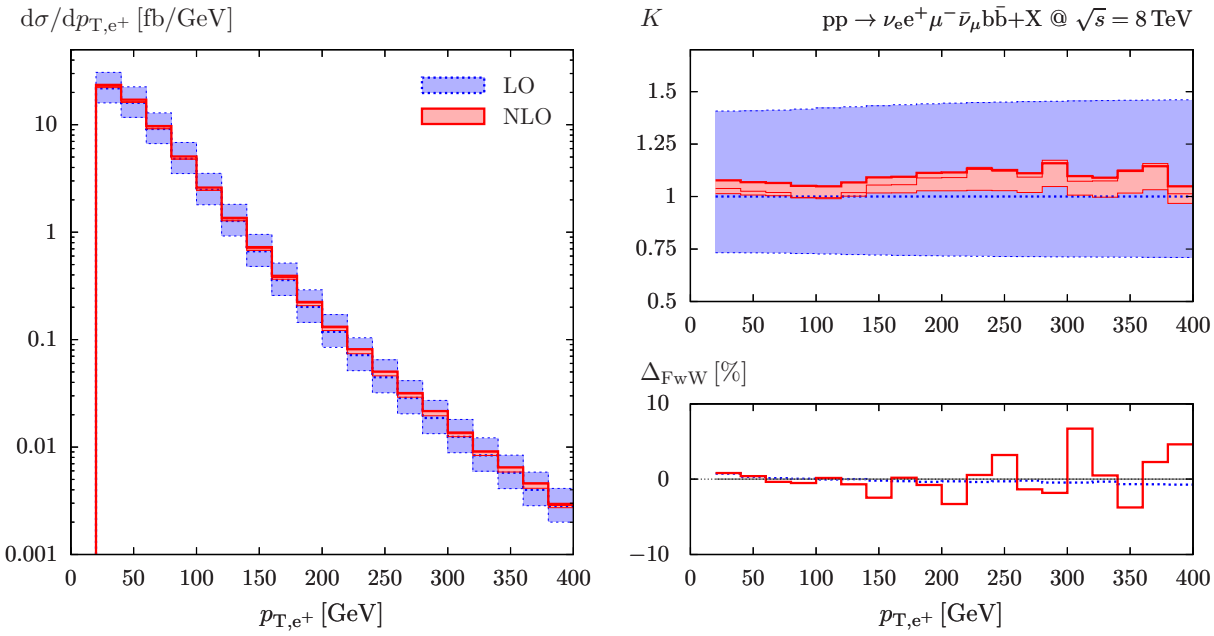

Figure 10: Transverse-momentum distribution of the positron with standard cuts for the LHC at $\sqrt{s} = 8\,\text{TeV}$ for dynamical scale $\mu_0 = E_\text{T}/2$.

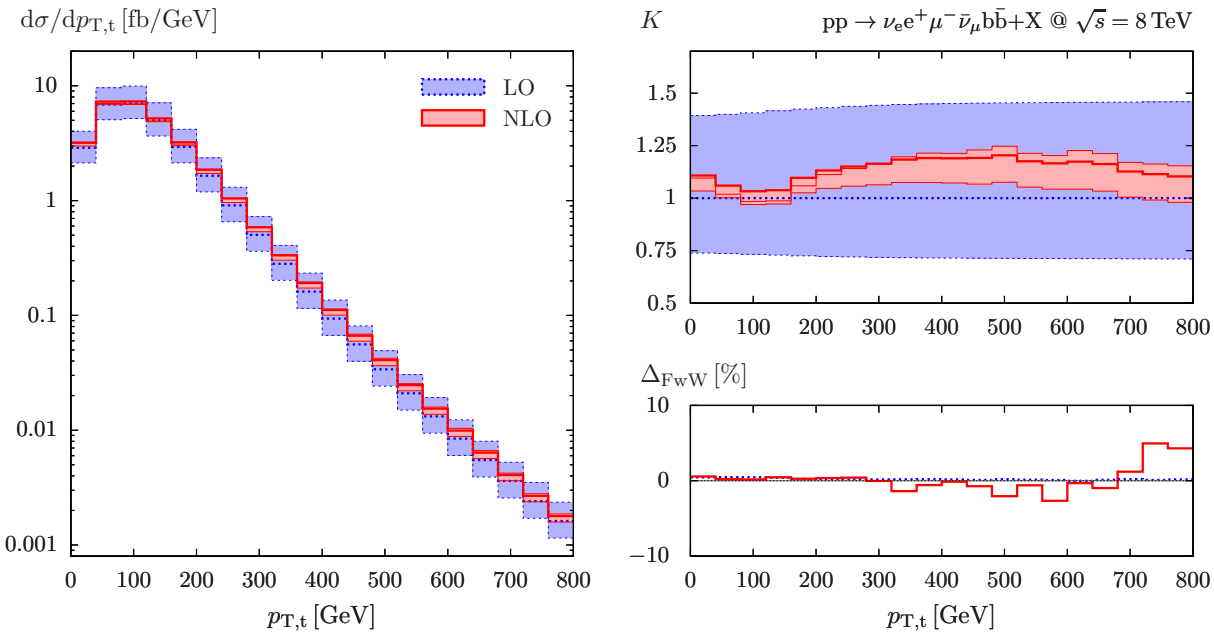

Figure 11: Transverse-momentum distribution of the top quark with standard cuts for the LHC at $\sqrt{s} = 8\,\text{TeV}$ for dynamical scale $\mu_0 = E_\text{T}/2$.

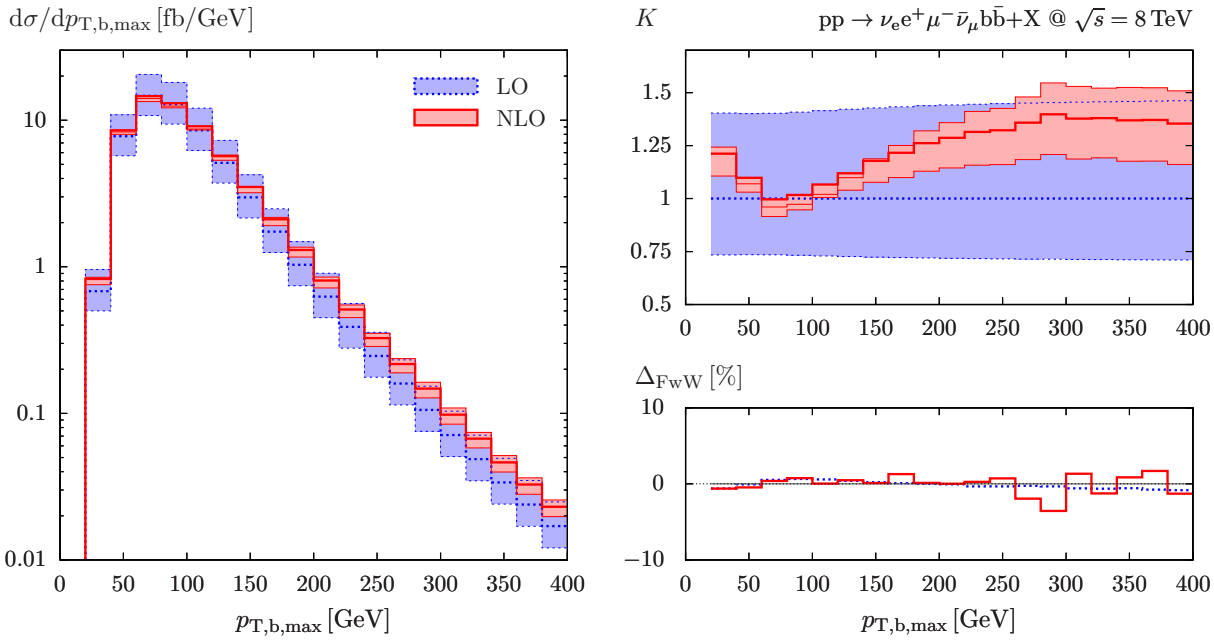

Figure 12: Transverse-momentum distribution of the harder b jet with standard cuts for the LHC at $\sqrt{s} = 8\,\text{TeV}$ for dynamical scale $\mu_0 = E_\text{T}/2$.

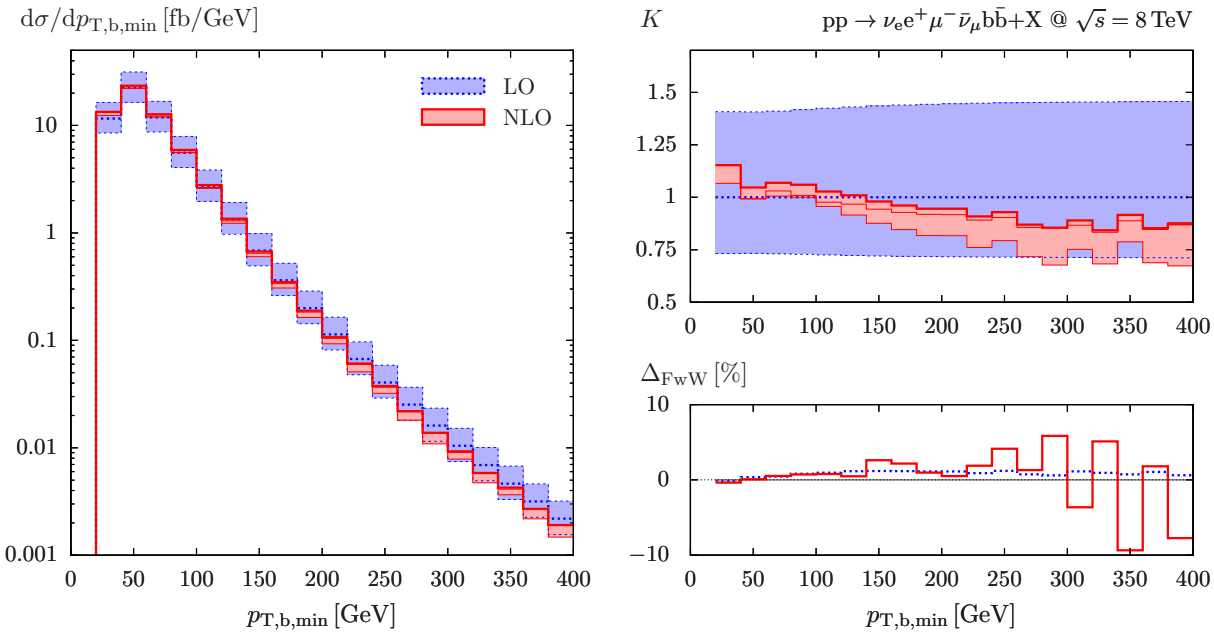

Figure 13: Transverse-momentum distribution of the softer b jet with standard cuts for the LHC at $\sqrt{s} = 8\,\text{TeV}$ for dynamical scale $\mu_0 = E_\text{T}/2$.

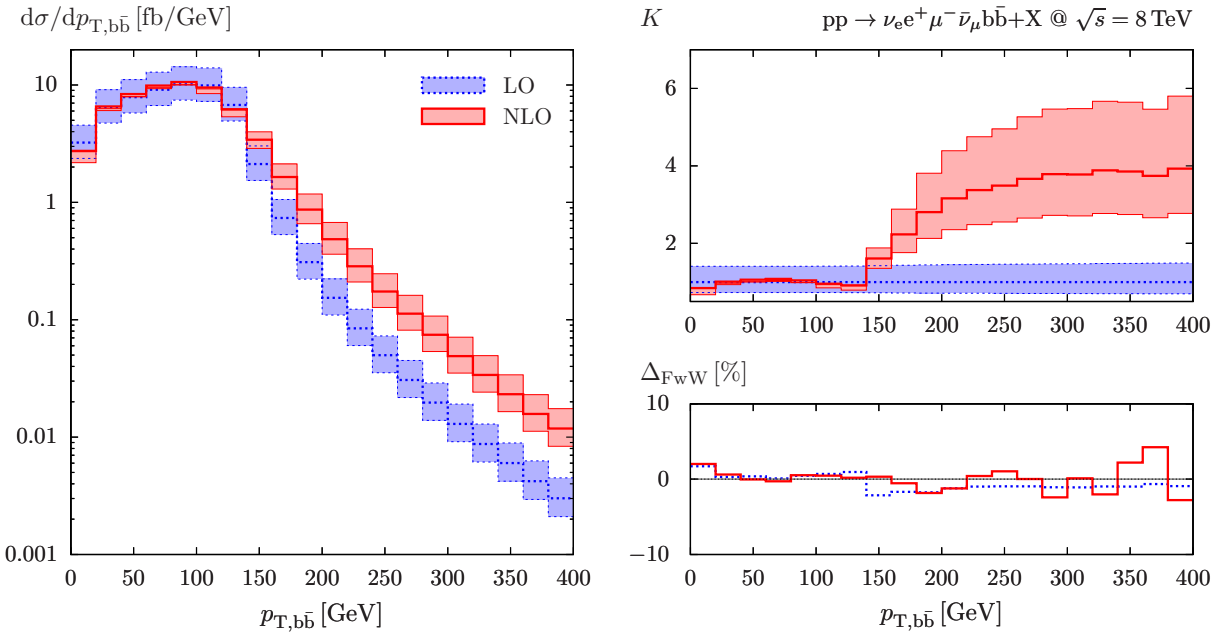

Figure 14: Transverse-momentum distribution of the $\mathrm{b\bar{b}}$ pair with standard cuts for the LHC at $\sqrt{s} = 8\,\mathrm{TeV}$ for dynamical scale $\mu_0 = E_\mathrm{T}/2$.

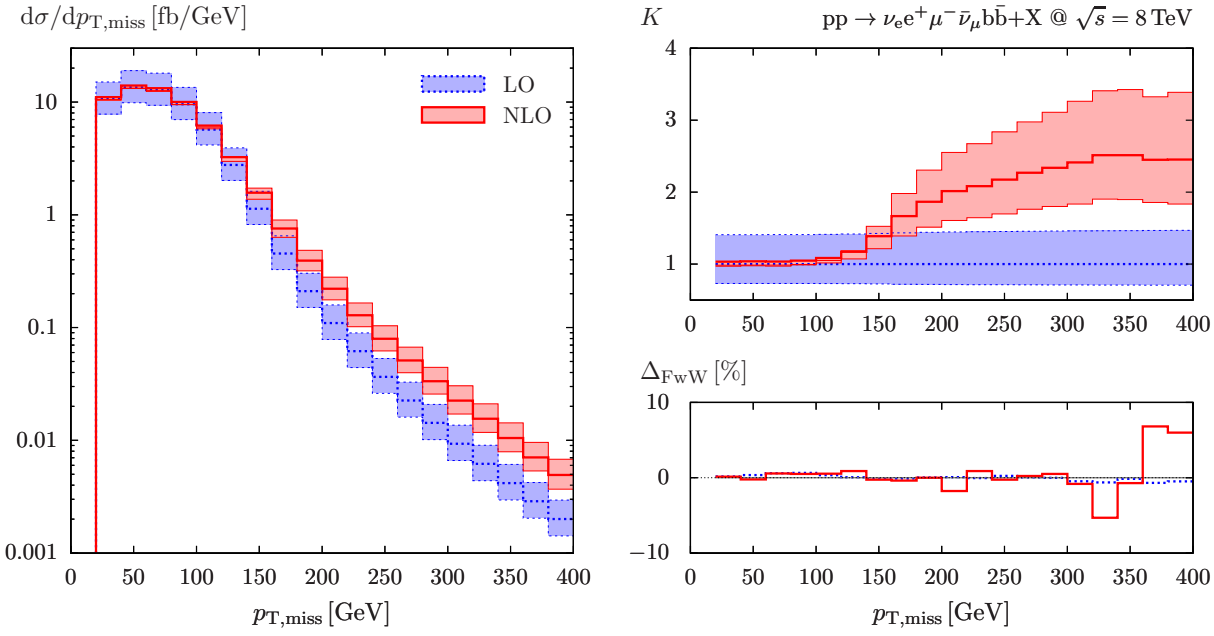

Figure 15: Missing-transverse-momentum distribution with standard cuts for the LHC at $\sqrt{s} = 8\,\mathrm{TeV}$ for dynamical scale $\mu_0 = E_\mathrm{T}/2$.

signal at the LHC is based on the selection of boosted $H \to b\bar{b}$ candidates with $p_{T,b\bar{b}} > 200\,\text{GeV}$, which permits to reduce $t\bar{t}$ contamination (and other backgrounds) in a very efficient way. As can be seen from Figure 14, the suppression of $t\bar{t}$ production is indeed particularly strong at $p_{T,b\bar{b}} \gtrsim 150\,\text{GeV}$. This is due to the fact that, in NtWA, b quarks need to be boosted via the p_T of their parent (anti)top quarks in order to acquire $p_{T,b} > (m_t^2 - M_W^2)/(2m_t) \simeq 65\,\text{GeV}$, and a $b\bar{b}$ system with high p_T is kinematically strongly disfavoured at LO, since top and antitop quarks have opposite transverse momenta. The NLO corrections undergo less stringent kinematic restrictions, resulting in a significant enhancement of $WWb\bar{b}$ events at large $p_{T,b\bar{b}}$. This is clearly reflected in the differences between the LO and NLO curves in the left plot of Fig. 14. At NLO the $t\bar{t}$ system can acquire large transverse momentum by recoiling against extra jet radiation. As indicated by the upper–right plot, the NLO correction represents 50−80% of the cross section at high p_T, corresponding to a huge K-factor of 2−4. FwW effects (lower–right plot) stay at the level of 2%. On the other hand, FtW effects (not shown here explicitly) become as large as 10–30% for $p_{T,b\bar{b}} > 200\,\text{GeV}$ [63]. This is most likely due to non-resonant topologies with direct $b\bar{b}$ production from a high-p_T gluon that recoils against a W^+W^- system and splits into a $b\bar{b}$ pair.

Figure 15 displays the distribution in the missing transverse momentum, $p_{T,\text{miss}} = |\vec{p}_{T,\nu_e} + \vec{p}_{T,\bar{\nu}_\mu}|$. The tail of this distribution, which is relevant for new-physics searches based on missing transverse energy plus jets and leptons, features a qualitatively similar behaviour as in the case of $p_{T,b\bar{b}}$, owing to analogous kinematic constraints. However, in the case of $p_{T,\text{miss}}$ the corrections are less pronounced: the K factor only rises to 2.5. FwW contributions are not significant.

The distribution in the invariant mass of the top quark, $M_t = M_{\nu_e e^+ b}$, in the vicinity of its resonance is shown in Figure 16. Below the resonance the NLO corrections develop a radiative tail of positive corrections due to final-state gluon radiation that is not recombined with the top-quark decay products. The NLO corrections induce a small shift in the peak of the distribution, whose magnitude depends on the jet recombination. Note that the major part of this shift would also be accounted for in a pure parton-shower approach to describe higher-order QCD effects. Thus, a thorough assessment of the impact of the full NLO QCD calculation with off-shell top quarks on observables that are used in the top mass measurement requires a careful comparison with predictions based on parton showers. Note also that FwW corrections increase in the side bands of the resonance to the level of a few per cent.

Figure 17 displays the distribution in the invariant mass of the positron and a b jet, i.e. the visible products of a top-quark decay. We here use the Monte Carlo truth to select the negatively charged b-quark jet.[9] In narrow-top-width and LO approximation this kinematic quantity is characterized by a sharp upper bound, $M_{e^+b}^2 < m_t^2 - M_W^2 \simeq (152\,\text{GeV})^2$, which renders it very sensitive to the top-quark mass. The value of m_t can be extracted with high precision using, for instance, the invariant-mass distribution of a positron and a J/ψ from a B-meson decay [112, 113], an observable that is closely related to M_{e^+b}. In the region below the kinematic bound, the NLO corrections to M_{e^+b} vary between −10% and 20%, and the impact of the NLO shape distortion on a precision m_t measurement is certainly significant. For $M_{e^+b} < 150\,\text{GeV}$, the NwWA is very good. Above the kinematic

[9] In Ref. [29] the e^+b pair is formed by selecting the b jet that yields the smallest invariant mass.

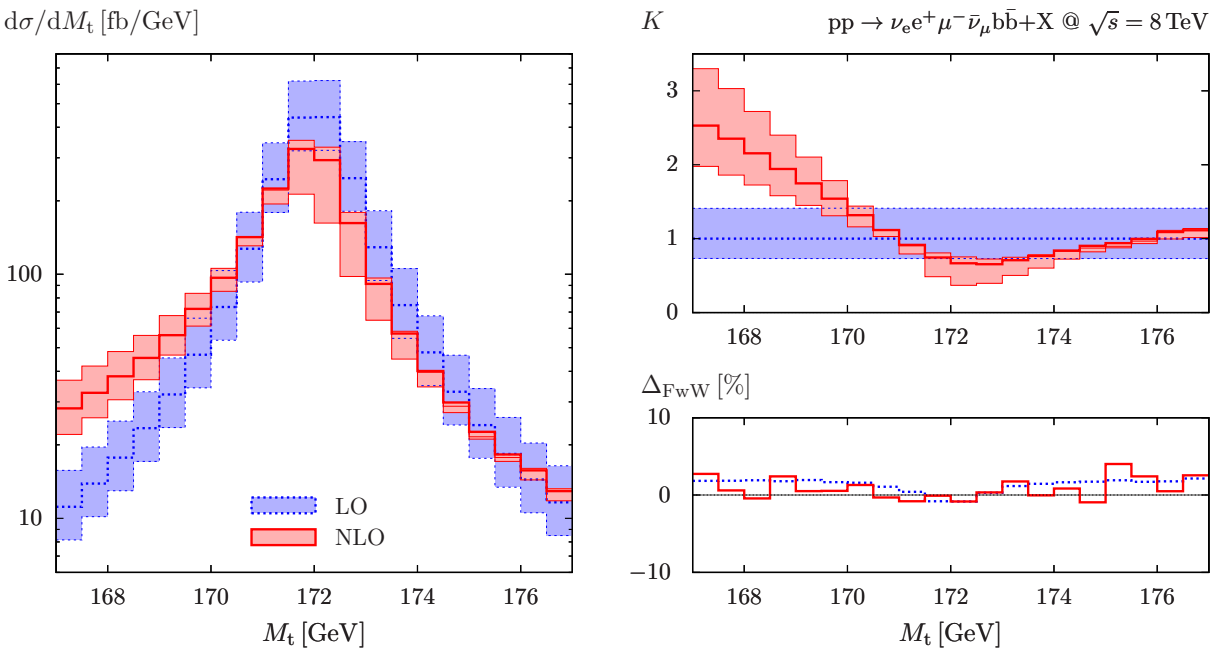

Figure 16: Invariant-mass distribution of the top quark, $M_{\mathrm{t}} = M_{\nu_{\mathrm{e}}\mathrm{e}^+\mathrm{b}}$, with standard cuts for the LHC at $\sqrt{s} = 8\,\mathrm{TeV}$ for dynamical scale $\mu_0 = E_{\mathrm{T}}/2$.

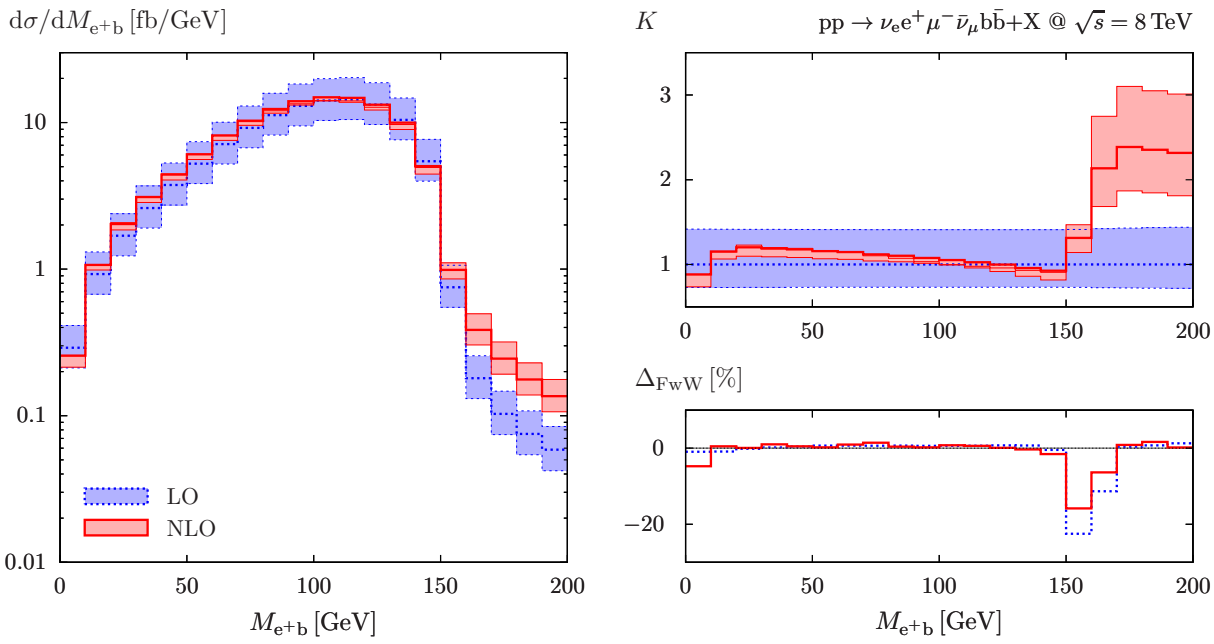

Figure 17: Invariant-mass distribution of positron–b-jet system with standard cuts for the LHC at $\sqrt{s} = 8\,\mathrm{TeV}$ for dynamical scale $\mu_0 = E_{\mathrm{T}}/2$.

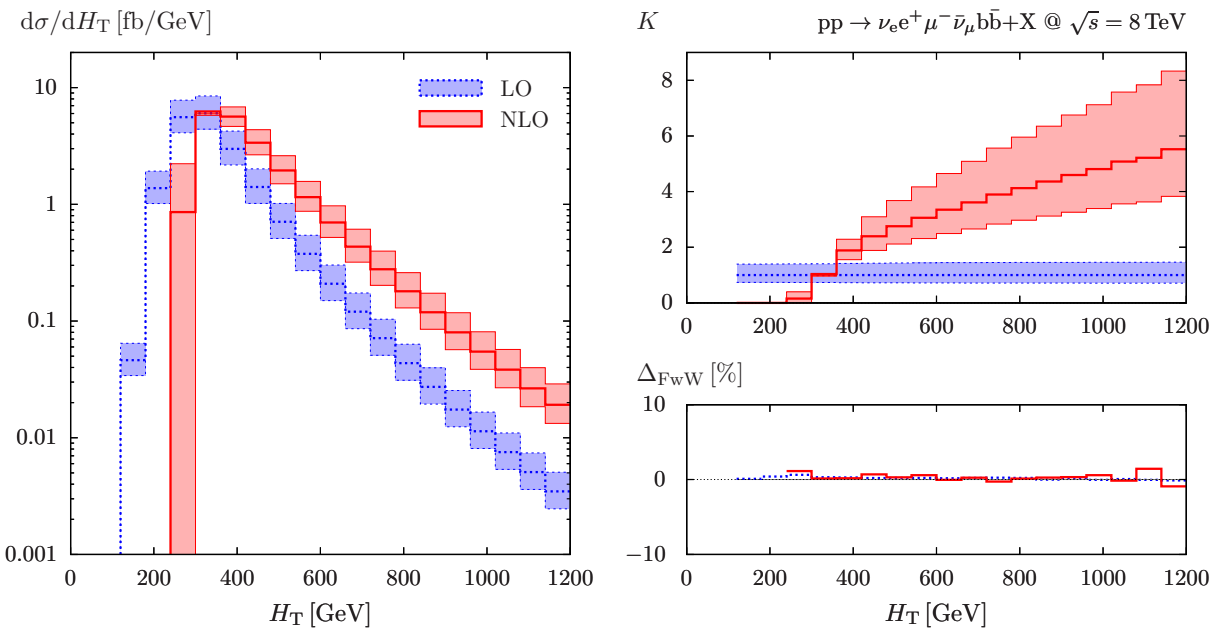

Figure 18: Distribution in the total transverse energy H_{T} with standard cuts for the LHC at $\sqrt{s} = 8\,\mathrm{TeV}$ for dynamical scale $\mu_0 = E_{\mathrm{T}}/2$.

bound, NLO corrections become clearly visible, giving rise to a tail that extends above $M^2_{\mathrm{e^+b}} = m^2_{\mathrm{t}} - M^2_{\mathrm{W}}$, and also FwW corrections become sizeable. In this kinematic region also the finite top width causes effects at the level of 50% [63]. While the contribution to the total cross section from the region above 150 GeV is fairly small, the impact of these contributions on the top-mass measurement might be non-negligible, given the high m_{t} sensitivity of the $M^2_{\mathrm{e^+b}} \simeq m^2_{\mathrm{t}} - M^2_{\mathrm{W}}$ region. Again a careful comparison between NLO off-shell calculation and parton-shower approach would be required to quantify off-shell effects on the m_{t} measurement.

In Figure 18 we display the distribution in the total transverse energy,

$$H_{\mathrm{T}} = p_{\mathrm{T,e^+}} + p_{\mathrm{T},\mu^-} + p_{\mathrm{T,miss}} + \sum_j p_{\mathrm{T},j}, \tag{3.25}$$

where the scalar sum over the jet transverse momenta, $p_{\mathrm{T},j}$, includes the two b-quark jets as well as possible extra jets contributing to NLO real emission. The H_{T} distribution is relevant for new-physics searches. The large correction above $H_{\mathrm{T}} = 400\,\mathrm{GeV}$ results from the inclusion of the gluon jet, which shifts the distribution to higher H_{T}. If this is not included, as e.g. in Ref. [33], the K factor is flat and varies between 0.8 and 1.2.

Finally, we show the distributions in the invariant masses of the $\mathrm{b\bar{b}}$ and $\mathrm{t\bar{t}}$ pairs, in Figures 19 and 20, and the distributions in the azimuthal angle between the two charged leptons in the transverse plane and the cosine of the angle between them, in Figures 21 and 22. In general these distributions receive moderate shape corrections, and FwW effects are tiny. Sizable NLO and FwW effects show up only in the $M_{\mathrm{t\bar{t}}}$ distribution below the $\mathrm{t\bar{t}}$ threshold.

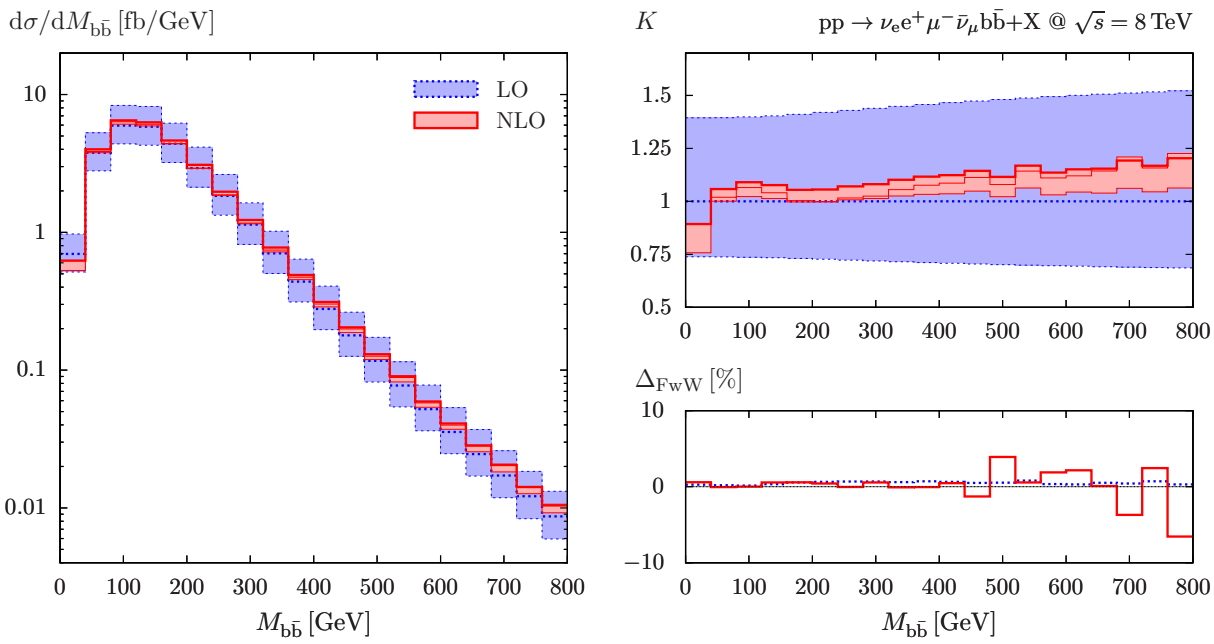

Figure 19: Invariant-mass distribution of the $\mathrm{b\bar{b}}$ pair with standard cuts for the LHC at $\sqrt{s} = 8\,\mathrm{TeV}$ for dynamical scale $\mu_0 = E_\mathrm{T}/2$.

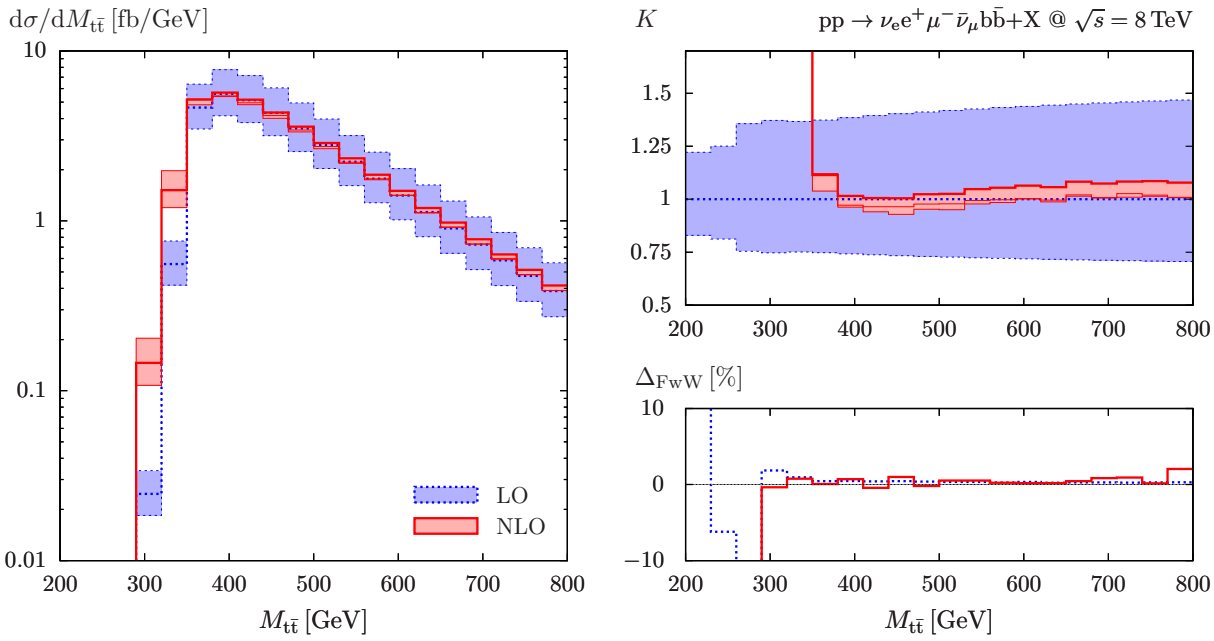

Figure 20: Distribution in the invariant mass of the $\mathrm{t\bar{t}}$ pair with standard cuts for the LHC at $\sqrt{s} = 8\,\mathrm{TeV}$ for dynamical scale $\mu_0 = E_\mathrm{T}/2$.

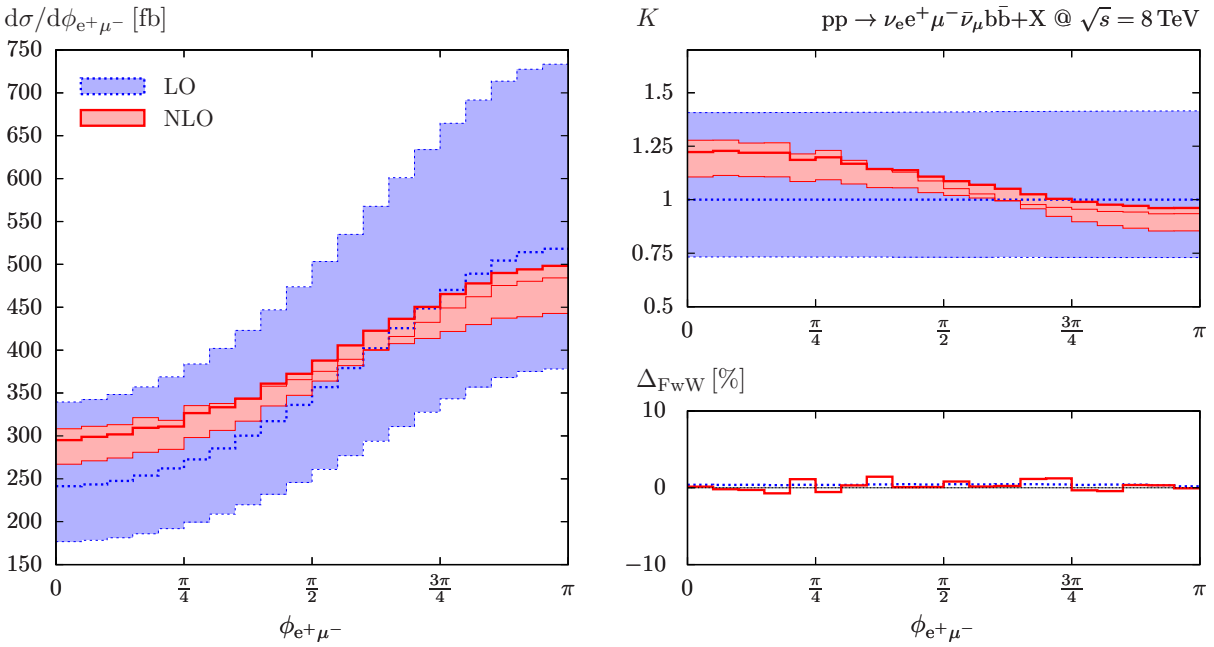

Figure 21: Distribution in the azimuthal angle between the positron and the muon in the transverse plane, $\phi_{e^+\mu^-}$, with standard cuts for the LHC at $\sqrt{s} = 8\,\text{TeV}$ for dynamical scale $\mu_0 = E_T/2$.

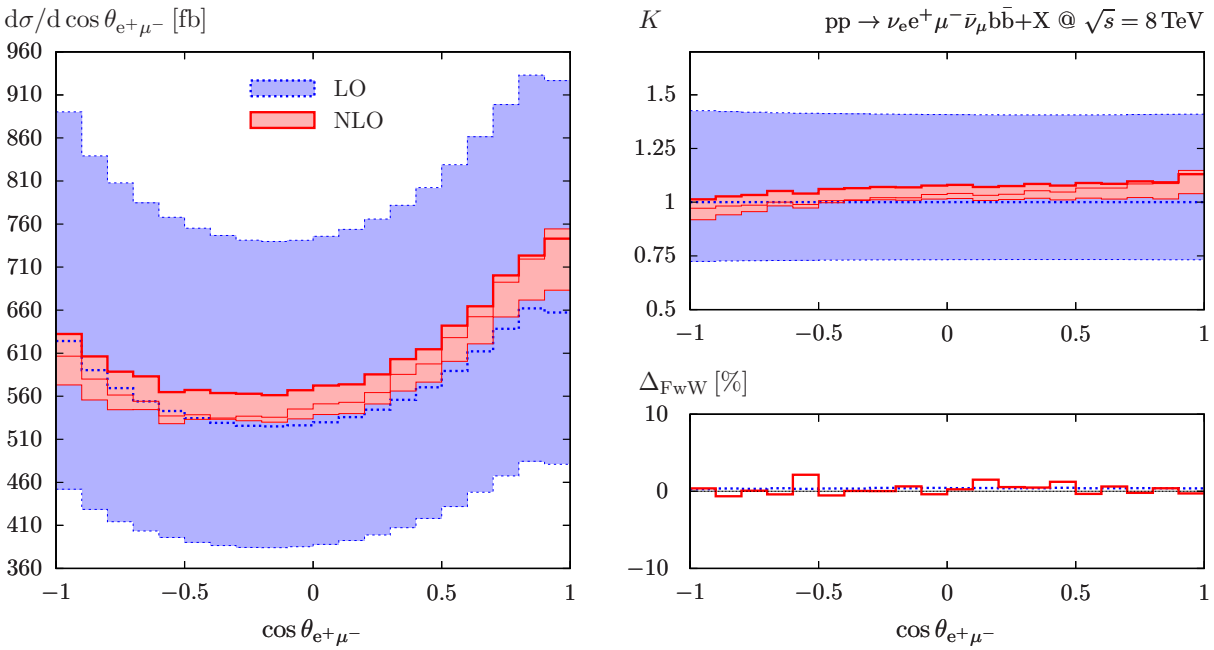

Figure 22: Distribution in the cosine of the angle between the positron and the muon, $\cos\theta_{e^+\mu^-}$, with standard cuts for the LHC at $\sqrt{s} = 8\,\text{TeV}$ for dynamical scale $\mu_0 = E_T/2$.

3.5.2 *Differential distributions for the LHC at* 14 TeV

At the LHC with 14 TeV, using the dynamical scale $\mu_0 = E_T/2$, we observe that the shapes of the distributions and the NLO corrections look qualitatively similar as for 8 TeV. However, the K factors for transverse-momentum distributions grow faster with p_T than at 8 TeV. In Figures 23 and 24 we show results for the distributions in the transverse momenta of the positron and of the harder b jet. Above $p_T = 100$ GeV, the K factor grows by about 30% for the p_{T,e^+} distribution and by about 60% for the $p_{T,b,max}$ distribution. Using the fixed scale $\mu = m_t/2$ instead (not shown), the K factor decreases by about 40% for the p_{T,e^+} distribution and by about 20% for the $p_{T,b,max}$ distribution. In general, FwW corrections remain similarly suppressed as at 8 TeV.

3.5.3 *Differential distributions for Tevatron*

Next we show a few distributions for Tevatron, using the dynamical scale $\mu_0 = E_T$. The transverse-momentum distribution of the positron is presented in Figure 25. The K factor decreases slightly with increasing p_T. FwW effects are completely negligible.

We turn to the distributions in the transverse momenta of the harder b jet and the softer b jet in Figures 26 and 27. Below the maxima of the distributions we find a positive K factor at the level of 40%, but above $p_{T,b} = 70$ GeV the K factor is pretty flat and close to one. For large $p_{T,b,min}$ FwW effects at the level of 2% show up.

The distribution in the transverse momentum of the $b\bar{b}$ pair is presented in Figure 28. In contrast to the LHC there is no enhancement of WWb$\bar{b}$ events at large $p_{T,b\bar{b}}$, and the K factor stays near one in the complete considered p_T range. A similar behaviour can be observed for the missing-transverse-momentum distribution (not shown).

The distribution in the invariant mass of the top quark in the vicinity of its resonance is shown in Figure 29. While the enhancement of the distribution by NLO corrections below the resonance is similar as for the LHC, the rise of the K factor above the resonance is weaker. In the side bands of the resonance FwW corrections are at the level of a few per cent as at the LHC.

The distribution in the total transverse energy as defined in (3.25) is presented in Figure 30. The effect of the NLO corrections is qualitatively similar as for the LHC, but the enhancement of the distribution for high H_T is only 40%. As for the LHC, the K factor would become much flatter if the gluon p_T was not included in H_T.

3.6 Limit of on-shell top quarks

To quantify non-resonant and off-shell-top contributions to the $\nu_e e^+ \mu^- \bar{\nu}_\mu b\bar{b}$ integrated cross section, we have investigated its narrow-top-width limit, $\Gamma_t \to 0$, by means of a numerical extrapolation. This is shown in Figure 31, where we plot

$$\bar{\sigma}(\Gamma_t) = \sigma(\Gamma_t) \left(\frac{\Gamma_t}{\Gamma_t^{\text{phys}}} \right)^2 \tag{3.26}$$

in the range $0 < \Gamma_t \leq \Gamma_t^{\text{phys}}$, where Γ_t^{phys} is the physical top-quark width. The factor $(\Gamma_t/\Gamma_t^{\text{phys}})^2$ compensates deviations of Γ_t from Γ_t^{phys} in such a way that the effective

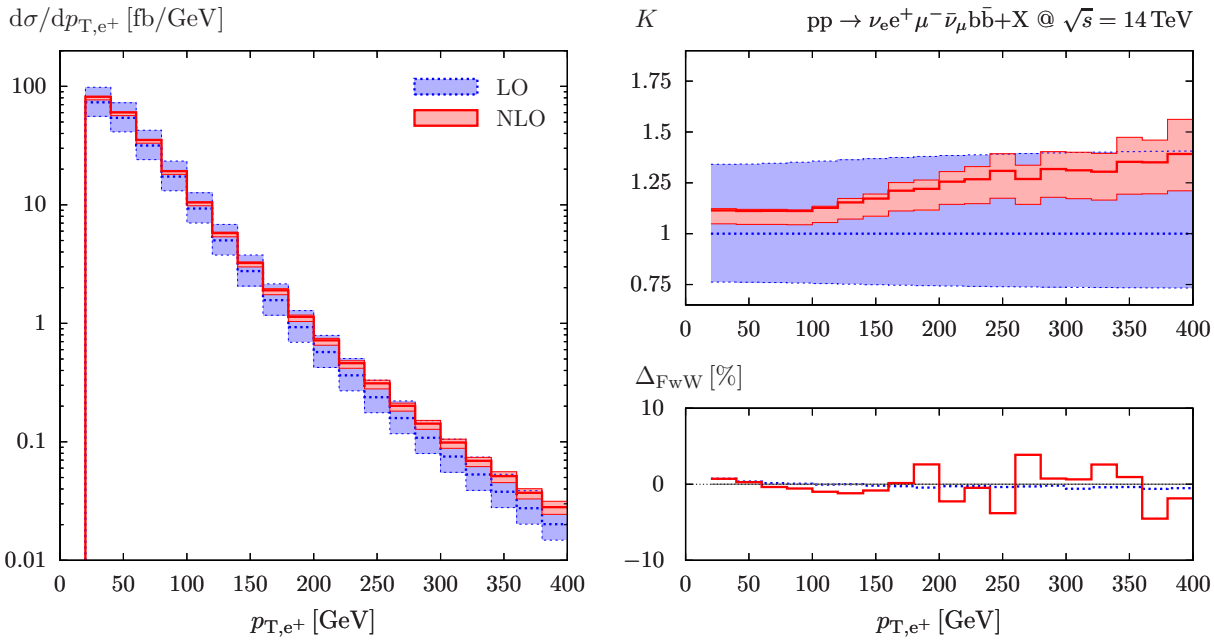

Figure 23: Transverse-momentum distribution of the positron with standard cuts for the LHC at $\sqrt{s} = 14\,\text{TeV}$ for dynamical scale $\mu_0 = E_\text{T}/2$.

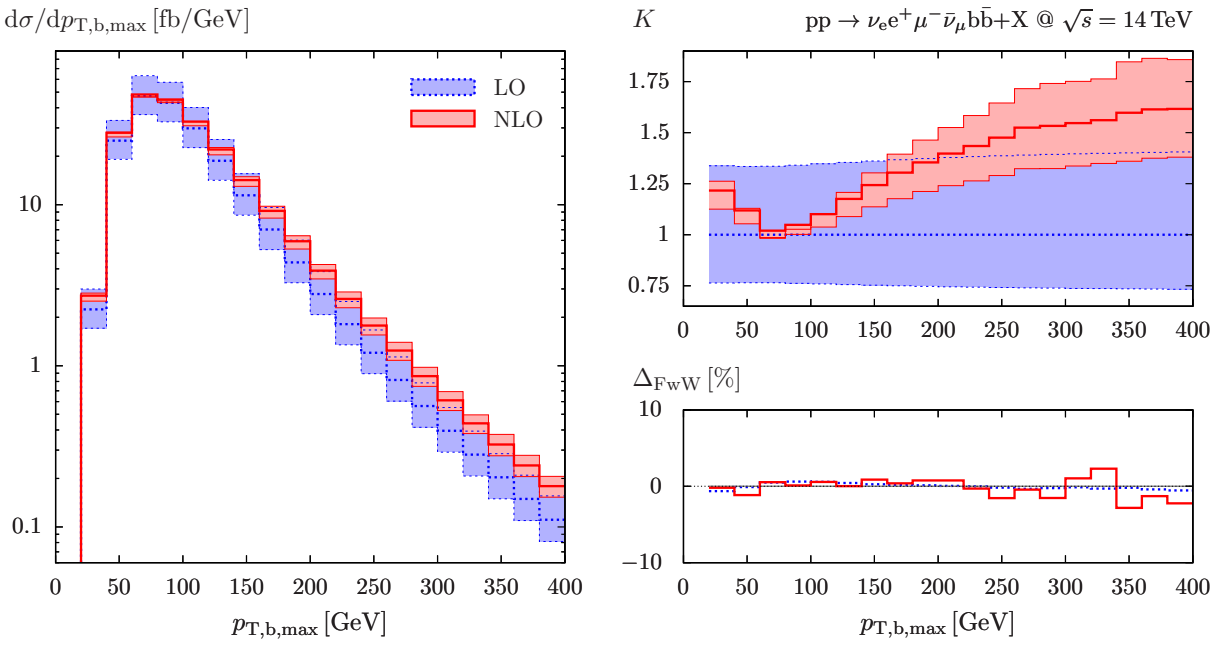

Figure 24: Transverse-momentum distribution of the harder b jet with standard cuts for the LHC at $\sqrt{s} = 14\,\text{TeV}$ for dynamical scale $\mu_0 = E_\text{T}/2$.

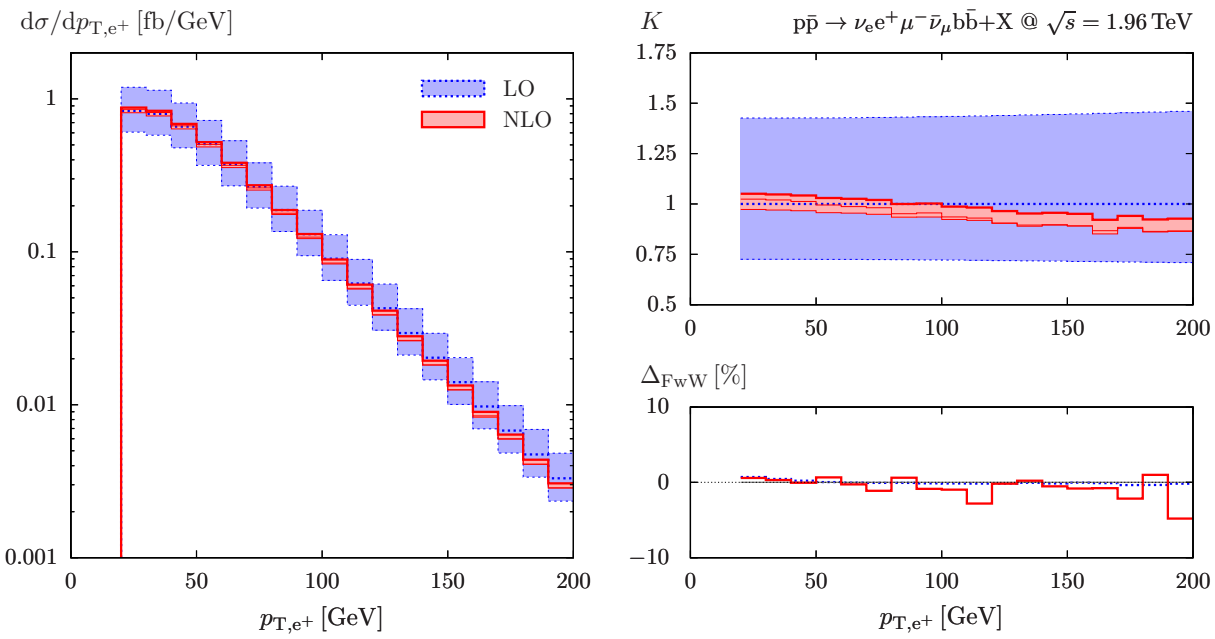

Figure 25: Transverse-momentum distribution of the positron with standard cuts for Tevatron for dynamical scale $\mu_0 = E_T$.

top-decay branching fractions remain constant. The consistency of the $\Gamma_t \to 0$ extrapolation at LO is demonstrated by the green squares in Figure 31, which were obtained with an explicit Born calculation in NtWA. At NLO, when $\Gamma_t \to 0$ the virtual and real parts of NLO corrections are individually enhanced by soft-gluon logarithmic singularities $\propto \alpha_s \ln \Gamma_t$, which are not reshuffled via Catani–Seymour dipoles. The precise numerical cancellation of such singularities in the sum of virtual and real corrections manifests itself in the quality of the linear convergence of the $\Gamma_t \to 0$ extrapolation. This provides a non-trivial confirmation of the consistency and numerical stability of the calculation. Finite-top-width effects are extracted by comparing results at $\Gamma_t = \Gamma_t^{\text{phys}}$ and $\Gamma_t \to 0$. At the Tevatron, we find that FtW effects shift the LO(NLO) cross section by $-0.8\%(-0.9\%)$. This is fairly close to the numerical value of Γ_t/m_t, which represents the expected order of magnitude. At the LHC, with $\sqrt{s} = 7\,\text{TeV}$, FtW effects turn out to be even smaller: $+0.4\%$ at LO and $+0.2\%$ (comparable to the Monte Carlo statistical error) at NLO. Most likely this difference to the result of $\sim 1\%$ at Tevatron is due to the influence of singly-top-resonant diagrams corresponding to associated tW production, whose positive contribution even overcompensates the negative effects from off-shell $t\bar{t}$ production.

The results of this extrapolation have been confirmed in a dedicated comparison [63] between our calculation and the one of Ref. [29] for on-shell top quarks. A similar $\Gamma_t \to 0$ extrapolation has been presented in Ref. [33].

3.7 Comparison with HELAC-NLO

Our predictions for the hadronic $\nu_e e^+ \mu^- \bar{\nu}_\mu b\bar{b}$ cross section have been successfully reproduced by the HELAC-NLO collaboration and vice versa. On the one hand, our results for the Tevatron in NwWA [32] have been checked by the HELAC-NLO group

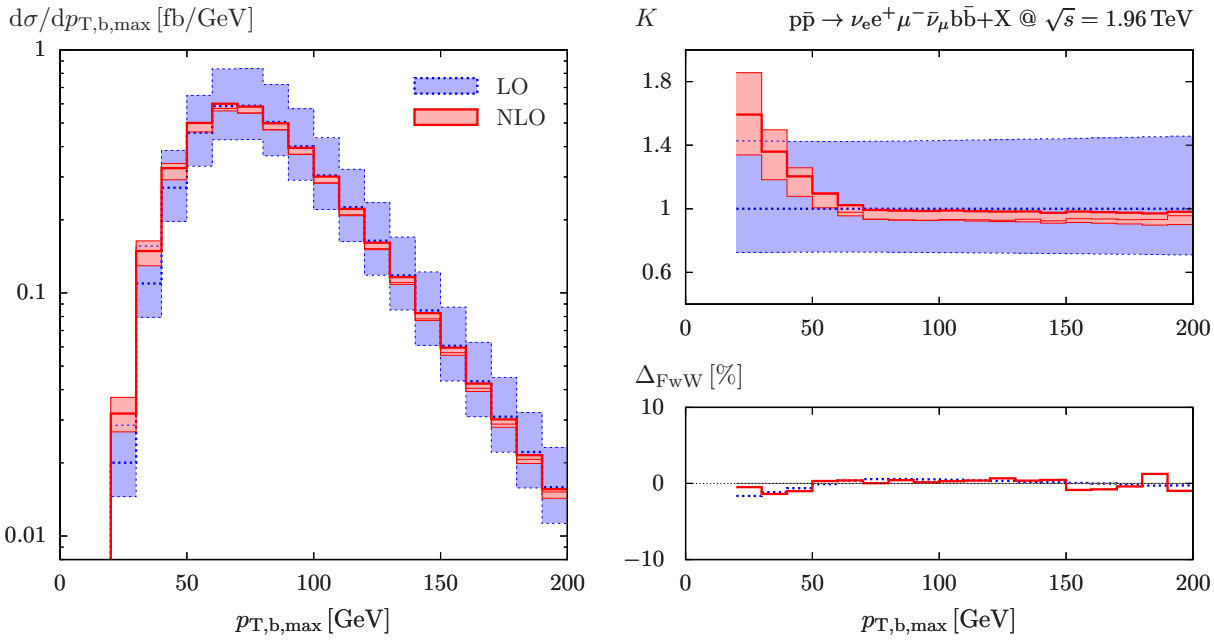

Figure 26: Transverse-momentum distribution of the harder b jet with standard cuts for Tevatron for dynamical scale $\mu_0 = E_{\mathrm{T}}$.

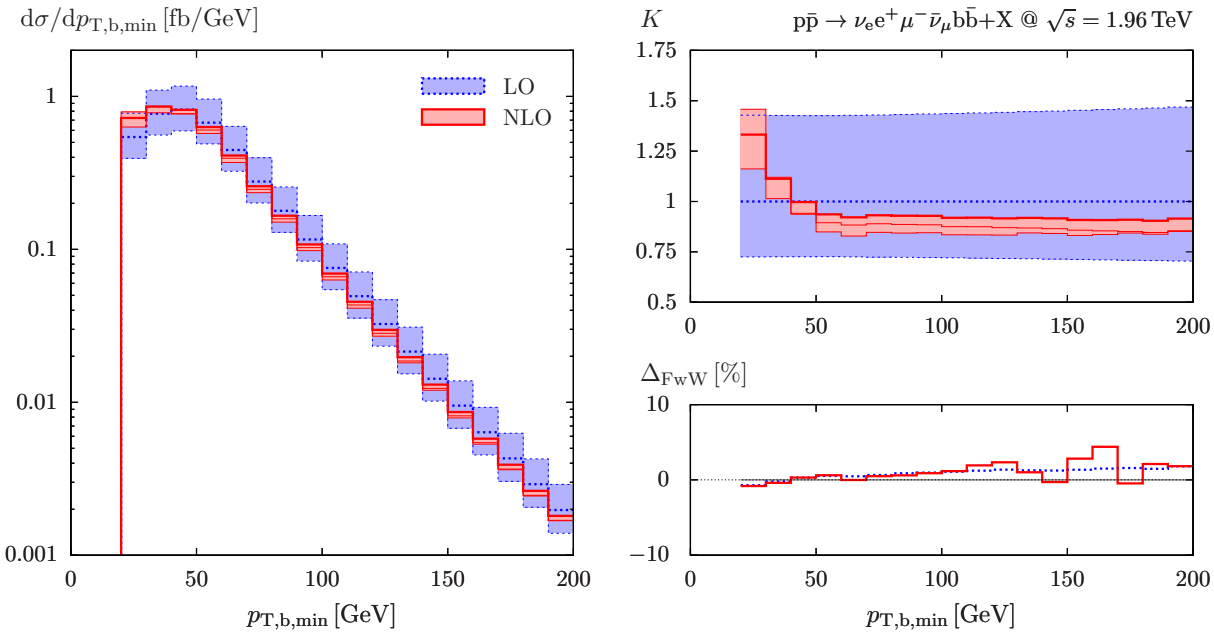

Figure 27: Transverse-momentum distribution of the softer b jet with standard cuts for Tevatron for dynamical scale $\mu_0 = E_{\mathrm{T}}$.

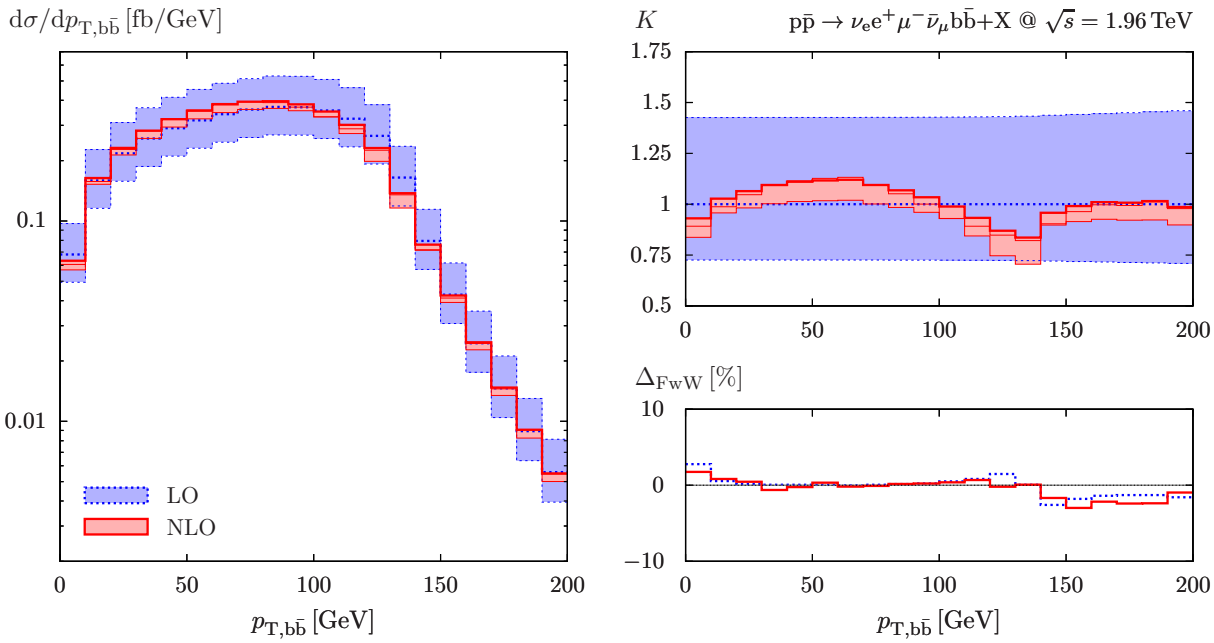

Figure 28: Transverse-momentum distribution of the $\mathrm{b\bar{b}}$ pair with standard cuts for Tevatron for dynamical scale $\mu_0 = E_\mathrm{T}$.

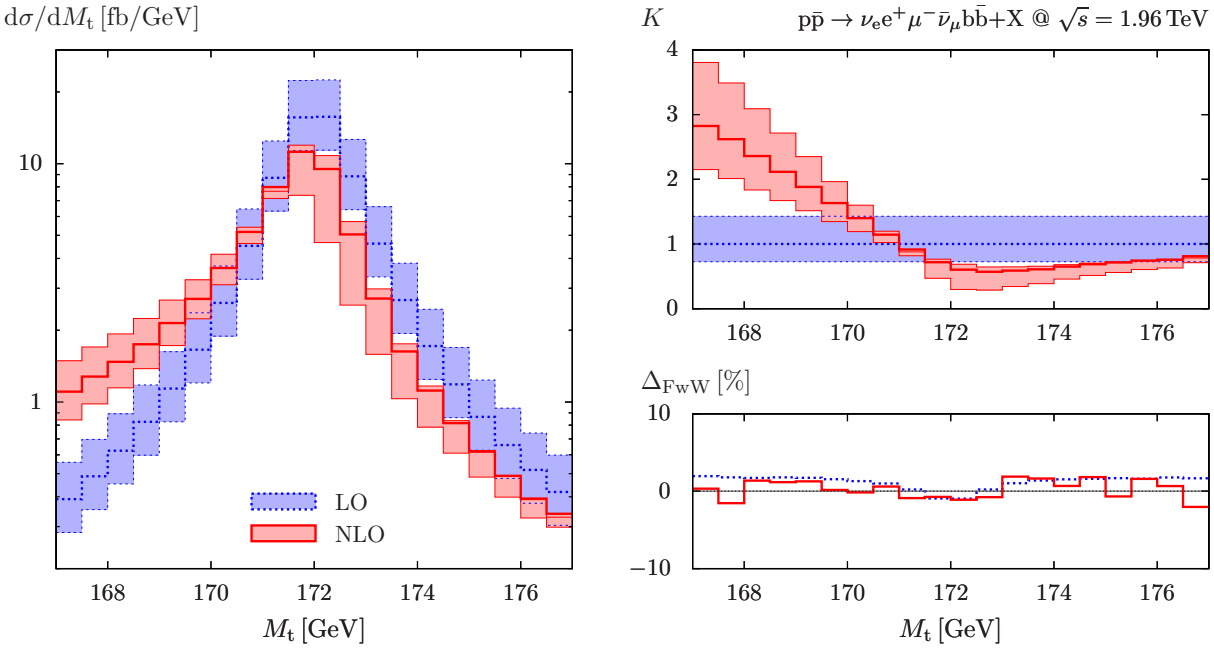

Figure 29: Invariant-mass distribution of the top quark, $M_\mathrm{t} = M_{\nu_\mathrm{e}\mathrm{e}^+\mathrm{b}}$, with standard cuts for Tevatron for dynamical scale $\mu_0 = E_\mathrm{T}$.

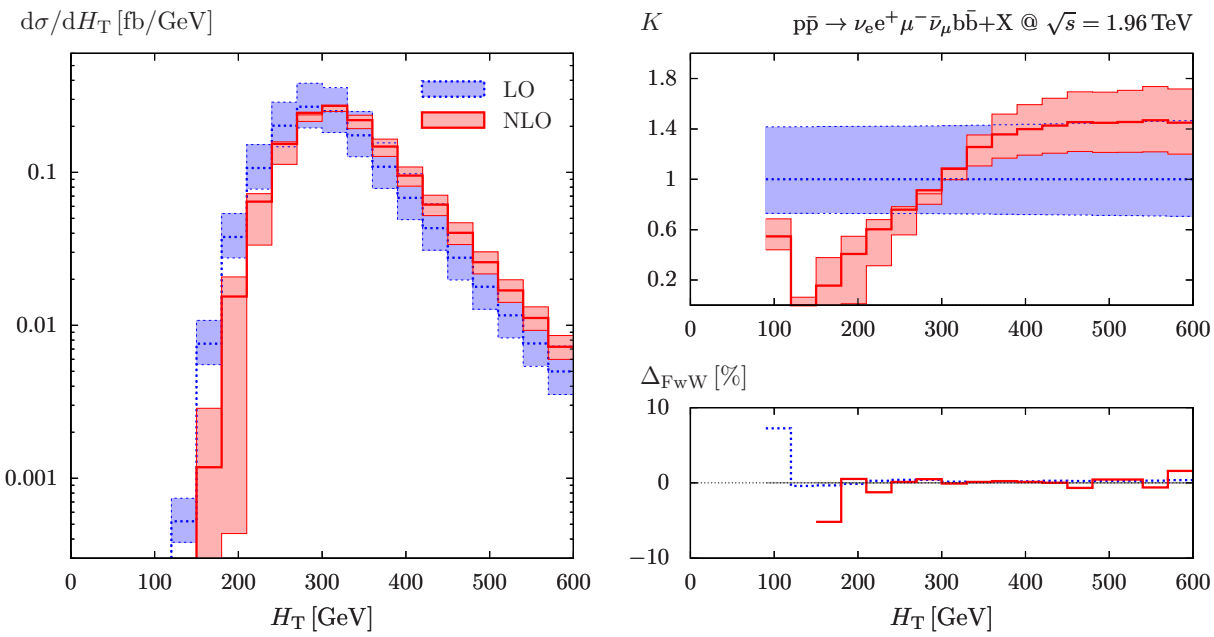

Figure 30: Distribution in the total transverse energy with standard cuts for Tevatron for dynamical scale $\mu_0 = E_{\mathrm{T}}$.

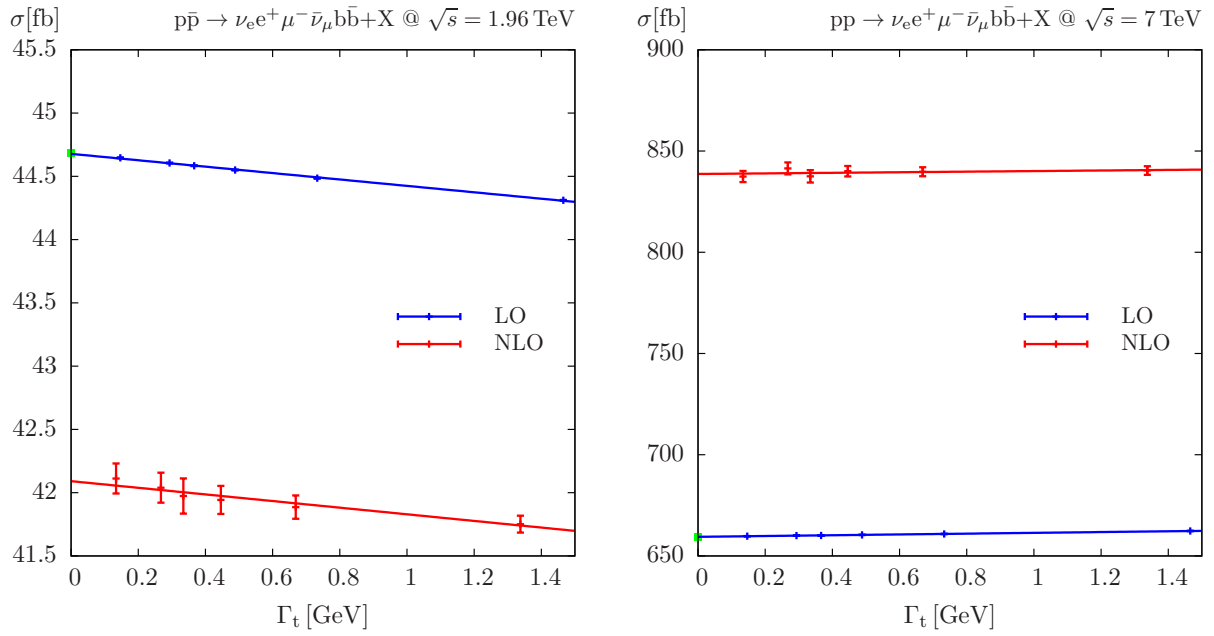

Figure 31: Numerical narrow-top-width extrapolation of the LO and NLO $\nu_{\mathrm{e}}\mathrm{e}^+\mu^-\bar{\nu}_\mu\mathrm{b}\bar{\mathrm{b}}$ cross section at Tevatron and the LHC at $\sqrt{s} = 7\,\mathrm{TeV}$. This study does not include finite-W-width effects and is based on the same fixed-scale choice, $\mu_0 = m_{\mathrm{t}}$, for Tevatron and LHC.

collider	energy	σ_{LO}[fb]	σ_{LO}[fb]	σ_{NLO}[fb]	σ_{NLO}[fb]
		Ref. [33]	this work	Ref. [33]	this work
Tevatron	1.96 TeV	34.922(14)	34.923(4)	35.705(47)	35.777(24)
LHC	7 TeV	550.54(18)	550.30(6)	808.46(98)	807.56(52)
LHC	10 TeV	1394.72(75)	1394.51(14)	1993.3(2.5)	1992.1(1.4)

Table 5: Cross sections for off-shell top-pair production for various colliders in the setup of Ref. [33] with anti-k_{T} algorithm.

finding agreement within integration errors [114]. On the other hand, we compared the FwW variant of our calculation against the HELAC-NLO predictions of Ref. [33]. The corresponding results obtained with the anti-k_{T} jet algorithm and the input parameters, cuts, and PDFs of Ref. [33] are listed in Table 5. At LO and NLO both calculations coincide within $(1-2)\sigma$, which is for NLO at the level of 0.2%. We note, however, that the numerical values of the input parameters $\Gamma_{\mathrm{t}}^{\mathrm{LO}}$ and $\Gamma_{\mathrm{t}}^{\mathrm{NLO}}$ used in Ref. [33], and adopted for the technical comparison in Table 5, do not include FwW corrections. As discussed in Sections 2.1.3 and 3.3, this induces a fake FwW shift of roughly -3% in the integrated cross section.

4 Conclusions

The precise understanding of top–antitop production is important for precision tests of the Standard Model and in searches for the Higgs boson and new physics. In this paper, we have presented NLO QCD predictions for the process $\mathrm{pp/p\bar{p}} \to \nu_{\mathrm{e}}\mathrm{e}^+\mu^-\bar{\nu}_\mu\mathrm{b\bar{b}} + X$, which corresponds to $\mathrm{t\bar{t}}$ production and decay in the di-lepton channel. The calculation includes all finite-top-width effects, i.e. off-shell top contributions, diagrams involving less than two top resonances, and all factorizable and non-factorizable NLO corrections. The leptonic W-boson decays have been described alternatively within a narrow-W-width approximation or including finite-W-width effects.

The employed techniques, based on Feynman diagrams and tensor integrals, provide high numerical stability and CPU efficiency. Each Feynman diagram is algebraically reduced to a canonical form and automatically processed to Fortran output, while tensor loop integrals are reduced to scalar integrals using numerical algorithms that avoid instabilities due to inverse Gram determinants and other spurious singularities. The real corrections are integrated using the dipole subtraction method.

We have presented a detailed study of integrated and differential cross sections and of asymmetries at Tevatron and the LHC at $\sqrt{s} = 7\,\mathrm{TeV}$, 8 TeV, and 14 TeV. We pointed out that a fixed QCD scale leads to perturbative instabilities in the tails of transverse-momentum distributions, while using a dynamical scale related to the transverse energy of the top quarks yields stable NLO predictions. For the LHC, where top–antitop production mainly proceeds via gluon–gluon annihilation, we decided to reduce the QCD scale by a factor two as compared to the Tevatron, where the quark–antiquark channel dominates.

This can be motivated by resummation of higher-order corrections, and leads to smaller K factors and a somewhat reduced residual scale dependence.

We also discussed the consequences of truncating the perturbative expansion at NLO in presence of unstable intermediate particles. Although the NLO corrections to the production and decay of top quarks are separately well known, a fixed-order NLO description of the entire process, i.e. production and decay, does not include the product of these two corrections. Such contributions are of NNLO kind but can largely exceed one per cent. To take them into account, we introduced an approach based on the idea of matching the inclusive $\nu_{\mathrm{e}}\mathrm{e}^+\mu^-\bar{\nu}_\mu\mathrm{b}\bar{\mathrm{b}}$ cross section, in the $\Gamma_{\mathrm{t}} \to 0$ limit, to the on-shell $\mathrm{t}\bar{\mathrm{t}}$ cross section. Numerically, the corresponding correction amounts to a few per cent.

Effects associated to the finite top-quark width are formally suppressed by $\Gamma_{\mathrm{t}}/m_{\mathrm{t}}$ and turn out to be below 1% for the total cross sections at Tevatron and the LHC at $\sqrt{s} = 7\,\mathrm{TeV}$. In contrast, finite-top-width effects can reach tens of per cent in phase space regions where top–antitop production is suppressed as a signal, but remains important as a background to Higgs and new-physics searches, as discussed in Ref. [63] where our results are compared to the ones of the (spin-correlated) narrow-width approximation of Ref. [29].

In spite of the larger numerical value of $\Gamma_{\mathrm{W}}/M_{\mathrm{W}}$ as compared to $\Gamma_{\mathrm{t}}/m_{\mathrm{t}}$, finite-W-width effects turn out to be less important than finite-top-width effects. For observables that are dominated by on-shell top quarks they remain below 0.5%, and for all other observables considered in the present paper they never exceed a few per cent. The only exception is the $M_{\mathrm{e}^+\mathrm{b}}$ distribution in the vicinity of $M^2_{\mathrm{e}^+\mathrm{b}} = m^2_{\mathrm{t}} - M^2_{\mathrm{W}}$, an observable which is, however, important for the precision measurement of the top-quark mass. The small size of finite-W-width contributions (to inclusive observables) is due to a double-suppression mechanism, which involves subtle cancellations between finite-W-width corrections to $\nu_{\mathrm{e}}\mathrm{e}^+\mu^-\bar{\nu}_\mu\mathrm{b}\bar{\mathrm{b}}$ matrix elements and to the Γ_{t} input parameter. Besides these observations, one should keep in mind that observables where top-quark and/or W-boson resonances are kinematically excluded can receive much larger finite-width contributions.

The step from on-shell top quarks to the inclusion of the top-quark decays with its full off-shell effects and the differential information on the decay products, including NLO QCD corrections, is an important step towards pushing the simulation of $\mathrm{t}\bar{\mathrm{t}}$ production at hadron colliders to a higher level. A natural next development, apart from extending the calculation to hadronic W decays as well, consists in a proper matching of the new NLO QCD corrections to off-shell $\mathrm{t}\bar{\mathrm{t}}$ production with QCD parton showers. Further future improvements of the calculation should also aim at including NLO electroweak corrections, a task that actually leads to a horrible NLO calculation for a $2 \to 6$ particle process. However, our setup of using a double-pole approximation for the W resonances effectively factorizes the full process again into a $2 \to 4$ ($\mathrm{WWb}\bar{\mathrm{b}}$) production and the $1 \to 2$ W-boson decays, rendering this calculation possible, though still very demanding.

Acknowledgements

S.P. would like to acknowledge financial support from the SNSF.

particle	$p^0\,[\mathrm{GeV}]$	$p^1\,[\mathrm{GeV}]$	$p^2\,[\mathrm{GeV}]$	$p^3\,[\mathrm{GeV}]$
a	250	0	0	250
b	250	0	0	−250
ν_e	48.56688853967434	−5.434957739109776	−19.57544900121795	44.11355452919156
e^+	44.98131949428399	27.80765763034380	−19.96763010585797	−29.17785167753225
μ^-	81.94400052131301	35.50973810316283	57.00882135433334	−46.94541520821219
$\bar{\nu}_\mu$	75.44248660279438	−13.21633653678938	−1.177064626981959	−74.26649144952955
b	156.4430715983779	−88.78355499018868	−95.32442077834540	86.63238319307789
$\bar{\mathrm{b}}$	92.62223324355639	44.11745353258120	79.03574315806995	19.64382061300453

Table 6: Phase-space point for the partonic process $ab \to \nu_\mathrm{e}\mathrm{e}^+\mu^-\bar{\nu}_\mu\mathrm{b}\bar{\mathrm{b}}$. All scattering particles are massless, intermediate top quarks are (slightly) off shell, and intermediate W bosons are exactly on shell, i.e. $(p_{\nu_\mathrm{e}} + p_{\mathrm{e}^+})^2 = (p_{\mu^-} + p_{\bar{\nu}_\mu})^2 = M_\mathrm{W}^2$.

A Benchmark numbers for the virtual corrections

In order to facilitate a comparison to our calculation, we provide explicit numbers for the squared tree amplitude and the corresponding virtual correction for the partonic processes $\mathrm{u}\bar{\mathrm{u}}/\mathrm{gg} \to \nu_\mathrm{e}\mathrm{e}^+\mu^-\bar{\nu}_\mu\mathrm{b}\bar{\mathrm{b}}$ evaluated at the phase-space point specified in Table 6. The amplitudes are computed using the input parameters of Section 3.1 and the complex top-quark mass (2.3). For the top-quark width we use the NLO value in (3.9), which includes FwW corrections, both in the tree and one-loop matrix elements. Since we compute virtual matrix elements handling W-boson resonances in double-pole approximation, we consider a phase-space point with on-shell intermediate W bosons. Moreover, as discussed in Section 2.1.3, we treat the W- and Z-boson masses as real parameters, we set $\Gamma_\mathrm{Z} = 0$, and we insert a non-zero W-boson width only in the W-boson propagator, which contributes a factor $1/(\Gamma_\mathrm{W} M_\mathrm{W})$ for each W resonance at $p_\mathrm{W}^2 = M_\mathrm{W}^2$. For the renormalization scale and the scale of dimensional regularization we choose $\mu = \mu_\mathrm{R} = m_\mathrm{t}$. The corresponding values of the strong coupling constant in the renormalization scheme described in Section 3 are

$$\alpha_\mathrm{s}(m_\mathrm{t})|_\mathrm{LO} = 0.1258086856923967, \qquad \alpha_\mathrm{s}(m_\mathrm{t})|_\mathrm{NLO} = 0.1095186120831399. \tag{A.1}$$

In the following we use the NLO strong coupling everywhere, i.e. also in tree matrix elements.

For the spin- and colour-averaged squared LO amplitudes in DPA we obtain

$$\begin{aligned} |\mathcal{M}^\mathrm{LO}_\mathrm{u\bar{u},DPA}|^2 &= 1.568863069202805 \cdot 10^{-5}\,\mathrm{GeV}^{-8}, \\ |\mathcal{M}^\mathrm{LO}_\mathrm{gg,DPA}|^2 &= 4.554053154627972 \cdot 10^{-5}\,\mathrm{GeV}^{-8}, \end{aligned} \tag{A.2}$$

while including doubly- and singly-W-resonant diagrams in the complex-mass scheme (2.28) with input parameters (3.10) yields

$$|\mathcal{M}^\mathrm{LO}_\mathrm{u\bar{u},full}|^2 = 1.567938932324559 \cdot 10^{-5}\,\mathrm{GeV}^{-8},$$

$$|\mathcal{M}^{\text{LO}}_{\text{gg,full}}|^2 = 4.551376909529072 \cdot 10^{-5}\,\text{GeV}^{-8}. \tag{A.3}$$

We express virtual NLO contributions in the $2 \to 6$ phase space as Laurent series in $\epsilon = (4-D)/2$,

$$|\mathcal{M}_{\text{DPA}}|^2 = \left(1 + c_\Gamma \sum_{k=0}^{2} \delta^{(k)}_{\text{NLO}} \epsilon^{-k}\right) |\mathcal{M}^{\text{LO}}_{\text{DPA}}|^2, \tag{A.4}$$

where we factor out the LO term in DPA and the normalization factor

$$\begin{aligned} c_\Gamma &= \frac{(4\pi)^\epsilon \Gamma(1+\epsilon)\Gamma^2(1-\epsilon)}{\Gamma(1-2\epsilon)} = \frac{(4\pi)^\epsilon}{\Gamma(1-\epsilon)} + \mathcal{O}(\epsilon^3) \\ &= (4\pi)^\epsilon \Gamma(1+\epsilon) - \frac{\pi^2}{6}\epsilon^2 + \mathcal{O}(\epsilon^3). \end{aligned} \tag{A.5}$$

We split the result into the two parts,

$$\delta^{(k)}_{\text{NLO}} = \delta^{(k)}_{\text{loops}} + \delta^{(k)}_{\text{I}}, \tag{A.6}$$

which correspond to the contributions of renormalized loop diagrams (loops) and the I operator of the dipole subtraction function as defined in Ref. [59]. Here we work with purely massless light fermions, i.e. in pure dimensional regularization. In $\delta^{(k)}_{\text{loops}}$ we include counterterm contributions from field, coupling, and mass renormalization. The numbers in Table 7 have been obtained in the 't Hooft–Feynman gauge using the 't Hooft–Veltman variant of dimensional regularization (four-dimensional external partons).

The agreement between our two independent versions of the virtual corrections, as can be seen from Table 7, is typically about 11 digits at non-exceptional phase-space points.

References

[1] P. Nason et al., *The One Particle Inclusive Differential Cross-Section for Heavy Quark Production in Hadronic Collisions*, *Nucl. Phys.* **B327** (1989) 49–92.

[2] W. Beenakker, W. van Neerven, R. Meng, G. Schuler, and J. Smith, *QCD corrections to heavy quark production in hadron hadron collisions*, *Nucl. Phys.* **B351** (1991) 507–560.

[3] M. L. Mangano, P. Nason, and G. Ridolfi, *Heavy quark correlations in hadron collisions at next-to-leading order*, *Nucl. Phys.* **B373** (1992) 295–345.

[4] S. Frixione, M. L. Mangano, P. Nason, and G. Ridolfi, *Top quark distributions in hadronic collisions*, *Phys. Lett.* **B351** (1995) 555–561, [hep-ph/9503213].

[5] W. Beenakker, A. Denner, W. Hollik, R. Mertig, T. Sack, et al., *Electroweak one loop contributions to top pair production in hadron colliders*, *Nucl. Phys.* **B411** (1994) 343–380.

[6] S. Moretti, M. R. Nolten, and D. A. Ross, *Weak corrections to gluon-induced top-antitop hadro-production*, *Phys. Lett.* **B639** (2006) 513–519, [hep-ph/0603083].

$u\bar{u}$ channel		$\delta^{(2)}$	$\delta^{(1)}$	$\delta^{(0)}$
loops	v1	−0.0929622851927013	−0.103079416107610	0.346530980271734
	v2	−0.0929622851925008	−0.103079416107340	0.346530980272341
I	v1	0.0929622851925095	0.103079416107488	−0.041671620626660
	v2	0.0929622851925092	0.103079416107487	−0.041671620626660
NLO	v1	−0.0000000000001918	−0.000000000000122	0.304859359645074
	v2	0.0000000000000084	0.000000000000146	0.304859359645681
gg channel		$\delta^{(2)}$	$\delta^{(1)}$	$\delta^{(0)}$
loops	v1	−0.1510637134378864	−0.032125892699063	0.571739679133372
	v2	−0.1510637134378313	−0.032125892699187	0.571739679132260
I	v1	0.1510637134378276	0.032125892699080	−0.155205928257365
	v2	0.1510637134378276	0.032125892699079	−0.155205928257365
NLO	v1	−0.0000000000000588	0.000000000000017	0.416533750876007
	v2	−0.0000000000000037	−0.000000000000107	0.416533750874894

Table 7: Various contributions to the virtual NLO corrections to $u\bar{u}/gg \to \nu_e e^+ \mu^- \bar{\nu}_\mu b\bar{b}$ at the phase-space point specified in Table 7. For each contribution we provide the results of the two independent calculations (v1 and v2).

[7] J. H. Kühn, A. Scharf, and P. Uwer, *Electroweak effects in top-quark pair production at hadron colliders*, *Eur. Phys. J.* **C51** (2007) 37–53, [hep-ph/0610335].

[8] W. Bernreuther, M. Fücker, and Z.-G. Si, *Electroweak corrections to $t\bar{t}$ production at hadron colliders*, *Nuovo Cim.* **B123** (2008) 1036–1044, [arXiv:0808.1142].

[9] W. Hollik and M. Kollar, *NLO QED contributions to top-pair production at hadron collider*, *Phys. Rev.* **D77** (2008) 014008.

[10] J. H. Kühn and G. Rodrigo, *Charge asymmetries of top quarks at hadron colliders revisited*, *JHEP* **1201** (2012) 063, [arXiv:1109.6830].

[11] M. Beneke, P. Falgari, and C. Schwinn, *Soft radiation in heavy-particle pair production: All-order colour structure and two-loop anomalous dimension*, *Nucl. Phys.* **B828** (2010) 69–101, [arXiv:0907.1443].

[12] M. Czakon, A. Mitov, and G. F. Sterman, *Threshold Resummation for Top-Pair Hadroproduction to Next-to-Next-to-Leading Log*, *Phys. Rev.* **D80** (2009) 074017, [arXiv:0907.1790].

[13] V. Ahrens, A. Ferroglia, M. Neubert, B. D. Pecjak, and L. L. Yang, *Renormalization-Group Improved Predictions for Top-Quark Pair Production at Hadron Colliders*, *JHEP* **1009** (2010) 097, [arXiv:1003.5827].

[14] N. Kidonakis, *Next-to-next-to-leading soft-gluon corrections for the top quark cross section and transverse momentum distribution*, *Phys. Rev.* **D82** (2010) 114030, [arXiv:1009.4935].

[15] S. Dittmaier, P. Uwer, and S. Weinzierl, *NLO QCD corrections to t anti-t + jet production at hadron colliders*, *Phys. Rev. Lett.* **98** (2007) 262002, [hep-ph/0703120].

[16] B. Kniehl, Z. Merebashvili, J. Körner, and M. Rogal, *Heavy quark pair production in gluon fusion at next-to- next-to-leading $O(\alpha_s^4)$ order: One-loop*, *Phys. Rev.* **D78** (2008) 094013, [arXiv:0809.3980].

[17] C. Anastasiou and S. M. Aybat, *The one-loop gluon amplitude for heavy-quark production at NNLO*, *Phys. Rev.* **D78** (2008) 114006, [arXiv:0809.1355].

[18] M. Czakon, A. Mitov, and S. Moch, *Heavy-quark production in massless quark scattering at two loops in QCD*, *Phys. Lett.* **B651** (2007) 147–159, [arXiv:0705.1975].

[19] M. Czakon, A. Mitov, and S. Moch, *Heavy-quark production in gluon fusion at two loops in QCD*, *Nucl. Phys.* **B798** (2008) 210, [arXiv:0707.4139].

[20] M. Czakon, *Tops from Light Quarks: Full Mass Dependence at Two-Loops in QCD*, *Phys. Lett.* **B664** (2008) 307–314, [arXiv:0803.1400].

[21] R. Bonciani, A. Ferroglia, T. Gehrmann, D. Maitre, and C. Studerus, *Two-Loop Fermionic Corrections to Heavy-Quark Pair Production: The Quark-Antiquark Channel*, *JHEP* **07** (2008) 129, [arXiv:0806.2301].

[22] R. Bonciani et al., *Two-Loop Planar Corrections to Heavy-Quark Pair Production in the Quark-Antiquark Channel*, *JHEP* **0908** (2009) 067, [arXiv:0906.3671].

[23] R. Bonciani, A. Ferroglia, T. Gehrmann, A. Manteuffel, and C. Studerus, *Two-Loop Leading Color Corrections to Heavy-Quark Pair Production in the Gluon Fusion Channel*, *JHEP* **1101** (2011) 102, [arXiv:1011.6661].

[24] A. Gehrmann-De Ridder and M. Ritzmann, *NLO Antenna Subtraction with Massive Fermions*, *JHEP* **0907** (2009) 041, [arXiv:0904.3297].

[25] M. Czakon, *A novel subtraction scheme for double-real radiation at NNLO*, *Phys. Lett.* **B693** (2010) 259–268, [arXiv:1005.0274].

[26] P. Baernreuther, M. Czakon, and A. Mitov, *Percent level precision physics at the Tevatron: first genuine NNLO QCD corrections to $q\bar{q} \to t\bar{t} + X$*, arXiv:1204.5201.

[27] N. Kauer and D. Zeppenfeld, *Finite width effects in top quark production at hadron colliders*, *Phys.Rev.* **D65** (2002) 014021, [hep-ph/0107181].

[28] W. Bernreuther, A. Brandenburg, Z. Si, and P. Uwer, *Top quark pair production and decay at hadron colliders*, *Nucl. Phys.* **B690** (2004) 81–137, [hep-ph/0403035].

[29] K. Melnikov and M. Schulze, *NLO QCD corrections to top quark pair production and decay at hadron colliders*, *JHEP* **08** (2009) 049, [arXiv:0907.3090].

[30] W. Bernreuther and Z.-G. Si, *Distributions and correlations for top quark pair production and decay at the Tevatron and LHC*, *Nucl. Phys.* **B837** (2010) 90, [arXiv:1003.3926].

[31] J. M. Campbell and R. K. Ellis, *Top-quark processes at NLO in production and decay*, arXiv:1204.1513.

[32] A. Denner, S. Dittmaier, S. Kallweit, and S. Pozzorini, *NLO QCD corrections to WWbb production at hadron colliders*, *Phys. Rev. Lett.* **106** (2011) 052001, [arXiv:1012.3975].

[33] G. Bevilacqua et al., *Complete off-shell effects in top quark pair hadroproduction with leptonic decay at next-to-leading order*, *JHEP* **1102** (2011) 083, [arXiv:1012.4230].

[34] **SM and NLO Multileg Working Group** Collaboration, J. R. Andersen et al., *The SM and NLO multileg working group: Summary report*, arXiv:1003.1241.

[35] A. Bredenstein, A. Denner, S. Dittmaier, and S. Pozzorini, *NLO QCD corrections to pp → t anti-t b anti-b + X at the LHC*, *Phys.Rev.Lett.* **103** (2009) 012002, [arXiv:0905.0110].

[36] G. Bevilacqua, M. Czakon, C. Papadopoulos, R. Pittau, and M. Worek, *Assault on the NLO Wishlist: pp → t anti-t b anti-b*, *JHEP* **0909** (2009) 109, [arXiv:0907.4723].

[37] G. Bevilacqua, M. Czakon, C. Papadopoulos, and M. Worek, *Hadronic top-quark pair production in association with two jets at Next-to-Leading Order QCD*, *Phys.Rev.* **D84** (2011) 114017, [arXiv:1108.2851].

[38] R. Ellis, K. Melnikov, and G. Zanderighi, *Generalized unitarity at work: first NLO QCD results for hadronic W + 3jet production*, *JHEP* **0904** (2009) 077, [arXiv:0901.4101].

[39] T. Melia, K. Melnikov, R. Rontsch, and G. Zanderighi, *NLO QCD corrections for W^+W^- pair production in association with two jets at hadron colliders*, *Phys.Rev.* **D83** (2011) 114043, [arXiv:1104.2327].

[40] C. Berger, Z. Bern, L. J. Dixon, F. Febres Cordero, D. Forde, et al., *Precise Predictions for W + 3 Jet Production at Hadron Colliders*, *Phys.Rev.Lett.* **102** (2009) 222001, [arXiv:0902.2760].

[41] C. Berger, Z. Bern, L. J. Dixon, F. Febres Cordero, D. Forde, et al., *Next-to-Leading Order QCD Predictions for Z, γ^*+3-Jet Distributions at the Tevatron*, *Phys.Rev.* **D82** (2010) 074002, [arXiv:1004.1659].

[42] C. Berger, Z. Bern, L. J. Dixon, F. Febres Cordero, D. Forde, et al., *Precise Predictions for W + 4 Jet Production at the Large Hadron Collider*, *Phys.Rev.Lett.* **106** (2011) 092001, [arXiv:1009.2338].

[43] H. Ita, Z. Bern, L. Dixon, F. Febres Cordero, D. Kosower, et al., *Precise Predictions for Z + 4 Jets at Hadron Colliders*, *Phys.Rev.* **D85** (2012) 031501, [arXiv:1108.2229].

[44] Z. Bern, G. Diana, L. Dixon, F. Febres Cordero, S. Hoeche, et al., *Four-Jet Production at the Large Hadron Collider at Next-to-Leading Order in QCD*, arXiv:1112.3940.

[45] F. Campanario, C. Englert, M. Rauch, and D. Zeppenfeld, *Precise predictions for $W\gamma\gamma$+jet production at hadron colliders*, *Phys.Lett.* **B704** (2011) 515–519, [arXiv:1106.4009].

[46] N. Greiner, A. Guffanti, T. Reiter, and J. Reuter, *NLO QCD corrections to the production of two bottom-antibottom pairs at the LHC*, *Phys.Rev.Lett.* **107** (2011) 102002, [arXiv:1105.3624].

[47] N. Greiner, G. Heinrich, P. Mastrolia, G. Ossola, T. Reiter, et al., *NLO QCD corrections to the production of W+ W- plus two jets at the LHC*, *Phys.Lett.* **B713** (2012) 277–283, [arXiv:1202.6004].

[48] S. Becker, D. Goetz, C. Reuschle, C. Schwan, and S. Weinzierl, *NLO results for five, six and seven jets in electron–positron annihilation*, *Phys.Rev.Lett.* **108** (2012) 032005, [arXiv:1111.1733].

[49] G. Bevilacqua and M. Worek, *Constraining BSM Physics at the LHC: Four top final states with NLO accuracy in perturbative QCD*, arXiv:1206.3064.

[50] A. Denner, S. Dittmaier, M. Roth, and L. H. Wieders, *Complete electroweak $\mathcal{O}(\alpha)$ corrections to charged-current $e^+e^- \to$ 4 fermion processes*, *Phys. Lett.* **B612** (2005) 223, [hep-ph/0502063]. Erratum-ibid. **B704** (2011) 667-668.

[51] A. Denner, S. Dittmaier, M. Roth, and L. Wieders, *Electroweak corrections to charged-current $e^+e^- \to$ 4 fermion processes: Technical details and further results*, *Nucl.Phys.* **B724** (2005) 247–294, [hep-ph/0505042]. Erratum-ibid. **B854** (2012) 504–507.

[52] A. Denner and S. Dittmaier, *Reduction of one-loop tensor 5-point integrals*, *Nucl. Phys.* **B658** (2003) 175–202.

[53] A. Denner and S. Dittmaier, *Reduction schemes for one-loop tensor integrals*, *Nucl. Phys.* **B734** (2006) 62–115.

[54] G. 't Hooft and M. J. G. Veltman, *Scalar One Loop Integrals*, *Nucl. Phys.* **B153** (1979) 365–401.

[55] A. Denner and S. Dittmaier, *Scalar one-loop 4-point integrals*, *Nucl. Phys.* **B844** (2011) 199–242, [arXiv:1005.2076].

[56] S. Catani and M. H. Seymour, *A general algorithm for calculating jet cross sections in NLO QCD*, *Nucl. Phys.* **B485** (1997) 291–419.

[57] S. Dittmaier, *A General approach to photon radiation off fermions*, *Nucl.Phys.* **B565** (2000) 69–122, [hep-ph/9904440].

[58] L. Phaf and S. Weinzierl, *Dipole formalism with heavy fermions*, *JHEP* **0104** (2001) 006, [hep-ph/0102207].

[59] S. Catani, S. Dittmaier, M. H. Seymour, and Z. Trocsanyi, *The Dipole formalism for next-to-leading order QCD calculations with massive partons*, *Nucl.Phys.* **B627** (2002) 189–265, [hep-ph/0201036].

[60] F. A. Berends, R. Pittau, and R. Kleiss, *All electroweak four fermion processes in electron–positron collisions*, *Nucl. Phys.* **B424** (1994) 308–342.

[61] A. Denner, S. Dittmaier, M. Roth, and D. Wackeroth, *Predictions for all processes $e^+e^- \to 4$ fermions + γ*, *Nucl. Phys.* **B560** (1999) 33–65, [hep-ph/9904472].

[62] S. Dittmaier and M. Roth, *LUSIFER: A LUcid approach to SIx FERmion production*, *Nucl. Phys.* **B642** (2002) 307–343, [hep-ph/0206070].

[63] A. Denner, S. Dittmaier, S. Kallweit, S. Pozzorini, and M. Schulze, *Finite-width effects in top-quark pair production and decay at the LHC*, in *The SM and NLO Multileg and SM MC Working Groups: Summary Report* (J. A. Maestre, S. Alioli, J. Andersen, R. Ball, A. Buckley, et al., eds.), pp. 55–63, 2012. arXiv:1203.6803.

[64] A. Denner, S. Dittmaier, S. Kallweit, S. Pozzorini and M. Schulze, *Off-shell effects in top–antitop production at hadron colliders*, in preparation.

[65] G. Bevilacqua, M. Czakon, M. Garzelli, A. van Hameren, A. Kardos, et al., *HELAC-NLO*, arXiv:1110.1499.

[66] V. S. Fadin, V. A. Khoze, and A. D. Martin, *Interference radiative phenomena in the production of heavy unstable particles*, *Phys.Rev.* **D49** (1994) 2247–2256.

[67] V. S. Fadin, V. A. Khoze, and A. D. Martin, *How suppressed are the radiative interference effects in heavy instable particle production?*, *Phys.Lett.* **B320** (1994) 141–144, [hep-ph/9309234].

[68] K. Melnikov and O. I. Yakovlev, *Top near threshold: All α_S corrections are trivial*, *Phys.Lett.* **B324** (1994) 217–223, [hep-ph/9302311].

[69] J. Küblbeck, M. Böhm, and A. Denner, *FEYNARTS: computer algebraic generation of Feynman graphs and amplitudes*, *Comput. Phys. Commun.* **60** (1990) 165–180.

[70] T. Hahn, *Generating Feynman diagrams and amplitudes with FeynArts 3*, *Comput. Phys. Commun.* **140** (2001) 418–431.

[71] A. Bredenstein, A. Denner, S. Dittmaier, and S. Pozzorini, *NLO QCD corrections to top anti-top bottom anti-bottom production at the LHC: 1. quark-antiquark annihilation*, *JHEP* **08** (2008) 108.

[72] A. Bredenstein, A. Denner, S. Dittmaier, and S. Pozzorini, *NLO QCD corrections to top anti-top bottom anti-bottom production at the LHC: 2. full hadronic results*, *JHEP* **1003** (2010) 021.

[73] T. Hahn and M. Perez-Victoria, *Automatized one-loop calculations in four and D dimensions*, *Comput. Phys. Commun.* **118** (1999) 153–165.

[74] S. Dittmaier, *Weyl-van-der-Waerden formalism for helicity amplitudes of massive particles*, *Phys. Rev.* **D59** (1999) 016007.

[75] T. Binoth, J. Guillet, G. Heinrich, E. Pilon, and C. Schubert, *An Algebraic/numerical formalism for one-loop multi-leg amplitudes*, *JHEP* **0510** (2005) 015, [hep-ph/0504267].

[76] J. Fleischer and T. Riemann, *A Complete algebraic reduction of one-loop tensor Feynman integrals*, *Phys.Rev.* **D83** (2011) 073004, [arXiv:1009.4436].

[77] D. Melrose, *Reduction of Feynman diagrams*, *Nuovo Cim.* **40** (1965) 181–213.

[78] G. Passarino and M. J. G. Veltman, *One Loop Corrections for e^+e^- Annihilation Into $\mu^+\mu^-$ in the Weinberg Model*, *Nucl. Phys.* **B160** (1979) 151.

[79] A. Ferroglia, M. Passera, G. Passarino, and S. Uccirati, *All purpose numerical evaluation of one loop multileg Feynman diagrams*, *Nucl.Phys.* **B650** (2003) 162–228, [hep-ph/0209219].

[80] W. Giele, E. Glover, and G. Zanderighi, *Numerical evaluation of one-loop diagrams near exceptional momentum configurations*, *Nucl.Phys.Proc.Suppl.* **135** (2004) 275–279, [hep-ph/0407016].

[81] W. Beenakker and A. Denner, *Infrared divergent scalar box integrals with applications in the electroweak standard model*, *Nucl. Phys.* **B338** (1990) 349–370.

[82] S. Dittmaier, *Separation of soft and collinear singularities from one-loop N-point integrals*, *Nucl. Phys.* **B675** (2003) 447–466, [hep-ph/0308246].

[83] R. G. Stuart, *Gauge invariance, analyticity and physical observables at the Z_0 resonance*, *Phys.Lett.* **B262** (1991) 113–119.

[84] A. Aeppli, G. J. van Oldenborgh, and D. Wyler, *Unstable particles in one loop calculations*, *Nucl.Phys.* **B428** (1994) 126–146, [hep-ph/9312212].

[85] M. W. Grünewald, G. Passarino, E. Accomando, A. Ballestrero, P. Bambade, et al., *Reports of the Working Groups on Precision Calculations for LEP2 Physics: Proceedings. Four fermion production in electron–positron collisions*, hep-ph/0005309.

[86] A. Denner, S. Dittmaier, M. Roth, and D. Wackeroth, *Electroweak radiative corrections to $e^+e^- \to WW \to 4$ fermions in double pole approximation: The RACOONWW approach*, *Nucl.Phys.* **B587** (2000) 67–117, [hep-ph/0006307].

[87] W. Beenakker, F. A. Berends, and A. Chapovsky, *Radiative corrections to pair production of unstable particles: results for $e^+e^- \to$ four fermions*, *Nucl.Phys.* **B548** (1999) 3–59, [hep-ph/9811481].

[88] J. Alwall et al., *MadGraph/MadEvent v4: The New Web Generation*, *JHEP* **09** (2007) 028.

[89] F. Cascioli, P. Maierhöfer, and S. Pozzorini, *Scattering Amplitudes with Open Loops*, *Phys.Rev.Lett.* **108** (2012) 111601, [arXiv:1111.5206].

[90] S. Dittmaier, S. Kallweit, and P. Uwer, *NLO QCD corrections to $pp/p\bar{p} \to$ WW+jet+X including leptonic W-boson decays*, *Nucl. Phys.* **B826** (2010) 18–70, [arXiv:0908.4124].

[91] F. Campanario, C. Englert, S. Kallweit, M. Spannowsky, and D. Zeppenfeld, *NLO QCD corrections to WZ+jet production with leptonic decays*, *JHEP* **07** (2010) 076, [arXiv:1006.0390].

[92] K. Hasegawa, S. Moch, and P. Uwer, *AutoDipole: Automated generation of dipole subtraction terms*, *Comput. Phys. Commun.* **181** (2010) 1802–1817, [arXiv:0911.4371].

[93] R. Kleiss and R. Pittau, *Weight optimization in multichannel Monte Carlo*, *Comput. Phys. Commun.* **83** (1994) 141–146.

[94] A. Bredenstein, S. Dittmaier, and M. Roth, *Four-fermion production at gamma gamma colliders. 2. Radiative corrections in double-pole approximation*, *Eur.Phys.J.* **C44** (2005) 27–49, [hep-ph/0506005].

[95] M. Ciccolini, A. Denner, and S. Dittmaier, *Strong and electroweak corrections to the production of Higgs + 2jets via weak interactions at the LHC*, *Phys. Rev. Lett.* **99** (2007) 161803, [arXiv:0707.0381].

[96] A. Martin, W. Stirling, R. Thorne, and G. Watt, *Parton distributions for the LHC*, *Eur. Phys. J.* **C63** (2009) 189–285, [arXiv:0901.0002].

[97] M. Jezabek and J. H. Kühn, *QCD Corrections to Semileptonic Decays of Heavy Quarks*, *Nucl. Phys.* **B314** (1989) 1.

[98] M. Cacciari, G. P. Salam, and G. Soyez, *The anti-kt jet clustering algorithm*, *JHEP* **04** (2008) 063, [arXiv:0802.1189].

[99] R. Bonciani, S. Catani, M. L. Mangano, and P. Nason, *NLL resummation of the heavy quark hadroproduction cross-section*, *Nucl.Phys.* **B529** (1998) 424–450, [hep-ph/9801375].

[100] **CDF** Collaboration, T. Aaltonen et al., *Evidence for a Mass Dependent Forward-Backward Asymmetry in Top Quark Pair Production*, *Phys.Rev.* **D83** (2011) 112003, [arXiv:1101.0034].

[101] **D0** Collaboration, V. M. Abazov et al., *Forward-backward asymmetry in top quark-antiquark production*, *Phys.Rev.* **D84** (2011) 112005, [arXiv:1107.4995].

[102] **CDF** Collaboration, T. Aaltonen et al., *Study of the Top Quark Production Asymmetry and Its Mass and Rapidity Dependence in the Full Run II Tevatron Dataset*, CDF-NOTE-10807.

[103] W. Hollik and D. Pagani, *The electroweak contribution to the top quark forward-backward asymmetry at the Tevatron*, *Phys.Rev.* **D84** (2011) 093003, [arXiv:1107.2606].

[104] W. Bernreuther and Z.-G. Si, *Top quark and leptonic charge asymmetries for the Tevatron and LHC*, arXiv:1205.6580.

[105] F. Halzen, P. Hoyer, and C. Kim, *Forward–backward asymmetry of hadroproduced heavy quarks in QCD*, *Phys.Lett.* **B195** (1987) 74.

[106] J. H. Kühn and G. Rodrigo, *Charge asymmetry of heavy quarks at hadron colliders*, *Phys.Rev.* **D59** (1999) 054017, [hep-ph/9807420].

[107] O. Antunano, J. H. Kühn, and G. Rodrigo, *Top quarks, axigluons and charge asymmetries at hadron colliders*, *Phys.Rev.* **D77** (2008) 014003, [arXiv:0709.1652].

[108] **ATLAS** Collaboration, *Measurement of the charge asymmetry in top quark pair production in pp collisions at sqrts=7 TeV using the ATLAS detector*, ATLAS CONF-2011-106.

[109] **CMS** Collaboration, *Measurement of the charge asymmetry in top quark pair production with the CMS experiment*, CMS-PAS-TOP-10-010.

[110] J. M. Butterworth, A. R. Davison, M. Rubin, and G. P. Salam, *Jet substructure as a new Higgs search channel at the LHC*, *Phys. Rev. Lett.* **100** (2008) 242001, [arXiv:0802.2470].

[111] J. M. Butterworth, A. R. Davison, K. Jakobs, V. E. Oezcan, G. Piacquadio, and C. Weiser, *ATLAS sensitivity to the standard model Higgs in the HW and HZ channels at high transverse momenta*, ATL-PHYS-PUB-2009-088.

[112] A. Kharchilava, *Top mass determination in leptonic final states with J/Ψ*, *Phys. Lett.* **B476** (2000) 73–78.

[113] S. Biswas, K. Melnikov, and M. Schulze, *Next-to-leading order QCD effects and the top quark mass measurements at the LHC*, *JHEP* **1008** (2010) 048, [arXiv:1006.0910].

[114] M. Worek, private communication.